IDENTIFYING FACTORS INFLUENCING ANTIRETROVIRAL PHARMACOLOGY AND HIV PERSISTENCE IN THE SPLEEN

Aaron S. Devanathan

A dissertation submitted to the faculty of the University of North Carolina at Chapel Hill in partial fulfillment of the requirements for the degree of Doctor of Philosophy in Pharmaceutical Sciences in the Eshelman School of Pharmacy (Pharmacotherapy and Experimental Therapeutics).

Chapel Hill
2022

Approved by:

Angela D.M. Kashuba

Paul B. Watkins

Yanguang Cao

Amanda H. Corbett

Yuri Fedoriw

ABSTRACT

Aaron S. Devanathan: Identifying Factors Influencing Antiretroviral Pharmacology and HIV Persistence in the Spleen
(Under the direction of Angela D.M. Kashuba)

Little is known about ARV pharmacology—and the factors that may influence it—in the spleen, which is a lymphoid organ and contains approximately 0.3% of HIV RNA during suppressive antiretroviral therapy (ART). We sought to characterize how ARVs distribute within the spleen, and determine the degree to which they concentrate and localize with HIV expression.

For Aim 1, we measured concentrations of 6 ARVs and 2 phosphorylated metabolites in three species. Generally, mice had the lowest splenic concentration of the three species, and nonhuman primates (NHPs) were most similar to humans. Spleen protein binding was lower than in plasma. Using quantitative proteomics, we quantified protein expression of 9 drug transporters in NHP and human spleens. NHPs had quantifiable Bcrp, Mrp4, and Ent1 concentrations; humans had quantifiable ENT1 concentrations. No relevant predictive relationships between transporters and ARV penetration were identified, nor did sex and viral infection.

For Aim 2, through quantitative mass spectrometry imaging (MSI) of NHP spleens, we determined that over 58% of tissue area and 50% of viral RNA was not exposed to detectable ARV. When drug was detected, almost all drug concentrations exceeded 50% inhibitory concentrations. Correcting the images for heme (assumed to be blood contamination) decreased

the ARV concentrations by 40%. Fibrosis markers covered 62% of tissue but ARV penetration did not appear to be affected by amount of fibrosis.

For Aim 3, we developed NHP and human PBPK models to describe the concentrations of tenofovir and emtricitabine and their metabolites. The final NHP and human models fit the observed data well and revealed species differences for emtricitabine: tissue:plasma AUC penetration ratios were significantly lower in NHPs than in humans. Adjusting partition coefficients did not change the T_{max} values for either species for both ARVs, providing evidence that blood flow is the limiting parameter.

This multifactorial, translational approach vastly improves our understanding of ARV pharmacology within lymphoid tissues, and informs development of future therapies for HIV eradication strategies in tissue reservoirs (i.e. “kick and kill”). These data highlight ART is not proximate to infected cells, and tissue concentrations of novel therapies must be quantified.

To my family

ACKNOWLEDGEMENTS

The completion of this dissertation would not have been possible without the academic and personal support provided by so many people. First and foremost, I would like to sincerely thank my advisor Dr. Angela Kashuba for all of her guidance throughout this journey. She encouraged and pushed me to become a greater scientist, and I am deeply honored to have served as a graduate student under her advisement. Under her leadership, I have grown as a researcher, critical thinker, and person. Dr. Kashuba always made time to guide my research progress, discuss research ideas, and provide advice as I move forward into my career. Without a doubt, she was the best advisor I could have asked for. She made graduate school so much fun for me, and I will pay that forward with my own trainees as I embark on an exciting academic career.

Next, I would like to thank my dissertation committee for selflessly lending their guidance to my dissertation. My committee chair Dr. Paul Watkins always asked me astute questions during committee meetings, my time as a T32 fellow, and through casual conversations. Most of the time, I didn't know the answers, but he made me think about my work more critically. I have known Dr. Amanda Corbett since my time as a resident, and she always helped me stay grounded and understand my work in the broader context. She has helped me become a better teacher, which translated into my presentations. Dr. Carter Cao was an invaluable resource as I worked through my PBPK modeling aim, a concept that was borne from his excellent teaching during the modular coursework. Dr. Yuri Fedoriw is an incredibly enthusiastic researcher, and I am very fortunate to have his assistance when interpreting

immunohistochemical data. He has also provided me great life advice such as: “Just try to learn something new every day”, a mantra I lived by during graduate school.

I would now like to highlight the many members of the Kashuba lab who provided scientific mentorship and guidance during my time here. Dr. Eli Rosen was an invaluable resource for the MSI work in my dissertation. He is without doubt the most patient person I have ever met. He helped me learn and understand MATLAB, mass spectrometry imaging, and how these tools can solve problems. I am also grateful to Nicole White, Dr. Yury Desyaterik, Dr. Joseph Mwangi, and Dr. Mac Gilliland for their support and interpretation of my MSI work. Dr. Mackenzie Cottrell has been a great resource for understanding HIV pharmacology and to put our work in a clinical context, and I can’t wait to become her colleague. Dr. Julie Dumond was a wonderful resource for melding my clinical knowledge with computational methods through her direction of the modular PK courses, and she will be a great resource to have moving forward. To Kashuba lab members past (Daijha Anderson, John Dohnal, Kimberly Handy, Justin Jones, Kristen Moody, Ashlyn Norris, Jason Pirone, Heather Prince, Erin Scholz, Nithya Srinivas, Allie Symonds, Micah Willis) and present (Amanda Schauer, Amanda Poliseno, Hannah Bryan, Brian Van Horne, Lauren Tompkins, Craig Sykes, Talisa Kinsale), thank you for your friendship and guidance over the years, making graduate school more fun than it already was for me.

This dissertation would not be possible without the great collaborators within and outside of UNC. Gabriela de la Cruz at the Translational Pathology Lab was always helpful in troubleshooting new antibodies or coming up with an analysis plan for staining spleen tissues. Dr. John Fallon was crucial to the transporter proteomics work, and I’m thankful for the time he spent teaching and explaining the methods to me. Dr. Michael Nekorchuk and the other members of Dr. Jacob Estes’ lab at OSHU patiently responded to my countless emails surrounding the

analysis and interpretation of RNAscope images. Without the animal studies performed by the Garcia lab at UNC, the Akkina lab at CSU, and the Luciw lab at UC Davis, and the tissue collection performed by the NDRI and NNTC, my dissertation would not have been possible.

When I first moved to North Carolina, I began as a pharmacy resident at UNC Health, and I got to know so many wonderfully amazing clinicians. I would like to especially thank Drs. Emily Durr, Kamakshi Rao, Moo Sultan, and Dan Crona, for their taking a chance on me and inviting me into the rich history of UNC Pharmacy. Additionally, I would like to thank the absolutely amazing pharmacy residency class of 2016-2017. I would not have enjoyed as much success in graduate school had I not learned countless life lessons from them during residency.

This accomplishment is a testament to the love of my friends and family. Thank you to my friends Jacob, Neil D., Anil , Austin, Raymond, Darvé, Neil T., Daisy, Brian, Justin, Adam, Tyler, Steph, Mary-Haston, Johlee, Lauren, Gerard, and so many others for being there for me. Last but certainly not least, I would like to thank and acknowledge my family: Mom, Dad, Aarthi, and many, many cousins, Aunties and Uncles.

TABLE OF CONTENTS

LIST OF TABLES

LIST OF FIGURES

LIST OF ABBREVIATIONS

3TC	Lamivudine
ABCB1	ATP-binding cassette subfamily B member 1
ABCC1	ATP-binding cassette subfamily C member 1
ABCC2	ATP-binding cassette subfamily B member 2
ABCC4	ATP-binding cassette subfamily B member 4
ABCG2	ATP-binding cassette subfamily G member 2
AIDS	Acquired immunodeficiency syndrome
ART	Antiretroviral therapy
ARV(s)	Antiretroviral(s)
ATV	Atazanavir
AUC	Area under the curve
BCF(s)	B cell follicles(s)
BCRP	Breast cancer resistance protein
BID	Twice a day
BLQ	Below limit of quantitation
BLT	Bone marrow-liver-thymus humanized mouse model
caRNA	Cell-associated RNA
C_{max}	Maximum concentration
dATP	Deoxyadenosine triphosphate
dCTP	Deoxycytidine triphosphate
DNA	Deoxyribonucleic acid
DRV	Darunavir

EC_{90}	90% effective concentration
EFV	Efavirenz
ENT1	Equilibrative nucleoside transporter 1
FDC(s)	Follicular dendritic cell(s)
FTC	Emtricitabine
FTCtp	Emtricitabine triphosphate
GALT	Gut-associated lymphoid tissue
GFR	Glomerular filtration rate
HIV	Human immunodeficiency virus
IC_{50}	50% inhibitory concentration
IC_{90}	90% inhibitory concentration
IHC	Immunohistochemistry
INSTI	Integrase inhibitor
IR-MALDESI	Infrared matrix assisted laser desorption electrospray ionization
ISH	*In situ* hybridization
LC-MS/MS	Liquid chromatography mass spectrometry
LLOD	Lower limit of detection
LLOQ	Lower limit of quantitation
LN	Lymph node
MDR1	Multidrug resistance protein 1
MRM	Multiple reaction monitoring
MRP1	Multidrug resistance-associated protein 1
MRP2	Multidrug resistance-associated protein 2

MRP4	Multidrug resistance-associated protein 4
MSI	Mass spectrometry imaging
MVC	Maraviroc
NDRI	National Disease Research Interchange
NHP	Nonhuman primate
NNRTI	Non-nucleoside reverse transcriptase inhibitor
NNTC	National NeuroAIDS Tissue Consortium
NRTI	Nucleoside/nucleotide reverse transcriptase inhibitor
OATP2A1	Organic anion transporting polypeptide 2A1
OCT3	Organic cation transporter 3
PBMC(s)	Peripheral blood mononuclear cell(s)
PBPK	Physiologically-based pharmacokinetic modeling
PD	Pharmacodynamics
PGP	P-glycoprotein
PI	Protease inhibitor
PK	Pharmacokinetics
PO	Oral
pVL	Plasma viral load
QD	Every day, daily
qPCR	Quantitative polymerase chain reaction
QTAP	Quantitative targeted absolute proteomics
RagHu	hu-HSC-Rag humanized mouse model
RAL	Raltegravir

RNA	Ribonucleic acid
RT-SHIV	Reverse-transcriptase simian/human immunodeficiency virus
RTV	Ritonavir
SHIV	Simian/human immunodeficiency virus
SIL	Stable isotope labeled
SIV	Simian immunodeficiency virus
SubQ	Subcutaneously
TCID	Tissue culture infectious dose
TCIU	Tissue culture infectious units
TDF	Tenofovir disoproxil fumarate
TFV	Tenofovir
TFVdp	Tenofovir diphosphate
PR(s)	Penetration ratio(s)
ZDV	Zidovudine

CHAPTER 1: HIV PERSISTENCE IN THE SPLEEN: OPPORTUNITIES FOR PHARMACOLOGIC INTERVENTION

Summary

The persistence of HIV in the spleen, despite combination antiretroviral therapy (cART), is not well understood. Sustained immune dysregulation and delayed immune recovery, in addition to immune cell exhaustion, may contribute to persistence of infection in the spleen. Eliminating HIV from this secondary lymphoid organ will require a thorough understanding of antiretroviral (ARV) pharmacology in the spleen, which has been minimally investigated. Low ARV exposure within the spleen may hinder the achievement of a functional or sterilizing cure if cells are not protected from HIV infection. Here we provide an overview of the anatomy and physiology of the spleen, review the evidence of the spleen as a site for persistence of HIV, discuss the consequences of persistence of HIV in the spleen, address challenges to eradicating HIV in the spleen, and examine opportunities for future curative efforts.

Introduction

Since the dawn of combination antiretroviral therapy (cART) in 1996, the life expectancy for those living with HIV has increased dramatically to approach near that of non-HIV infected individuals.[1] Following interruption of viral-suppressive therapy, however, rebound viremia occurs after approximately 2-3 weeks.[2–4] It has been estimated that the half-life of HIV from reservoirs is 44 months, indicating that it would take nearly 73 years of continuous suppressive therapy for full eradication from the body.[5,6] The persistence of HIV in the presence of effective cART remains a significant barrier to a cure.

The latent reservoir is established early in infection and comprises of memory and follicular helper T cells.[7] While the hypothesis of active replication occurring in lymphoid tissue remains controversial,[8–10] the persistence of HIV in the lymphoid tissue reservoir has been associated with suboptimal antiretroviral (ARV) concentrations.[11,12] The spleen, a lymphoid organ, is one of the first locations to mount the innate immune response against viral infections, as well as to perform foreign antigen presentation. Recently, the detection of cell-associated viral RNA in spleen tissue may indicate either residual replication or HIV release from stable reservoirs.[13] ARV penetration has been relatively understudied in the spleen. Novel clinical pharmacology tools may provide valuable insight into the persistence of HIV in this lymphoid reservoir with current cART and future eradication interventions. Our group has reviewed the pharmacological challenges and opportunities related to the persistence of HIV in the gut-associated lymphoid tissues[14], yet data regarding the persistence of HIV in the spleen is lacking. Here, we review the anatomy and physiology of the spleen, the evidence of HIV persistence and its consequences, challenges to eradicating HIV in the spleen, and the role of the spleen in future HIV cure therapy.

Anatomy and Physiology of the Spleen

There are two main compartments in the spleen: the red pulp and the white pulp. These two functional units have distinct vascular architecture and cellular compositions. This is a brief review the anatomy and physiology of the spleen, and more in-depth discussions of splenic structure have been previously published.[15–18] Figure 1.1 illustrates the microcirculation of the spleen.

The spleen is comprised of red and white pulp. The red pulp has three main functions: filtering blood, recycling iron (following erthryophagocytosis), and storage of platelets.[16] Splenic

macrophages are responsible for the recycling of iron and compete with bacteria for the utilization of iron for survival. Therefore, the red pulp also serves as a defense against pathogens. Comprising nearly 25% of the splenic tissue, the white pulp contains numerous immunological cells, including – but not limited to – macrophages, dendritic cells, and plasma B cells.[16] T cells are mainly located in the periarterial lymphatic sheaths (PALS, described below). B cells are primarily located in the follicles and are responsible for the production of antibodies following opsonization of foreign antigens (most notably encapsulated bacteria). The marginal zone of the white pulp contains dendritic cells and macrophages responsible for antigen presentation. Blood flow to the spleen ranges from 170-330 mL/min in humans, which is approximately 5% of the total cardiac output.[19] In nonhuman primates (NHPs; a common model for HIV treatment, prevention and cure), blood flow to the spleen is 21 mL/min, close to 2% of cardiac output, although the spleen weighs significantly less (8 grams vs 180 grams in humans).[20] Branching off the abdominal aorta and into the celiac artery, the splenic artery provides oxygenated blood to the spleen. As the splenic artery enters the hilus (fissure) of the spleen, the splenic artery begins to branch off and direct into the fibrous trabeculae. These central arteries are surrounded by lymphatic tissue (PALS) that form the characteristic splenic follicles, comprising the white pulp.[16,17] The central arteries further branch to form penicillar arteries, which enter the red pulp of the spleen. Greater than 90% of the blood flow to the spleen goes to the white pulp, thereby circumventing the red pulp.[21]

There are two morphological components of the red pulp that distinguish it from the white pulp: splenic sinuses (sinusoids) and splenic cords (Cords of Billroth). The splenic sinuses are capillaries lined with discontinuous endothelium as well as slits to perform the sifting of erythrocytes in the spleen. These sinuses eventually form veins (venous sinuses). The splenic

cords are located within the red pulp and comprise of reticular fibers and macrophages. These fibers are composed of collagenous fibers that may be responsible for splenic contraction and are bound by the extracellular matrix and fibroblasts. From a pharmacologic perspective, the morphology of the splenic sinuses allows for not only the permeation of large endogenous molecules, such as albumin, but also large exogenous molecules, such as monoclonal antibodies. For instance, it has been previously demonstrated that rituximab, a monoclonal antibody utilized in the treatment of various cancers and rheumatologically-based conditions, distributes into the spleen.[22–25]

Lastly, blood circulating into the red pulp collect in the venous sinuses that enter the trabeculae of the spleen, through the trabecular veins, and ultimately into the splenic vein. The splenic vein then drains into the hepatic portal vein and into the liver. Therefore, there is both anatomical and physiological communication between the spleen and the liver. Similar to lymph nodes, the spleen contains an efferent lymph vessel that drains into the lymphatic system; unlike the lymph nodes, the spleen does not contain any afferent lymph vessels.[15,16]

Figure 1.1: Physiologic overview of spleen anatomy and physiology

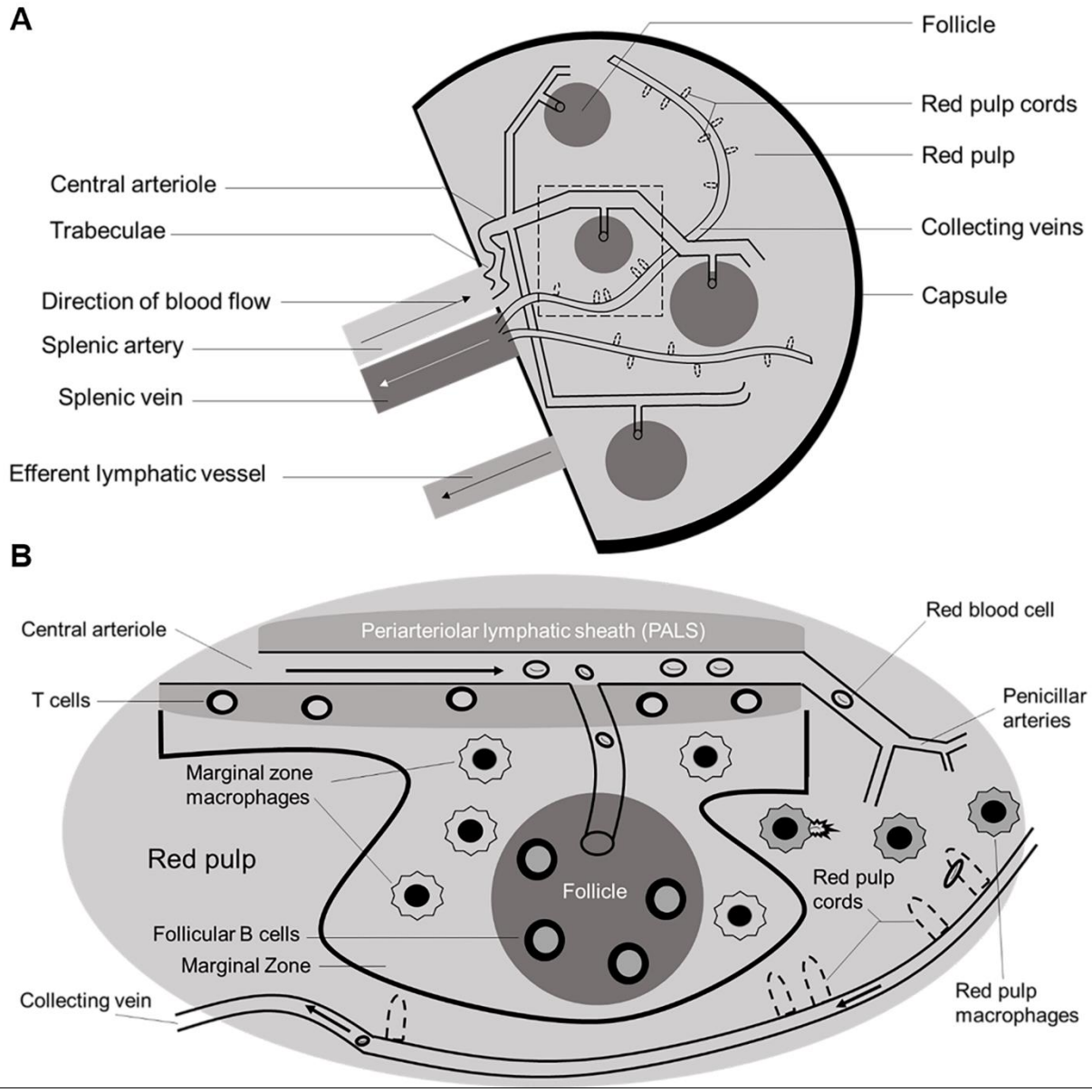

(A) A high-level view of the microanatomy of the spleen. **(B)** An enlarged view of the area within the dotted lines. As blood flows through the central arteriole, smaller arterioles branch off to supply blood into the follicles. The white pulp consists of the periarteriolar lymphatic sheaths (PALS), marginal zone, and follicles. Blood exits the collecting vein located within the red pulp, drains into the splenic vein, and ultimately enters the portal vein. Arrows represent blood flow.

HIV Persistence in the Spleen

Although cART can decrease HIV in the plasma to undetectable concentrations, it cannot completely clear HIV infection from the body. Since <2% of total body lymphocytes are in the blood, it is imperative to examine HIV in anatomical sites.[26] The spleen is the largest secondary lymphoid organ and contains approximately one-quarter of the body's lymphocytes which combines the functionality of the innate and adaptive immune responses. Yet, the spleen is understudied. In 1997, Reinhart et al noted in 8 rhesus macaques infected with SIV $Delta_{B670}$ that the spleen contains 2 x 10^8-10^{10} SIV virions (measured via *in situ* hybridization [ISH] silver staining) and that the viral RNA was observed in the PALS and cells in the red pulp.[27]

Technological advances in quantifying HIV reservoirs has aided in understanding virology and the spatial distribution of virus. These advances include RNAScope and DNAScope, an ISH approach that utilizes "double-Z" target probes to bind in a contiguous fashion to complementary RNA or DNA sequences, respectively.[28] In these scenarios, the probability of two probes adjacently non-specifically binding is low, thereby providing minimal background noise. Deleage et al observed that the B cell follicles of lymph nodes were anatomical compartments for viral persistence, even after 26 weeks of viral suppressive cART to rhesus macaques.[29] The flexibility of this approach allowed for the same authors to demonstrate persistence of SIV RNA on follicular dendritic cells and within the B cell follicles in the spleens of chronically infected rhesus macaques, similar to what had been seen in the lymph nodes.[28] To further provide evidence of viral persistence in the spleen, Estes et al examined 27 rhesus macaques with distinct simian AIDS viruses (9 total spleens) using the RNAScope and DNAScope procedures and demonstrated that even in chronically treated macaques, SHIV and SIV viral RNA persists in the spleen as >99% of the SIV RNA+ cells were located in lymphoid

tissues.[13] Certainly, the presence of virus in the tissue does not necessarily indicate ongoing viral replication, but the numbers of virions seen in these studies indicates the sources of virus that may reemerge following treatment interruption.

There is evidence from post-mortem human spleens that may further indicate persistence of virus. For example, Nolan et al examined the spleens from 5 participants on suppressive cART utilizing droplet digital PCR (ddPCR) and single genome sequencing (SGS).[30] In this analysis, maximum likelihood phylogenies indicated that both the *env* and *nef* viral genes showed viral diversity in the spleen and that because both DNA and RNA sequences were detected in 2 out of 5 patients, this suggested active virus replication.[30] But this is not without controversy. Bozzi et al conducted phylogenetic analyses to investigate HIV populations in infected tissues, including the spleen.[31] The authors did not find evidence of ongoing replication or compartmentalization of HIV within the spleen but did detect clonal expansion of infected cells that predated cART, concluding that the extent of clonal expansion of cells that carry infectious proviruses should be the focus of curative efforts.[31] Therefore, while there may potentially be evidence of actively replicating virus, this is still controversial.

Taken together, there is evidence that suggests HIV persists in the spleen. While much of the conclusions are extrapolated from lymph nodes because of their ability to be extracted for further study, morphological similarities between the two organs might indicate similar processes. Furthermore, splenic data are derived from NHP preclinical models, which can recapitulate the infection process in humans. These data collectively can help inform immune dynamics and viral persistence in the human spleen.

Table 1.1: Macrophage subsets in the spleen and the effect of HIV infection

Macrophage Type	Cellular Marker(s)	Function	Effect of HIV infection[32,33]
Red pulp macrophages	Spi-C[34], F4/80+[35,36], VCAM-1[37], CD163+[38], HO-1[35], ferroportin[35]	• Clearance of effete red blood cells[15] • Iron metabolism[15,34,39] • Scavenging blood-borne debris[39] • Production of type 1 interferons[40]	• Increased in acute infection • Increased in chronic infection
Marginal zone metallophilic macrophages	CD68+[36,39], SIGN-R1[39], CD169[36], sialoadhesin[41]	• Immune surveillance[36] • Degradation and clearance of viruses[42]	• Decreased in acute infection • Decreased in chronic infection
Marginal zone macrophages	CD68+[36,39], CD169+, MARCO[43], LXRα[44], Tim4[44]	• Clearance of blood-borne encapsulated bacteria[44]	• Decreased in acute infection • Decreased in chronic infection
White pulp macrophages (tingible body macrophages)	CD68+[39]	• Phagocytosis of apoptotic B cells within germinal centers[36,44] Regulation of germinal center reactions[44]	• Decreased in acute infection • Decreased in chronic infection (replaced by CD163+ and CD163+/CD68+ macrophages)

F4/80 - epidermal growth factor-like module-containing mucin-like hormone receptor-like 1; VCAM-1 - vascular cell adhesion molecule 1; HO-1 - heme oxygenase 1; SIGN-R1 - specific intracellular adhesion molecule-grabbing nonintegrin receptor 1; MARCO - macrophage receptor with collagenous structure; LXRα - liver X receptor-alpha; Tim4 - T-cell membrane protein 4

Consequences of persistence of HIV in the spleen

Immune dysregulation

Like other pathogenic disease states, the spleen plays an important role in initial antigen presentation and subsequent antibody development against HIV. A key component of the immune cascade is the follicular T helper (Tfh) cell, which is responsible for the development of the germinal center, the site of somatic hypermutation and plasma B cells. Earlier reports indicated that during the acute and chronic phase of HIV infection, frequencies are increased.[45] Conversely, Boswell et al indicated decreased frequencies of Tfh cells.[46] Within lymphoid tissues, Cubas et al noted that the triggering of programmed cell death ligand 1 (PDL-1) on Tfh

cells within the lymph nodes diminishes the B cell responses during HIV infection and potentially lessens control of HIV infection, owing in part due to the reduction in interleukin-21 (IL-21) secretion.[47]

Rodrigues et al noted in a rhesus macaque model infected with *Leishmania infantum*, the abortive differentiation of splenic Tfh cells, relating to the failure of these cells to express PD-1.[48] Ultimately, this led to altered B cell differentiation and reduced production of antigen-specific immunoglobulins. In fact, immunohistochemical (IHC) analysis has indicated the atrophy and disruption of the germinal center during visceral leishmaniasis. In the context of HIV or SIV, Moukambi et al utilized rhesus macaques of Indian origin infected with SIVmac251 and showed that – in the acute phase of infection – splenic Tfh cells decrease early after infection and remodeling of normal splenic architecture occurs.[45] Accompanying the loss of Tfh cells were the loss of memory B cell subsets and lower titers of immunoglobulins against SIV.[45]

Collagen deposition

Mechanisms underlying collagen deposition and subsequent depletion of CD4+ T cells are related to the inflammation and chronic immune activation of HIV infection. Fibrosis in preclinical animal models have indicated the mediator role of transforming growth factor (TGF)-β1 on regulatory T cells in the lymphatic tissues of sooty mangabys and rhesus macaques.[49] These regulatory T cells expressing TGF-β1 were directly linked with collagen type 1 expression in fibroblasts and may lend credence to the notion that suppressive cART does not completely recover T cells or reverse collagen deposition in the lymphatic tissues.[49–51] Due to infeasibility of serial sampling, this has not been holistically demonstrated in the spleen, although red pulp enlargement and lymph follicle atrophy were noted in the spleens from 34 splenectomized patients secondary to hepatosplenic schistosomiasis.[52] Given the morphological and architectural

similarities between lymph nodes and the spleen, similar processes with HIV would be expected, although this has not been confirmed.

In the context of immune system homeostasis, the secondary lymphoid tissues – specifically the spleen – play a vital role. The architecture of these lymphoid organs is ideal to mount an immune response following the introduction of an antigen. For instance, the T cell zone (TZ) is the primary site of HIV activation as the majority of CD4+ T cells reside here.[53] It has been previously demonstrated that the TZ decreases in size during the progression of HIV infection.[54] Schacker et al prospectively examined histological sections of inguinal lymph nodes from HIV-positive patients on suppressive cART and noted depletion of the CD4+ T cell population in all stages of HIV infection associated with deposition of collagen. The area of tissue occupied with collagen was significantly negatively correlated ($r = -0.55$, $p = 0.0008$) with tissue naïve CD4+ T cells.[54] This was further supported by a separate, follow-up study by the same group indicating the deposition of collagen was associated with the depletion and impaired reconstitution of CD4+ T cells.[55] In 2008, Estes et al expanded these findings to the gut-associated lymphoid tissue, demonstrating a significant, inverse relationship ($r = -0.60$; $P = 0.004$) between the percent area occupied by collagen in the T cell zone of the Peyer patches and the CD4+ cell population.[56] Furthermore, treatment in early infection can increase a specific subtype of T cell – CD4+ central memory T cell – in the Peyer patches, even after 6 months of suppressive cART.[56] In the inguinal lymph nodes, Zeng et al noted that collagen damages the fibroblastic reticular cell (FRC) network, contributing to the loss of naïve T cells, mediated by decreased interleukin-7 (IL-7) production and presentation to the FRC, even following suppressive cART administration.[57] Tien et al found that plasma fibrinogen and C-reactive protein were independent predictors of 5-year mortality risk in HIV-infected patients.[58] This

increased inflammatory state secondary to HIV infection causes damage to the lymphoid tissue. Given these results, adjunct antifibrotic and/or anti-inflammatory therapy have been speculated and trialed with mixed results.[59,60]

Inflammatory sequelae

Although cART has allowed for the reconstitution of peripheral CD4+ T cells, HIV-infected adults are at greater risk of non-AIDS-related morbidity, including cardiovascular disease, osteoporosis, and liver disease.[61] One reason for the increased risk of these morbidities is inflammation. A higher frequency of inflammatory monocytes, cytokines, and hypercoaguability biomarkers have been noted, even with consistent, viral-suppressive cART.[58,62–65]

Another key sequelae of the chronic inflammatory state is the activation of macrophages and monocytes. Table 1.1 displays the four main macrophage subsets in the spleen. The activation is accompanied by increased turnover and frequency of circulating monocytes, which may be regulated by the marginal zone macrophages.[66–69] This local, splenic activation may explain the findings seen via IHC. In 72 spleens from post-mortem AIDS patients, histological evidence suggested drastic changes ranging from follicular hyperplasia to follicular atrophy, which had been directly attributable to HIV infection rather than concomitant opportunistic infections.[70] Furthermore, the inflammation resulted in splenomegaly (median splenic weight was 280 grams in those without secondary pathologic lesions).[70] It had been noted from the spleens of these patients that progressive HIV impaired activation of macrophages in the spleen secondary to follicular morphological changes.[70,71]

This was further explored by Williams et al via an accelerated SIV-infected NHP model.[33] In this study, uninfected, acutely infected, infected but asymptomatic, and chronically

infected untreated NHP spleens were immunologically stained for CD163+CD68+ macrophages. Two important findings were demonstrated. First, the immunology of marginal zone macrophages changed during the acute and the chronic phases of infection. In the acute phase, universal upregulation of CD163 was noted, with accompanying loss of CD68 throughout the organ. In the chronic phase, CD163+CD68+ macrophages entered the germinal center to compensate for the acute phase loss of CD68.[33] Second, the authors noted lymphoid depletion, illustrated by hyposplenism, white pulp depletion, and germinal center burn out related to T cell depletion from infection.[33]

Taken together, the pathogenesis of HIV infection directly affects the spleen early in infection and the physical presence of virus in the lymphoid organ causes morphological changes that impair downstream immunological responses. Furthermore, these morphological changes continue to occur in the chronic phase of infection, although the modulatory effect of cART – if present – has yet to be determined.

Challenges to Eradicating HIV in the Spleen

Clonal Expansion

Clonal expansion describes the process of T and B lymphocytes interacting with an antigen or antigen-presenting cell and subsequently generating clones via mitosis against a specific antigen. It has been shown that clonal expansion of HIV-infected cells can persist for over 11 years, even on suppressive cART.[72] Indeed, the identical HIV DNA sequences of infected cells in peripheral blood and tissues lends credence to cellular proliferation being the contributor to the persistence of HIV.[73–75] Lee et al performed cross-sectional genetic analyses on RNA sequences from T cell subsets in blood, lymph nodes, and gut tissues from patients on

suppressive cART for 3-17.8 years and demonstrated two important findings. First, the number of infected memory T cells decreases with cART initiation. Second, effector memory T cells from the lymph nodes can produce infectious virus through clonal expansion. This maintains HIV persistence and offsets the decay of HIV-infected cells.[76] The effector memory T cells from the lymph node contained provirus which was genetically identical to those in plasma.[76]

Similarly, von Stockenstrom et al isolated intracellular HIV-1 genomes from CD4+ T cell subsets from peripheral blood, GALT, and lymph node tissues, from patients receiving suppressive cART, separated by 7-9 months.[77] The authors noted that DNA integrant frequencies were stable over time and that clonally expanded populations were found in effector memory T cells isolated from lymph nodes.[77] While these data are derived from lymphoid tissues, data for the spleen remain sparse, and although morphological similarities between lymph nodes and spleen may permit extrapolation, it is important to be able to examine the spleen directly. Bozzi et al, utilizing phylogenetic analyses of infected post-mortem tissues of treated HIV-infected individuals, did not find evidence of ongoing replication in tissues.[31] In the two spleen samples examined (cART duration: 8.0 and 22.7 years, respectively), there were identical HIV sequences determined via average pair wise differences (0.26% and 1.7%, respectively), compared to the variants sequenced from peripheral blood mononuclear cells (PBMCs) after years of cART.[31] Although this is a sample size of 2, these data do point to the spleen potentially containing clones of virus present prior to starting cART, representing another challenge to fully eradicate HIV.

ARV penetration and modulation

Although the spleen plays a crucial role in immunoregulation, the study of the spleen as a reservoir for HIV is challenging. The spleen is an initial place of antigen presentation, but the in-depth study of the organ is limited to post-mortem individuals or situations in which the spleen must be removed (e.g. splenectomy secondary to ruptured spleen following motor vehicle accident). However, there have been a few studies examining the distribution of ARVs into the spleen of animal models.

Di Mascio et al administered 5 mg/kg intravenous bolus doses of a radiolabeled derivative of tenofovir to Sprague-Dawley rats and detailed the biodistribution of the compound into the spleens after 120 minutes.[78] The authors noted that compared to plasma, splenic concentrations were approximately 2-fold lower.[78] Furthermore, positron emission tomography imaging indicated that a slower accumulation and clearance of the drug from the spleen compared to plasma.[78] Similarly, Lee et al described the biodistribution of a one-time administration of radiolabeled tenofovir disoproxil fumarate to two beagle dogs, which were sacrificed at 24 hours.[79] The percent injected dose per gram of tissue in the spleen observed by Lee et al (<0.01%) was similar to Di Mascio et al (<0.05%).[78,79]

Our group demonstrated that NHPs achieved higher splenic penetration than humanized mouse models or humans alongside higher molar percentages of the active intracellular metabolites of nucleoside reverse transcriptase inhibitors (NRTI), indicating a higher rate of active metabolite conversion.[80] However, for the NRTIs and metabolites in humans, inhibitory quotient values did not exceed 1, which may result in lack of virologic control.[80] In a separate analysis, it was noted that between plasma and tissue concentrations, the NRTIs emtricitabine and tenofovir had positive linear relationships and raltegravir had inconsistent relationships in

the secondary lymphoid organs, highlighting the heterogeneity of ARV penetration into tissues.[81] Fletcher et al examined ARV concentrations in PBMCs and mononuclear cells from lymph nodes, ileum, and rectum, and noted that lower drug concentrations correlated with slower HIV decay rate in the tissues.[12]

All taken together, this would lead one to believe that it is the lack of ARV tissue penetration that contributes to the persistence of HIV. However, this conclusion remains controversial.[31] Should this be the case, drug resistance would likely occur during the setting of subtherapeutic ARV concentrations, as seen in the plasma of patients with poor drug adherence, but this is not observed.[82] Instead, it has been previously noted that the concentrations in tissue reservoirs may be low enough as to not permit the development of resistance, but allows wild-type virus to continue to replicate, thereby outcompeting resistant variants.[83]

Optimizing cART in the spleen is difficult for many reasons. First, as mentioned previously, there are limited data of ARV exposure in the spleen. Additionally, drug transporters and metabolizing enzymes may modulate the disposition of ARVs in the spleen. While a comprehensive discussion of drug transporters is beyond the scope of this review, it is well known that ARVs interact with the ATP-binding cassette (ABC) membrane-associated efflux transporters and solute carrier (SLC) uptake transporters.[84] The expression of these transporters can be altered endogenously or exogenously, thereby affecting ARV concentrations. In preclinical species, quantifiable Mrp4, Bcrp, and Ent1, concentrations have been demonstrated in the spleen, although these did not significantly correlate with ARV concentrations .[80]

Drug metabolizing enzymes (DMEs) are highly responsible for the disposition of ARVs. Macrophages derived from bone marrow and blood express cytochrome P450 (CYP) 1A1, 2A6/7, 2D6, 2E1 and 3A4 mRNA, which are responsible for the biotransformation of numerous

antiretroviral classes, such as protease inhibitors and non-nucleoside reverse transcriptase inhibitors.[85–87] Furthermore, gene expression of DMEs has been shown in human peripheral blood mononuclear cells.[88] While the DMEs in the spleen have yet to be fully characterized, it is possible that due to the wealth of lymphocytes in the spleen, DMEs may play a role in the intracellular disposition and metabolism of small molecules, including ARVs.

The role of inflammation on potential modulation of ARV disposition into reservoir tissues has yet to be elucidated. In the context of antimicrobials, pathophysiological changes in critical illness (alterations in protein binding, pH, etc.) dictated by increases in acute phase proteins affect distribution into the active site of infection, resulting in concentrations below the minimum inhibitory concentration.[89] Although it has been previously demonstrated that the protein binding potential was lower than that in plasma, these values did not differ between NHPs infected with recombinant SHIV versus uninfected controls.[80] Taken together, there may potentially be a role of inflammation or inflammatory sequelae (e.g. collagen deposition as above) associated with HIV infection that modulates ARV penetration and leads to inadequate penetration in lymphoid tissues, but this needs further study.

Future Approaches to Understanding ARV Tissue Distribution

Mass spectrometry imaging

Evaluations of ARVs in tissues have conventionally utilized liquid chromatography-mass spectrometry (LC-MS) of tissue homogenates, which has been regarded as the gold standard of tissue quantification.[90] However, a limitation to this analysis is that tissue homogenates lose spatial and distributional configurations within the tissue due to total consumption of sample. This would lead to significant overestimation of concentrations at the site of action, and

misleading conclusions regarding exposure-response relationships.[91] Our group has demonstrated that distribution of ARVs is not uniform across the tissue reservoirs.[92,93] These data were generated via a novel mass spectrometry imaging (MSI) method known as infrared matrix-assisted laser desorption electrospray ionization (IR-MALDESI).[94,95] The process and workflow of IR-MALDESI has been described previously.[95] IR-MALDESI combines the technical specifications of traditional LC-MS/MS methods, with heat-map style imaging of variable drug concentrations across a snap frozen, unaltered tissue section. Additionally, IR-MALDESI uses ice as a matrix which avoids organic matrix peak interference, allows collection of multiple masses within the tissue, reduces voxel-to-voxel variability and increases sensitivity.[95,96]

The heat-map style imaging data generated from MALDESI requires tissue slices for analyses. Adjacent spleen tissue slices can be sectioned for IHC and ISH analyses and registered with IR-MALDESI images via numerical programming language (e.g. MATLAB) algorithms. Correlation analyses can be assessed qualitatively by visual comparisons and quantitatively through image analysis of the total percentage of the image occupied by a specific ARV (IR-MALDESI), CD4+ cells (IHC), and vRNA/vDNA via RNAScope/DNAScope (ISH). This combinatorial approach that allows for the visualization of ARVs, HIV RNA/DNA, and immunological cells, possibly demonstrating that merely achieving quantifiable splenic ARV concentrations may not be sufficient for effective viral control, as suggested previously.[11,12]

Furthermore, the quantitative data abstracted from IR-MALDESI can lend credence to the ARV concentrations needed within the tissue compartment to suppress virus. Thompson et al assessed the distribution of ARVs in gut tissues across three species and measured the distribution relative to CD3+ T cells and the expression of HIV and SHIV RNA.[93] Across the three species, it was demonstrated that 40-60% of the CD3+ T cells remained unexposed to

ARVs, indicating that ARV exposure in some areas where HIV target cells reside may be limited.[93] These analyses should be similarly performed in the spleen and other tissue reservoirs (lymph nodes, genital tract, etc.) to elucidate the relationship between potential suboptimal ARV exposure and HIV persistence, and represents ongoing work by our group.

Opportunities for HIV Eradication

Small molecules

The concept of "kick and kill" strategies describes latency reversing agents (LRAs) combined with immunotherapeutic intervention, as described below.[97] Numerous LRA classes have been investigated, but the most widely explored are the histone deacetylase inhibitors (HDACi). Deacetylation of histones leads to compacted chromatin, hindering gene expression. Inhibition allows for the unpacking of the chromatin and subsequent immune recognition of the latent cells.[98] Examples of HDACi are vorinostat, panobinostat, and romidepsin.

Data on tissue concentrations of HDACi are scarce. Recently, Perrin et al dosed 3 rats intravenously with 10 mg/kg panobinostat and concentrations in tissues were quantified, and the mean concentration in the spleen was 2.9 μM.[99] Compared to EC_{50} values of HIV-1 wild type and mutant strains determined by Norton et al (1.6-12.86 nM),[100] the concentrations quantified in tissues are over 200-fold higher. Regarding romidepsin, it was noted that when cutaneous burn-injured and control mice were dosed with 5 mg/kg intraperitoneal injections twice daily, there was an increase in histone acetylation.[101] Within the spleen tissue, there was a 17% increase in histone acetylation (a biomarker of romidepsin's effect). This suggests splenic bioavailability of romidepsin, although drug concentrations are unknown. Since LRAs are used in combination with immunotherapeutic agents, a discussion of these follows.

Monoclonal antibody therapy

Monoclonal antibodies represent a novel approach for the treatment and potential eradication of HIV. Most recently, the sole monoclonal antibody approved in the United States for the treatment of HIV infection is the post-attachment inhibitor ibalizumab, which targets the extracellular CD4 domain.[102–106] Due to their designed specificity for a particular antigen, monoclonal antibodies have been utilized for decades in other immune-related diseases, such as cancer, rheumatoid arthritis, and psoriasis. Monoclonal antibodies greatly differ from conventional small molecules as they are highly polar and have molecular weights of approximately 150 kDa.[107] As a result of these different physicochemical properties, distribution of antibodies into tissues occurs primarily through convection.[108–110] Similar to other proteins, monoclonal antibodies experience a sieving process, which is mathematically represented by reflective coefficients. Most tissues have capillary beds comprised of reflective coefficients of 0.95-0.98, indicating virtual impermeability to plasma proteins. In contrast, spleen sinusoidal capillaries contain reflective coefficients of 0.85, lending credence to the notion that plasma proteins circulate into the spleen.[109,111] Indeed, the spleen has been shown to be a preferential site of accumulation of therapeutic antibodies.

FC_{γ} receptors in neutrophils, monocytes, and macrophages are responsible for the internalization and destruction of antibodies.[112] However, binding to FcRn (also known as the Brambell receptor) allows for the recycling of the antibody into the plasma upon acidification.[112] It has been demonstrated that the spleen expresses FcRn receptors.[113] Indeed, in FcRn knockout mice, immunoglobulin accumulation occurred in the liver and spleen, both organs that contain the aforementioned sinusoidal capillary system.[114] A well-documented example is the monoclonal antibody rituximab, which targets splenic antigens (i.e. CD20 antigens on B-cell

splenocytes), and there are numerous references detailing the pathway of rituximab as it relates to the spleen.[22–25] While therapeutic antibodies were proposed initially as a curative strategy for HIV, suboptimal efficacy in preclinical animal models and early unsuccessful clinical trials in humans has tempered enthusiasm. Currently, broadly neutralizing antibodies may potentially regenerate the interest in large, protein therapeutics to treat and prevent HIV infection. While a review of antibody therapeutics is beyond the scope of this manuscript, interested readers are directed to a review by Gruell and Klein.[115]

Adoptive T cell therapy

Another novel approach to HIV therapy is adoptive cell therapy, particularly the engineering of T cells with chimeric antigen receptors (CARs) that are directed towards the HIV envelope.[116] Currently, CAR T-cell therapy is explored and approved for cancer immunotherapies, including B-cell leukemia. In the 1980s, early attempts of CARs utilized soluble CD4 molecules to prevent HIV infection by blocking the interaction between CD4 and the envelope; however, resistance and a short half-life of the soluble CD4 hampered their efficacy.[117,118] Advances have enhanced technical features of T-cell therapies in the context of hematological malignancies. One improved design has been to introduce antibodies against viral antigens versus the extracellular regions of CD4 cells, allowing for specific binding to the viral antigen and limited off-target effects, although differences in affinities of the antibody component are being evaluated.[119,120]

Despite the advancements in T-cell therapies, the pharmacokinetics remain relatively unknown. Biodistribution studies of T cells in mice prepared from splenocytes or tumors concentrated primarily in the spleen and lung after 20-24 hours.[121,122] Early development of mathematical models relied on incomplete biodistribution data or a lack of experimental data.[123]

Khot et al utilized chromium-51-labeled T cells from splenocytes that were expanded using anti-CD3, anti-CD28, and IL-2, and administered to a melanoma mouse model.[124] After noting that the T cells are rapidly cleared from the blood following administration, greater than 90% of the T cells distributed in the spleen, liver, lungs, kidneys, bone, and lymph nodes.[124] Other studies utilized chromium-labeled lymphocytes and noted high body surface counts of lymphocytes in the spleen and liver, both of which have an intricate reticuloendothelial system as aforementioned.[125] More sophisticated mathematical modeling approaches will be warranted to characterize the biodistribution of CAR T-cell therapies that utilize antibodies in the future.

Conclusion

In summary, the spleen is an understudied organ in the context of HIV, and the gaps in knowledge range from ARV concentration analyses to distributional data examining ARVs in relation to immunological cells and virus. HIV infection and immune activation in the spleen leads to potential fibrotic tissue damage that exacerbates immunosuppressive consequences such as CD4+ T cell depletion and inflammation. Initiation of ART reduces viral burden in plasma, but HIV is not fully cleared from lymphoid tissues, which may be caused by inadequate ARV penetration throughout the tissue. Indeed, heterogeneous drug distribution in has been demonstrated, and nonuniform drug coverage of virus – or ARV coverage at subtherapeutic concentrations – provides support for a pharmacologic contribution to viral reservoir persistence. New pharmacologic methods can help bridge these knowledge gaps. These data will help inform HIV treatment and cure clinical trials that would potentially harness immunologically-related therapies with small molecules.

Specific Aims

AIM 1: Identify the effect of infection status, sex, and drug transporter expression on the antiretroviral (ARV) penetration in the spleens of three species (*Chapter 2*)

1a: Quantify ARV concentrations in plasma and spleen tissue homogenates from humanized mice, nonhuman primates (NHPs), and humans using LC-MS/MS methods, and use these concentrations to calculate penetration ratios. Determine if any statistically significant differences in drug concentrations exist based on species, infection status, or sex.

1b: Quantify the protein (NHP, human) expression of drug transporters in spleen tissue using quantitative targeted absolute proteomics methods, and determine if any statistically significant differences in transporter expression exist based on species, infection status, or sex.

1c: Determine if any statistically significant relationships exist between drug transporter expression and ARV penetration in spleens.

AIM 2: Visualize and measure the variability of ARV spatial distribution in the spleens of NHPs (*Chapter 3*)

2a: Using Infrared-Matrix Assisted Laser Desorption Electrospray Ionization (IR-MALDESI), visualize and quantify ARVs in the spleens of NHPs. Compare IR-MALDESI drug concentrations to those determined through LC-MS/MS analyses in Aim 1a. Using quantitative imaging analyses, calculate the percentage of tissue area covered by individual and cumulative ARVs, and the proportion of drug coverage meeting 50% inhibitory concentrations thresholds.

2b: In infected NHPs, perform RNAscope *in situ* hybridization analyses of viral RNA expression within the spleen tissue, and quantify viral load in tissue based on cell associated RNA.

2c: Visualize the distribution of fibrosis markers using immunohistochemistry, and calculate the percentage of tissue area covered by fibrosis response.

2d: Colocalize splenic ARV distribution with viral RNA, and quantify the proportion of virus covered by any drug exposure and by inhibitory drug exposure. Colocalize splenic ARV distribution with fibrosis markers to determine if fibrosis appears to influence patterns of drug distribution.

AIM 3: Develop physiologically-based pharmacokinetic (PBPK) models to simulate the pharmacokinetic profile of two ARVs and their metabolites in the NHP and human spleens (*Chapter 4*)

3a: Develop plasma PBPK models of emtricitabine and tenofovir in NHPs and humans, and optimize parameters by fitting model to observed plasma concentrations from Aim 1a. Perform population simulations, and evaluate model performance by comparing AUC and C_{max} predicted/observed ratios.

3b: Optimize splenic model parameters by fitting to observed splenic parent and metabolite concentrations from Aim 1a.

3c: Calculate tissue penetration ratios using AUCs, and compare trends in splenic penetration between NHPs and humans.

CHAPTER 2: IDENTIFY THE EFFECT OF INFECTION STATUS, SEX, AND DRUG TRANSPORTER EXPRESSION ON THE ANTIRETROVIRAL (ARV) PENETRATION IN THE SPLEENS OF THREE SPECIES

Summary

Adequate antiretroviral (ARV) concentrations in lymphoid tissues are critical for optimal antiretroviral therapy, but there are minimal data on ARV penetration in spleen. This study quantified total and protein-unbound splenic ARV concentrations, and determined whether drug transporters, sex, or infection status were modifiers of these concentrations in animal models and humans. Two humanized mice models [hu-HSC-Rag (n=36; 18 HIV+ and 18 HIV-); bone marrow-liver-thymus (n=13; 7 HIV+ and 6 HIV-) and one nonhuman primate model [NHP; rhesus macaque (n=18; 10 SHIV+ and 8 SHIV-) were dosed to steady-state with ARV combinations. HIV+ human spleens (N=14) from National NeuroAIDS Tissue Consortium were analyzed post-mortem (up to 24h post-dose). ARV concentrations were measured by LC-MS/MS, drug transporter concentrations were measured with LC-MS proteomics, and protein binding in NHP spleens was determined by rapid equilibrium dialysis. Mice generally had the lowest splenic concentrations. Protein binding in splenic tissue was 6-96%, compared to 76-99% in blood plasma, indicating a larger percentage of unbound drug is available for pharmacologic effect. NHPs had quantifiable Mrp4, Bcrp, and Ent1 concentrations, and humans had quantifiable ENT1 concentrations with no significant correlations with tissue ARV concentrations. There was also no influence of infection status or sex. With these dosing strategies, NHP splenic penetration most

closely resembled humans. These data can inform tissue pharmacokinetic scaling to humans to target HIV reservoirs by identifying important species related differences.

Introduction

Combination antiretroviral therapy (ART) has transformed the prognosis of human immunodeficiency virus (HIV) from a fatal to a chronic condition. The life expectancy of a person living with HIV is comparable to that of an uninfected person. Although consistent adherence to ART can produce undetectable HIV RNA in plasma, it has been shown that lifelong therapy is required due to rebound viremia following interruption of therapy.[126,127] Anatomical sites, known as HIV reservoirs or sanctuary sites, may be locations of HIV replication during ART. These include the brain, gut associated lymphoid tissue (GALT), lymph nodes, spleen, and genital tract.[83,128–130] One potential reason for the maintenance of these HIV reservoirs is inadequate antiretroviral (ARV) distribution into tissues. Lower ARV concentrations in GALT and lymph nodes, have been associated with persistent viral replication.[12] However, data regarding ARV penetration into the spleen are lacking, and data on drug distribution into the spleen are limited.[18]

The spleen is the largest secondary lymphoid organ that contains 25% of the body's lymphocytes, and it is a primary site of initial antigen presentation.[16,131] It has been demonstrated in nonhuman primates (NHPs) that early SIV infection of follicular T helper cells remodels splenic lymphoid architecture with indistinguishable T cell areas, B cell follicles, and germinal centers, and disrupts the formation of memory B cells and antibodies to SIV.[33,45] Furthermore, viral RNA persists in NHP spleens despite ART-suppressive therapy of at least 26 weeks in these animals.[13] Viral RNA also persists in post-mortem human spleens collected 4-20 hours after death from patients who were on ART and virologically suppressed in blood plasma.[30,132] As a

result of the role the spleen plays in the immune system, it is imperative to understand its role in HIV in the era of ART.

Previously identified factors that affect drug distribution into HIV reservoirs include sex, drug transporters, and species differences.[133–135] Our group has also characterized drug transporter expression in GALT and lymph nodes.[136,137] In this study, we aim to quantify ARV concentrations and to evaluate these factors affecting ARV distribution in splenic tissues across three commonly used preclinical species – two humanized mouse models and a NHP model [138,139] - and humans.

Methods

Animal studies and spleen collection

The animal study scheme is shown in Figure 2.1. This study used 3 common HIV preclinical models from 2 species: hu-HSC-Rag (RagHu) humanized mice (n=36), bone marrow-liver-thymus (BLT) humanized mice (n=13), and rhesus macaques (NHP) (n=18). All humanized mice and 6 NHPs were female. Aggressive interactions are common between male mice within the same cage, but isolating mice in separate cages can be inefficient and costly. For these reasons, we chose to use only female mice that could be safely kept in groups to minimize cage needs while maximizing animal well-being.[140] RagHu mice (n=18), BLT mice (n=7), and NHPs (n=10) were infected for 6 weeks with $HIV_{BAL\ D7}$ (200 µL, $2.1x10^6$ IU/mL), HIV_{JRcsf} (200 µL, $9x10^4$ TCIU), and RT-SHIV ($10^{4.5}$ $TCID_{50}$), respectively.[141] The remaining animals were uninfected (RagHu n=18, BLT n=6, NHP n=8). After the infection period, animals were dosed for 10 days to steady-state and necropsy was performed one day after the last dose. Doses were chosen based on previously reported effective treatment regimens in these animal models,[142–146] and are reported in Table 2.1. RagHu mice were dosed with efavirenz (EFV) only (n=12),

atazanavir (ATV) only (n=12) or a combination of emtricitabine (FTC), tenofovir (TFV), raltegravir (RAL), and maraviroc (MVC) (n=12). All BLT mice received the 5 drug combination of FTC/TFV/RAL/MVC/ATV (n=13). Finally, NHPs were dosed with FTC/TFV/EFV/RAL (n=9) or FTC/TFV/MVC/ATV (n=9).

At necropsy, plasma and spleens were collected from all animals and snap frozen. Mouse and NHP tissue was divided for use in ARV and transporter expression analyses, with matched data obtained when possible. All animal studies were performed in accordance with Institutional Animal Care and Use Committee protocols from the University of North Carolina at Chapel Hill (protocol 15-168), Colorado State university (protocol 16-6998A), and the University of California Davis (protocol 18345).

Figure 2.1: Animal study dosing and sampling scheme

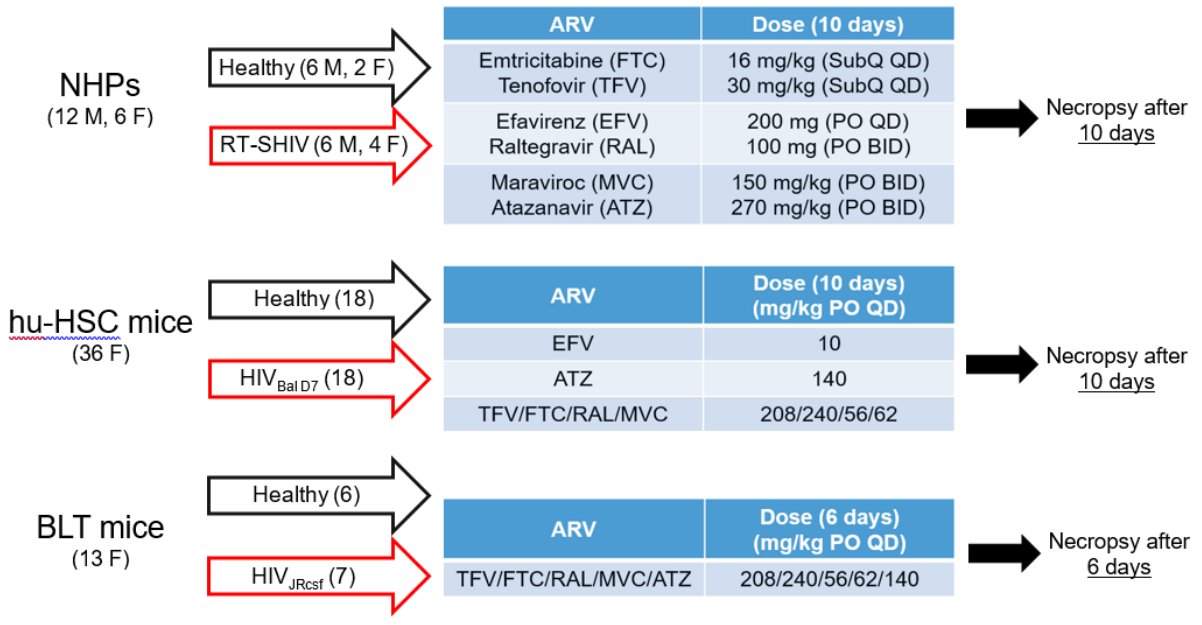

PO, oral; QD, daily; SubQ, subcutaneous; BID, twice daily

Human spleen collection

Human plasma and spleen samples were obtained by the National Research Disease Interchange and the National NeuroAIDS Tissue Consortium from deceased HIV+ patients who consented to organ donation prior to death, or whose families consented to organ donation immediately following the patients' death. To screen for subjects who were adherent to ART or received ARV dosing pre-mortem (and therefore most likely to have quantifiable tissue ARV concentrations), plasma samples were obtained based on desired subject characteristics such as tissue availability, viral load, and ART regimens containing TFV, FTC, EFV, RAL, MVC, or ATV. Plasma samples were analyzed in our laboratory by LC-MS/MS, and only subjects with measurable ARV plasma concentrations were included in the tissue request. Ultimately, spleen sections from 13 subjects (2 female) were requested, and each subject's ART regimen contained at least one drug of interest (8 TFV, 7 FTC, 8 EFV, 3 RAL, 2 ATV, 0 MVC). Human lymph node tissue was divided for use in ARV and transporter expression analyses, with matched data obtained when possible. Details on subject demographics, virology, ART regimens and can be found in Table 2.2.

Table 2.1: Subject demographics and preliminary data of human samples

Sample ID	ARV Regimen	Pre-mortem viral load (copies/mL)	Pre-mortem CD4 count (cells/mL)	Sex	Race	Age at Death (yrs)	First evidence of HIV
7102547787	TFV, FTC, RAL, ETR	20	8	Female	Black	55	2005
1077	TFV, FTC, EFV, APV, AZT	2760	142	Male	White	47	2003
1117*	EFV, ABC, NFV, RTV, AZT	37060	114	Female	Black	Unknown	1990
4077	TFV, FTC, ATV/r	402	3	Male	White	34	1996
4123¶	FTC, EFV	---	398	Male	White	60	1996
6081	TFV, FTC, ATV/r	---	Unknown	Male	White	35	1994
MHBB708¶	RAL, 3TC, AZT	<50	88	Male	Black	63	Unknown
MHBB716¶	TFV, FTC, EFV	<50	597	Male	Black	67	Unknown
MHBB725¶	EFV, 3TC, AZT	<50	106	Male	---	55	1995
MHBB731¶	RAL, ABC, 3TC	<50	503	Male	White	73	1992
10015	EFV, 3TC, d4T	176800	66	Male	White	34	1991
10067	TFV, FTC, EFV, NFV	2097	5	Transgender Male	Asian	27	1990
CA292	TFV, EFV, 3TC	3570	48	Male	White	43	1983
CE150	TFV, EFV, 3TC	25022	17	Male	Native Alaskan	42	1988

---, not available; *witnessed last dose; ¶tissue only

LC-MS/MS analysis of ARV concentrations in plasma and bulk tissue

Concentrations of all 6 ARVs (TFV, FTC, EFV, RAL, MVC, and ATV) were analyzed in plasma and spleen tissue using LC-MS/MS. Additionally, the intracellular active metabolites tenofovir diphosphate (TFVdp) and emtricitabine triphosphate (FTCtp), and their respective endogenous nucleotides, deoxyadenosine triphosphate (dATP) and deoxycytidine triphosphate

(dCTP), were analyzed in spleen tissue. Plasma and tissue samples were extracted by protein precipitation using stable, isotopically labeled internal standards. Extracts were analyzed by a Shimadzu HPLC system with an API 5000 mass spectrometer (SCIEX, Framingham, MA) detector equipped with a TurboIonSpray interface. The lower limit of quantitation (LLOQ) for plasma was 1 ng/mL, and for tissue was 0.002 ng/mL (FTC, MVC), 0.005 ng/mL (EFV, RAL, ATV), 0.01 ng/mL (TFV), 1.11 ng/mL (dATP, dCTP), and 0.22 ng/mL (TFVdp, FTCtp). Assay precision and accuracy was within 15%. At least 30 mg of spleen tissue was homogenized using a Precellys Tissue Homogenizer (Bertin Technologies, Montigny-le-Bretonneux, France) in 1 mL of 70:30 acetonitrile:1 mM ammonium phosphate (pH 7.4) and extracted by protein precipitation as before. TFV and FTC were analyzed using a Waters Atlantis T3 (50mm x 2.1mm, 3 µm particle size) column; EFV, RAL, MVC, and ATV were separated using an Agilent Pursuit XRs 3 Diphenyl (50 mm x 2 mm, 5 µm particle size) HPLC column; TFVdp, FTCtp, dATP, and dCTP were analyzed on a Thermo BioBasic AX column. Concentrations were converted to ng/g based on a tissue density of 1.06 g/mL.

Tissue penetration ratios (PRs) at the end of the dosing interval were calculated for each ARV by dividing spleen concentrations by plasma concentrations. Molar percentages were calculated for the two NRTIs and their metabolites. To calculate molar ratios for the two NRTIs and phosphorylated metabolites, concentrations were converted to mol/g units based on molar mass, summed together to achieve total moles, and the proportions calculated. We also calculated active metabolite to endogenous nucleotide ratios, since the efficacy of the active metabolite depends on its concentration relative to the endogenous nucleotide it replaces during reverse transcription.[147]

ARV tissue protein binding

Protein binding of ATV, EFV, MVC, and RAL, were determined by rapid equilibrium dialysis (RED) previously described.[148] Approximately 20 mg of NHP and human spleen tissue were homogenized in Precellys tubes and incubated at 37^{o}C for 14h (EFV), 16h (RAL, MVC), and 8h (ATV) in rapid equilibrium dialysis cartridges (Thermo Scientific, Pittsburgh, PA, USA). Tissue samples were extracted by protein precipitation with their respective stable labelled internal standard. Samples were analyzed on a Waters Atlantis T3 (50x2.1mm, 3um column) for ATV, RAL, and EFV and Waters XTERRA MS C18 (50x2.1, 3.5um) for MVC. Subsequent detection occurred with a SCIEX API-5000 triple quadrupole mass spectrometer operated in positive ion (ATV, RAL, MVC) or negative ion (EFV) electrospray mode. Assay lower limit of quantification was 0.100 ng/mL (ATV), 0.250 ng/mL (MVC), and 0.400 ng/mL (EFV, RAL). Inter- and intra-day assay precision and accuracy was within 10% of the literature value for the accompanying plasma quality control sample.

ARV 90% inhibitory quotients

The median fraction unbound value was used across all NHP and human spleen tissue samples to calculate the unbound splenic concentrations. The 90% inhibitory quotients (IQ_{90}) were calculated by dividing the unbound splenic concentrations at necropsy (24 hours following administration of the final dose) by the protein-unbound IC_{90} values derived from the literature and utilized previously.[93] Total concentrations were utilized for FTC and TFV due to their negligible protein binding in plasma.[149]

Protein expression analysis

Protein concentrations of 5 efflux and 3 uptake transporters were measured by quantitative targeted absolute proteomics (QTAP).[150] Transporters were chosen based on their relevance to ARV disposition, putative expression in lymphoid tissues, or previous investigation in other reservoir tissues (Table 2.2).[136,151–154] Approximately 100 mg of lymph node tissue was homogenized in 1.3 mL of hypotonic buffer (10 mM NaCl, 1.5mM $MgCl_2$, 10 mM Tris HCl pH 7.4, 150 µL Complete Protease Inhibitor Solution (Sigma Aldrich, St. Louis, MO)) using a Precellys Tissue Homogenizer, and 10-30 µg of membrane protein was isolated as previously described.[136,155] Membrane protein was dried down and reconstituted with 50 mM ammonium bicarbonate buffer plus 40 mM dithiothreitol, 10% sodium deoxycholate, and 10 µL β-casein (0.1 µg/µL). Samples were then reduced for 40 min at 60 ºC followed by addition of 135 mM iodoacetamide and incubation in the dark for 30 min at room temperature. One pmol of stable isotope labeled (SIL) peptide standards (Theracode JPT Inc, Acton, MA) were added to samples, followed by digestion with 25 µL trypsin (0.1 µg/µL) at 37 ºC (Promega, Madison, WI). Digestion was interrupted after 18 h with 10% trifluoroacetic acid, and samples were extracted using solid phase extraction on 33 µm polymeric reversed phase extraction columns (Phenomonex, Torrance, CA). After final dry-down and reconstitution in 98% formic acid (0.1%) plus 2% acetonitrile, around 0.06-0.12 µg of microsomal protein was loaded onto a C18 trap column connected to a BEH130 C18 (150 µm x 100 mm, 1.7 µm particle size) main separation column. Sample analysis was performed on a nanoACQUITY system (Waters, Milford, MA) coupled to a Qtrap 5500 mass spectrometer (SCIEX, Framingham, MA) equipped with a Nanospray III source. Analyst 1.5 and MultiQuant 2.0 software (SCIEX) were used for multiple reaction monitoring (MRM) data acquisition and analysis. Peak area ratios of

unlabeled/SIL peptides were determined using the sum of two MRMs. The lower limit of detection (LLOD) for the peptides was 0.1 pmol/mg protein, and 50 µg NHP liver homogenate was used as a positive control. Concentrations below the LLOQ and above 0.02 pmol/mg protein were imputed as determined, and concentrations below 0.02 pmol/mg protein were imputed as 0.02 pmol/mg protein as previously described.[156]

Table 2.2: Drug transporters used in gene and protein expression analyses

Transport Direction	Gene Name	Protein Name	ARV Substrates	ARV Inhibitors	ARV Inducers
Efflux	*ABCC1*	MRP1	FTC, ATV	FTC, TFV, EFV	
Efflux	*ABCC2*	MRP2	TFV, ATV	FTC, TFV, EFV	MVC
Efflux	*ABCC4*	MRP4	TFV		
Efflux	*ABCB1*	PGP	RAL, MVC, ATV	FTC, EFV, MVC, ATV	FTC, EFV, ATV
Efflux	*ABCG2*	BCRP	TFV, EFV, RAL	EFV, ATV	
Uptake	*SLCO2A1*	OATP2A1	ATV	ATV	
Uptake	*SLC29A1*	ENT1	FTC, TFV		
Uptake	*SLC22A3*	OCT3	3TC		

3TC, lamivudine

Statistical analysis

ARV parent and metabolite concentrations, penetration ratios, gene expression analyses, and transporter concentrations were compared based on infection status, sex (only evaluable for NHPs), and species differences. Comparisons were analyzed via the Kruskal-Wallis One Way ANOVA test followed by Dunn's test with the Holm-Sidek p-value corrections for multiple comparisons. Dichotomous comparisons (i.e. infection status for mice and NHPs and sex for NHPs) were analyzed via the Wilcoxon Rank Sum test. Data are reported as median (interquartile range). All statistical analyses were performed using R 3.6.1 (R Foundation for Statistical Computing, Vienna, Austria) with a significance level of $p<0.05$.

Results

ARV and metabolite drug exposure in the spleen

Of the 18 NHPs in this study, 1 (infected female) was excluded from the analyses due to hepatic failure. Therefore, a total of 17 NHPs were included in the analysis. Due to the similarities in the plasma and tissue concentrations, the analyses performed here pooled the hu-HSC-Rag and BLT mice data. Figure 2.2A shows the distribution of plasma concentrations in the pooled mice, NHPs, and humans. For both NRTIs (FTC and TFV), median pooled mouse plasma concentrations were significantly higher than the NHPs (2.5-fold for FTC and 2.3-fold for TFV) and humans (65-fold for FTC). In contrast, the EFV, RAL, and MVC plasma concentrations were significantly lower in the mice. Infected mice had significantly higher NRTI plasma concentrations than uninfected mice (not shown). In the NHPs, there was no influence of infection status or sex on plasma concentrations (Appendix 2.1 and 2.2).

Figure 2.2B displays the distribution of splenic tissue concentrations in the pooled mice, NHPs, and humans. With a similar trend to plasma, mice had 7.8-fold higher median concentrations of FTC than NHPs and 44-fold higher concentrations than humans. Also similar to plasma, mice had generally lower concentrations of EFV, RAL, MVC, and ATV. There was no influence of infection status or sex on splenic ARV concentrations.

To quantify the proclivity of the ARVs to distribute into splenic tissue, tissue:plasma penetration ratios (PRs) were calculated, and are displayed in Figure 2.2C. For human samples, PRs were calculated on paired samples if plasma and tissue concentrations were available for analysis. Generally, the median PRs were similar across species, although mice FTC PRs were significantly higher than those of NHPs (6.7 vs 2.4; $p<0.01$), and NHP TFV PRs were

significantly higher than both mice (4.7 vs 1.4; $p<0.01$) and humans (4.7 vs 0.7; $p<0.01$). There was no influence of infection status or sex on PRs.

Figure 2.2: Cross-species differences in ARV concentrations and penetration ratios in the spleens

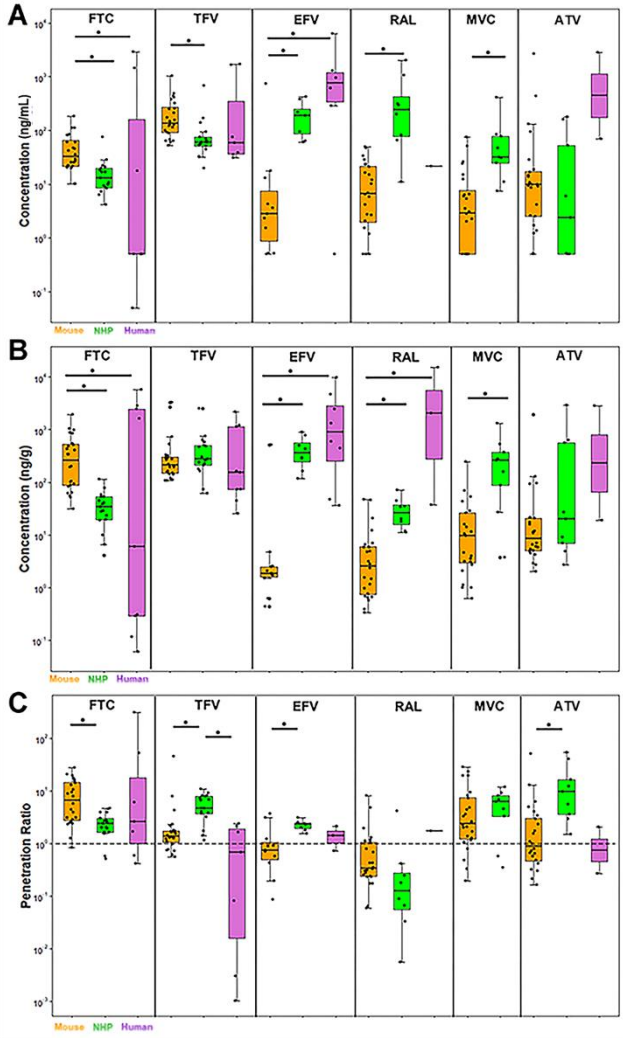

Distribution of plasma concentrations (A), splenic concentrations (B), and penetration ratios (C) for the six antiretrovirals. The dotted line in (c) indicates 1. Mice are in dark grey, nonhuman primates are in light grey, and humans are in white. Boxplots are medians with 25th and 75th percentiles. Whiskers display the data point still within 1.5-times the interquartile range below and above the lower and upper quartile values, respectively. *$p<0.05$ via Kruskal-Wallis One Way ANOVA test followed by Dunn's test with the Holm-Sidek p-value corrections for multiple comparisons. FTC, emtricitabine; TFV, tenofovir; EFV, efavirenz; RAL, raltegravir; MVC, maraviroc; ATV, atazanavir; NHP, nonhuman primate.

Calculated molar percentages are displayed in Table 2.3. In mice and humans, the conversion to the active metabolite for FTC was 0.2%, and for TFV was 2-14%. In the NHPs, however, FTCtp accounted for 22% and TFVdp accounted for 80% of the molar mass. Compared to other species, these differences were statistically significant (all $p<0.05$). There was no influence of infection status or sex on NRTI conversion to metabolite.

Table 2.3: Molar percent of FTC, FTCtp, TFV, and TFVdp

ARV	Mouse	NHP	Human
FTC mol %	99.8 (99.5, 99.9)	77.7 (58.6, 84.6)	99.8 (82.0, 99.9)
FTCtp mol %	0.2 (0.1, 0.5)	22.3 (15.4, 41.4)	0.2 (0.1, 18.0)
TFV mol %	97.4 (96.3, 98.7)	19.7 (8.9, 35.3)	85.7 (70.8, 96.3)
TFVdp mol %	2.6 (1.3, 3.7)	80.3 (64.7, 91.1)	14.3 (3.8, 29.2)

Figure 2.3: Cross-species differences in metabolite and nucleotide concentrations and ratios

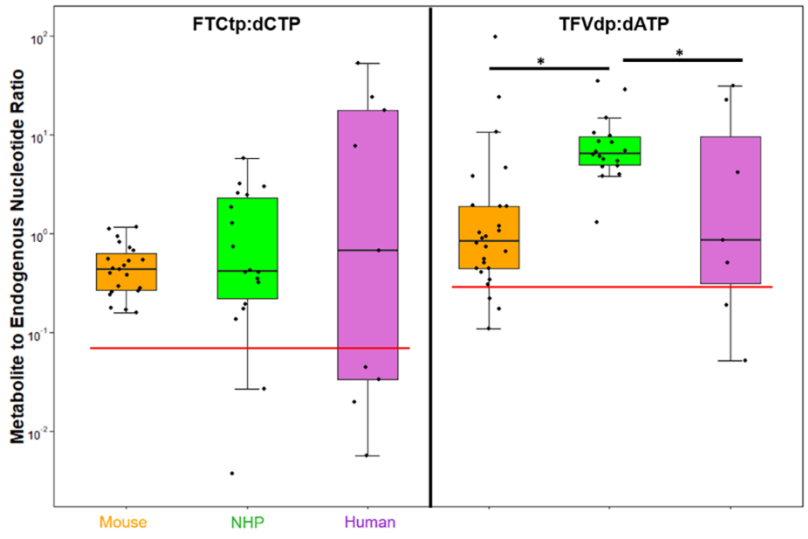

Distribution of metabolite-to-endogenous nucleotide ratios for the two active metabolites. The horizontal red lines indicate the 90% effective ratios from reference #32. Mice are in orange, nonhuman primates are in green, and humans are in lavender. Boxplots are medians with 25th and 75th percentiles. Whiskers display the data point still within 1.5-times the interquartile range below and above the lower and upper quartile values, respectively. *$p<0.05$ via Kruskal-Wallis One Way ANOVA test followed by Dunn's test with the Holm-Sidek p-value corrections for multiple comparisons. FTCtp, emtricitabine triphosphate; dCTP, deoxycytidine triphosphate; TFVdp, tenofovir diphosphate; dATP, deoxyadenosine triphosphate; NHP, nonhuman primate.

Figure 2.3 displays the distribution of NRTI active intracellular metabolite to endogenous nucleotide ratios (MERs) across the three species with reference lines for the EC_{90} derived from peripheral blood mononuclear cells (PBMCs) by Cottrell et al.[157] Median ratios were not statistically different across species and above the respective EC_{90} values. There was no influence of infection status on MERs. However, male NHPs achieved significantly higher FTCtp;dCTP MERs than females (1.6 vs 0.3; p=0.01; Appendix 2.3), although this was not seen with TFVdp:dATP MERs.

Protein binding and IQ_{90} values

Due to the size limitation of mouse spleens, protein binding analysis could not be performed in these models. Additionally, there were only four human spleen samples (1 EFV, 1 RAL and 2 ATV) available for protein binding analyses. Table 2.4 shows the median splenic tissue protein binding for NHPs and humans as compared with the literature-derived plasma protein binding in humans.[158–161] Across the four ARVs that have significant (>75%) protein binding (EFV, RAL, MVC, and ATV) in human plasma, the percent of drug bound to protein in NHP and human splenic tissues was lower than plasma. There were no statistical differences when comparing splenic tissue protein binding potential based on infection status or sex in the NHPs (Appendix 2.4 and 2.5). Furthermore, there were no differences in the distributions of unbound penetration ratios by infection status or sex (Appendix 2.6 and 2.7).

The distribution of IQ_{90} values for the NHPs and humans is displayed in Table 2.4. NHPs achieved significantly higher IQ_{90} values for the active metabolites of the NRTIs (137 vs 0.8 for TFVdp; 9.68 vs 0.07 for FTCtp, respectively with $p<0.001$ for both). In contrast, humans achieved significantly higher median EFV IQ_{90} values than NHPs (17.3 vs 5.08, $p<0.001$). By

infection status, uninfected NHPs achieved higher IQ_{90} values than infected NHPs for RAL (2.6 vs 0.98; p=0.03). There was no influence of sex or infection status on these inhibitory quotients.

Table 2.4: Plasma protein binding in human plasma and spleen for four antiretrovirals in NHPs and human spleen tissues alongside IC_{90} values

Antiretroviral	**Percent bound in human plasma (%)**	**Percent bound in spleen (median [IQR])**		**IC_{90} value (ng/g)**	**IQ_{90} value (median [IQR])**	
		NHP	**Human**		**NHP**	**Human**
FTC	<5	N/A	N/A	84	0.4 (0.2-0.6)	0.07 (0.003-29)
TFV	<5	N/A	N/A	2980	0.09 (0.07-0.2)	0.05 (0.02-0.4)
EFV	99	86 (79-92)	81	10	5 (3.6-8)	17.3 (6.1-53.8)
RAL	83	53 (51-54)	17	10	1.3 (0.8-1.8)	170 (87-722)
MVC	76	11 (10-18)	N/A	6	38 (12.8-55.4)	N/A
ATV	86	49 (38-62)	31 (19-44)	11	0.9 (0.3-26.1)	88.8 (45-133)

Drug transporter expression in the spleen

Figure 2.4 displays drug transporter protein concentrations. Across all nine evaluated transporters, >50% of the mice did not have quantifiable human drug transporter concentrations. NHPs had quantifiable Mrp4 (0.07 [0.02-0.27] pmol/mg protein), Bcrp (1.8 [0.3-5.5] pmol/mg protein), and Ent1 (0.6 [0.4-1.8] pmol/mg protein), concentrations, whereas humans had quantifiable ENT1 concentrations (0.2 [0.02-0.3] pmol/mg protein). Tissue transporter concentrations were higher in uninfected NHPs, reaching statistical significance for Ent1 (1.7 vs 0.5 pmol/mg protein; p=0.02, Appendix 2.8). There was no influence of sex on NHP transporter protein concentrations (Appendix 2.9). There were also no significant correlations between transporter concentrations and ARV tissue drug concentrations or PRs (Appendix 2.10).

Figure 2.4: Cross-species differences in drug transporter expression in spleens

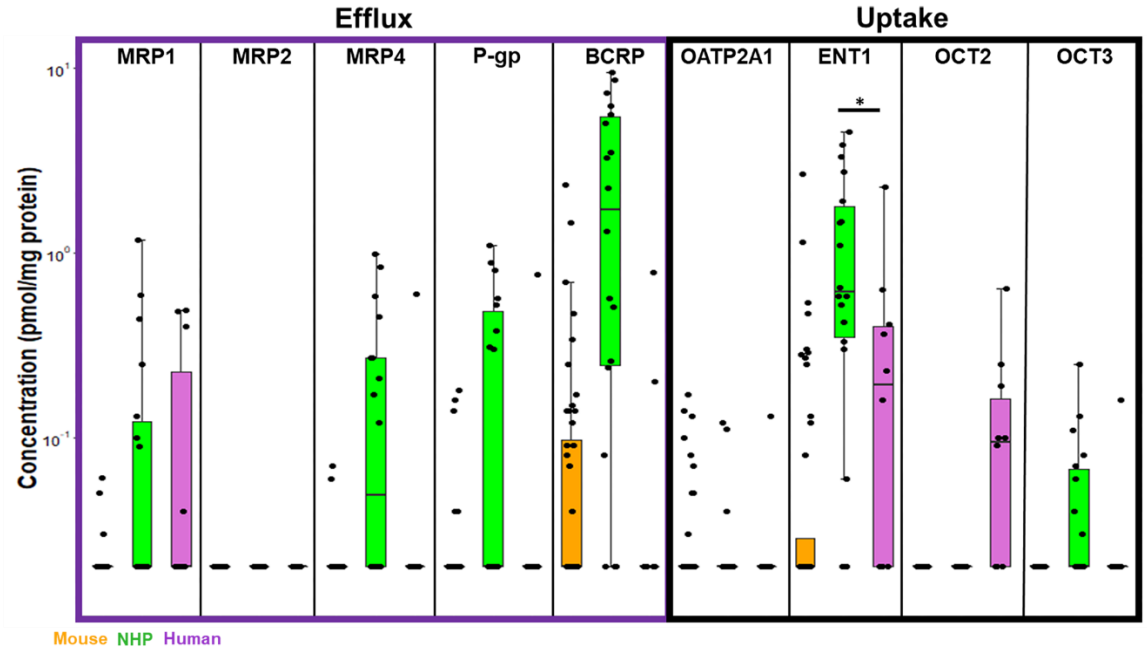

Distribution of drug transporter concentrations. Mice are in orange, nonhuman primates are in green, and humans are in lavender. Boxplots are medians with 25th and 75th percentiles. Whiskers display the data point still within 1.5-times the interquartile range below and above the lower and upper quartile values, respectively. *p<0.05 via Kruskal-Wallis One-Way ANOVA. NHP, nonhuman primate.

Discussion

This is the first analysis investigating potential factors affecting ARV distribution in the spleen across three preclinical species and humans. We have demonstrated several novel findings that have pharmacologic implications for drug development and HIV research. First, we noted species differences in PRs, with NHPs achieved higher PRs than either mice or humans, along with having higher molar conversions to NRTI active metabolites. This also resulted in the highest TFVdp:dATP ratios and were the only species with the MERs wholly above the EC_{90} value. This also was evident with NHPs achieved higher IQ_{90} values than humans for both TFVdp and FTCtp. Second, spleen tissue protein binding was lower than human plasma, which would result in higher IQ values in the spleen. Third, while we detected the drug transporters Mrp4, Bcrp, and Ent1 in NHP spleens and ENT1 in human spleens, there was no association of

protein concentration with splenic ARV tissue concentrations. Finally, we did not note any influence of sex or infection status in tissue drug concentrations.

Drug dosing was chosen based on treatment strategies for animal investigations, which have been adjusted to mimic human plasma exposure.[142,144,145] Since tissue concentrations can be driven by plasma drug exposure, PRs were calculated.[148] Using this ratio, we noted that NHPs and humans had similar drug penetration into the spleen (with the exception of TFV, which was 6.8-fold higher in NHPs), while mice had 3.4-fold lower TFV PRs. Generally, mice, had PRs that were lower than NHPs and humans. This indicates that the penetration of ARVs may vary based on species, whereby ARV splenic penetration is lower in mice and more comparable between NHPs and humans.

We calculated molar percentages of the NRTIs to evaluate conversion to active metabolites. In NHPs, FTCtp and TFVdp exposure relative to FTC and TFV were significantly higher than both humanized mouse models and humans. This is a similar trend to previously published lymph node data.[137] Although the splenic exposures were 4.6-12.5-fold higher, this could be due to the presence of red blood cells (RBCs). Durand-Grassland et al noted TFVdp concentrations were 20% higher in PBMC samples that contained RBCs.[162] Dried blood spot analysis by Adams et al demonstrated TFVdp concentrations were 64% higher in upper-layer packed cells (ULPC) vs PBMCs.[163] Taken together, since the spleen is highly vascularized and clears RBCs with a minor role in erythropoiesis, it is conceivable that the 12.5-fold higher TFVdp metabolite concentrations compared to lymph nodes may be a result of the presence of a wealth of RBCs in the spleen. Furthermore, because >70% of the morphology of the spleen is devoted to the red pulp – which houses RBCs and heme – this warrants future investigation.

The significantly higher percentage of TFVdp in NHPs is also contextualized by a previous study that examined the expression of phosphorylating enzymes in the ectocervix, vagina, and colon of macaques and humans.[164] Adenlyate kinase 2 was shown to be expressed 5- to 15-fold higher in the ectocervical and vaginal tissues compared to what had been observed in humans.[164] This may explain the higher rate of conversion to TFVdp in the spleen tissue, as it has been demonstrated that adenylate kinase is a prevailing enzyme catalyzing the second phosphate group to TFV to form TFVdp.[165] Examining the specific cell types within the spleen tissues of NHPs and humans alongside the possible differential kinases within those cells would shed light on the increased capacity for phosphorylation between species in the spleen.

Protein-unbound concentrations are responsible for pharmacologic effect.[166] Notably, ATV and MVC bind to both albumin and alpha-1-acid glycoprotein (AAG), and RAL and EFV bind primarily to albumin. While we are not aware of albumin or AAG concentration data within the spleen, for all ARVs evaluated, protein binding in spleen tissue was lower than plasma protein binding. EFV concentrations were 86% protein bound in NHP splenic tissue, which is lower than the reported percent bound in plasma (99%) and leads to an increase in free drug concentrations. EFV protein binding was not reduced to the same extent as other ARVs in the spleen. This may be due to the lipophilicity of EFV (log P = 5.4)[167] and its proclivity to be bound to other proteins.[168] We have previously noted a high level of EFV binding in brain tissue in these same animals.[148] A possible explanation for the lower tissue protein binding seen with ATV, RAL, and MVC, is a lower concentration of drug binding proteins in tissue. Indeed, brain tissue albumin concentrations are <1 mg/L versus 35-50 mg/L in plasma.[169] Additionally, previous studies demonstrated <7% MVC protein binding potential in the brain and cervicovaginal fluid, which implies that MVC protein binding is consistently lower across

multiple matrices outside of plasma.[148,170]We are not aware of evidence of additional similar proteins in the spleen, which merits further examination. Protein binding between species is an important consideration, yet ARV plasma protein binding differences is less clear given the lack of studies or data via open-access sources such as Drugs@FDA. Although we saw differences in tissue protein binding with RAL between NHPs and humans, only 1 human sample was able to analyzed, and larger studies would be warranted.

In calculating the splenic ARV IQ_{90} values, we attempted to represent the relationship between drug exposure and efficacy. While IQ data in secondary lymphoid tissues are scarce, we chose a threshold of 1 based on previous literature associating achievement of IQ>1 in plasma with virologic control.[171–173] We used protein-unbound spleen tissue concentrations, which are responsible for pharmacologic activity, for viral activity.[166,174] For the NRTIs and metabolites in humans, IQ_{90} values did not exceed 1; the other ARVs mostly exceeded 1. Feng et al proposed that a mechanism underlying synergy between FTC, TFV, and EFV, was the NNRTI-mediated stable complex formation that would prolong the chain-termination effects of FTCtp and TFVdp in cell cultures and biochemical assays.[175] Taken together, with synergy, perhaps an IQ>1 in tissues is not necessary and that the inclusion of a third ARV agent (as part of guideline-recommended combination therapy) yielded durable and effective therapy. Since the IQ threshold of 1 was associated with virologic control in plasma, it remains to be seen how that may differ in the lymphoid organs.

Drug transporters on cellular membranes are known to efflux or influx ARVs into cells.[134,154] Our drug transporter data were generated by QTAP, which quantifies the amount of drug transporter proteins in a sample. We found three quantifiable drug transporters in the NHP spleen (Bcrp, Mrp4, and Ent1) and one quantifiable drug transporter in the human spleen

(ENT1). Humanized mouse models did not have quantifiable concentrations, which may have been due to our limited sample mass. This was similarly seen when investigating the lymph nodes of these animals. Since BCRP is a heme efflux protein, and the spleen recycles heme and its byproducts, it is not surprising that BCRP was detected.[16,176] Given that EFV is an inhibitor of BCRP[177] and that BCRP has been demonstrated to induce resistance to NRTIs in CD4+ cells[178], it is conceivable that the expression of BCRP was captured by QTAP, and the inhibition provided by EFV administration potentially permitted the greater penetration of concomitant TFV. Second, MRP4 is localized on platelets and is responsible for platelet activation, and the spleen sequesters nearly one-third of the body's platelets.[16,179] Therefore, it's likely that the MRP4 activity in the spleen is not related to ARV activity due to platelet expression, rather than lymphocyte expression. Lastly, Ent1 mRNA has been demonstrated to be present in the spleens of mice and rats[180], and is responsible for the intracellular uptake of nucleosides and nucleoside analogs, (i.e. ribavirin and gemcitabine).[181,182] We hypothesize that this transporter could play a role in the uptake of NRTIs, since ENT1 facilitates the transplacental transfer of abacavir in cell lines and vesicles derived from human term placenta.[183] However, we did not find significant correlations between ENT1 concentrations and NRTI tissue concentrations. However, these previous data have been limited to gene expression analyses, which may be altered in the posttranscriptional processes.[180,184–186] Therefore, with the identification of important drug transporter expression in spleen tissue via QTAP, additional investigations on the location and function of these drug transporters are warranted.

We did not find any significant correlations between the quantifiable ARV-relevant transporters and either tissue concentrations, PRs or PRs corrected for protein binding. This may be because we measured total splenic tissue drug transporter expression rather than membrane-

isolated drug transporter concentration, although previous studies noted that transporter abundance measures are not significantly different when using hepatocytes compared to using liver tissue.[187,188]

Other factors we did not evaluate in this investigation may still exert influence over drug distribution. For example, collagen deposition and lymphatic tissue fibrosis disrupts immune reconstitution after HIV infection, even after ARV therapy is initiated.[55] Additionally, it has been demonstrated that macrophages[85] and lymphocytes[189] express cytochrome P450 drug-metabolizing enzymes, potentially affecting splenic bioavailability. Therefore, it is possible that splenic drug concentrations may be limited to a greater degree by factors other than drug transporters. However, our data suggest this did not affect the penetration of EFV, MVC, and ATV, based on unbound concentrations. We also did not see any substantive influence on drug concentration from infection status and sex. We did see that uninfected NHPs express higher levels of the cellular uptake transporter Ent1, which would theoretically indicate that there would be greater NRTI penetration into the spleen. However, this was not seen when comparing TFV concentrations, correlation coefficients between Ent1 concentrations and TFV tissue concentrations, or molar percentages of the active metabolites. This suggests that although this finding was statistically significant, it may not be clinically relevant.

There are some limitations to this study. First, LC-MS/MS analysis of drug concentrations utilized tissue homogenates, which provides averaged concentrations within pieces of tissue. Therefore, there may be heterogeneous distributional patterns of ARVs within the spleen tissue. Future analyses will utilize mass spectrometric imaging technology to elucidate heterogeneous ARV distribution.[92,93,148] Second, our sample size included 48 mice, 17 NHPs and 13 evaluable human spleen tissues. Yet sex differences could only be evaluated in NHPs; larger

tissue studies from a more diverse population may be warranted to confirm these results. Third, the small sizes of mouse and human tissues precluded a comprehensive analysis for all samples. For example, mice spleen tissues were too small for protein binding experiments and may have been too small to detect appreciable drug transporter concentrations by QTAP. Fourth, results from the QTAP analyses provide protein concentrations, which may not translate to transporter function or localization of transporters within spleen tissue. Fifth, PRs were calculated using single time points at the end of the dosing interval, rather than a true exposure measure (i.e. area under the curve (AUC)), overestimating the penetration of ARVs into splenic tissue since plasma clearance may be faster than tissue clearance. Lastly, as aforementioned, another limitation is the inherent RBC contamination in the homogenate of spleen tissue. Future analyses include harnessing mass spectrometric imaging (MSI) to examine geographical distribution of ARVs in spleen tissue and concomitantly correcting for heme, a marker for blood, which has been performed by our group previously.[93] Nonetheless, these data holistically demonstrate the species differences in splenic ARV penetration and should be understood prior to preclinical pharmacokinetic scaling to humans.

CHAPTER 3: QUANTIFYING AND COLOCALIZING ANTIRETROVIRALS, RT-SHIV, AND FIBROSIS MARKERS IN THE SPLEENS OF NONHUMAN PRIMATES

Summary

Although current antiretroviral therapy (ART) has increased life expectancy, a cure for human immunodeficiency virus (HIV) remains elusive due to the persistence of the virus in tissue reservoirs. In the present study, we sought to elucidate the relationship between ARVs and viral expression in the spleen. We performed mass spectrometry imaging (MSI) of 6 different ARVs, RNAscope in situ hybridization for viral RNA and immunohistochemistry of three different fibrosis markers in the spleens of 8 uninfected and 10 reverse transcriptase simian-human immunodeficiency virus (RT-SHIV)-infected rhesus macaques (infected for 6 weeks) that had been dosed for 10 days with combination ART. Using MATLAB, computational quantitative imaging analysis was performed to evaluate the spatial and pharmacological relationships between the 6 ARVs, viral RNA and fibrotic deposition. In these spleens, 58% of the spleen tissue area was not covered by any detectable ARV response (defined as above the limits of detection for individual ARVs). Maraviroc had the highest median spatial coverage (72% of the spleen tissue area). Moreover, 50% of the infected cells were not exposed to any detectable ARV. Of the quantifiable ARV response colocalized with infected cells, nearly 100% of the response was above the in vitro 50% inhibitory concentrations (IC50), driven by efavirenz and maraviroc. Fibrosis markers covered more than 50% of the spleen tissue area and had negative relationships with the cumulative ARV coverages. Our findings suggest that heterogeneous ARV spatial distribution must be considered when evaluating viral persistence in tissue reservoirs.

Introduction

For over three decades, the mainstay for the treatment of human immunodeficiency virus (HIV) is antiretroviral therapy (ART).[190] Although combination ART has resulted in undetectable plasma viral load (pVL) and an increased life expectancy comparable to those living without HIV, there is not yet a cure.[191] Moreover, lifelong adherence to daily ART is required, as plasma viral rebound occurs after treatment disruption.

The major barrier to a cure for HIV is the persistence of HIV in the body's tissues, known as reservoirs.[192–194] These reservoirs include the gut-associated lymphoid tissue (GALT), lymph nodes (LNs), and the spleen.[194,195] The spleen plays an important role in both the immunological and circulatory systems.[15] The persistence of HIV in spleen may be related to clonal expansion of latently infected cells. For instance, Nolan et al noted that the spleens from 5 participants virally suppressed on ART at time of death contained clonally expanding cells with identical proviral genomes.[30] While the hypothesis of ongoing viral replication within lymphoid tissues was put forth, this remains controversial [83] Recently, Bozzi et al did not detect evidence of genetic changes in HIV sequences – either in blood or tissues – in patients after years of ART, indicating the growing evidence towards clonal expansion.[31] Nevertheless, cure strategies, such as "Shock-and-Kill", will require adequate ART concentrations within deep tissue reservoirs to prevent viral persistence.[196]

Historically, liquid chromatography-tandem mass spectrometry (LC-MS/MS) has been the gold standard for quantifying ARV concentrations in biological matrices. Our group has previously reported ARV concentrations of homogenized spleens from nonhuman primates (NHPs) and humans, and noted large variation of splenic concentrations compared to those in plasma (7.5-fold lower to 9.5-fold higher, depending on the drug).[80] But sample preparation –

specifically whole-tissue homogenization – results in the loss of important spatial information. Elucidating the geographical distribution of ARVs within the tissue is an important next step to study pharmacological efficacy of drugs.[195] Indeed, novel mass spectrometry imaging (MSI) methods in the gut, brain, and LNs have illuminated heterogeneous ARV distribution within those tissue reservoirs.[93,148,197]

Analyses of splenic inflammation and fibrosis in those living with HIV are limited. Histological findings within postmortem spleens of virally suppressed HIV+ patients include inflammation and lymphoid hyperplasia.[132] Given that the spleen is a fibrous organ[16], additional fibrosis may provide a barrier to drug diffusion and distribution. However, the influence of fibrosis on splenic drug distribution is unknown.

Herein, we utilize a novel MSI method known as infrared matrix-assisted laser desorption electrospray ionization (IR-MALDESI) to image 6 ARVs, RNAscope ISH to image viral RNA, and immunohistochemistry (IHC) to image fibrosis markers in the spleens of uninfected NHPs and NHPs infected with reverse transcriptase simian-human immunodeficiency virus (RT-SHIV). Quantitative, computational imaging analysis methods were employed to understand the spatial relationships between these important drug treatment factors.

Methods

NHP study & tissue collection

The NHP study and tissue collection has been described before.[80] Briefly, 18 rhesus macaques (*Macaca mulatta)* were used in this study. Eight NHPs (6 males, 2 females) were left uninfected and 10 NHPs (6 males, 4 females) were infected for 6 weeks with RT-SHIV. pVL was monitored during infection period. After the 6-week infection period, all animals were dosed

to steady-state (8-10 days) with ARV doses based on previously reported effective treatment regimens in this animal model. All NHPs received daily subcutaneous doses of 30 mg/kg of body weight of emtricitabine (FTC) and 16 mg/kg of body weight of tenofovir (TFV) plus one of the following oral combinations: 200 mg of efavirenz (EFV) daily plus 100 mg of raltegravir (RAL) twice daily (FTER regimen; n =9) or 150 mg/kg of maraviroc (MVC) twice daily plus 270 mg/kg of atazanavir (ATV) twice daily (FTMA regimen; n = 9). One day after the final dose, NHPs were euthanized by phenobarbital overdose and necropsy was performed. At necropsy, spleens were collected from each NHP and snap-frozen. All relevant viral load measures are reported in Appendix 3.1. Spleen tissue was stored at -80°C until analysis.

Tissue sectioning

The spleens from each NHP (n=18) were mounted on a specimen disc using O.C.T. (Tissue-Tek; Sakura Finetek, Inc., Torrance, CA) and cryosectioned at -17°C using a Leica CM1950 cryomicrotome (Leica Biosystems, Buffalo Grove, IL) at a thickness of 10 microns. Sections were thaw-mounted onto positively charged glass slides (IHC and ISH) or plain glass slides (IR-MALDESI). Serial sections were collected from each spleen in the following order and quantity for each imaging method: IHC, 3 sections; IR-MALDESI and LC-MS/MS, 6 sections (alternating); and ISH, 2 sections.

LC-MS/MS & IR-MALDESI MSI analyses

NHP 40422, on the FTC, TFV, EFV and RAL regimen, developed liver failure, resulting in plasma drug concentrations 17- to 260-fold higher than for other animals; this NHP was excluded from further analysis. LC-MS/MS methods for spleen tissue homogenate samples have been detailed previously.[80] There had been no (0%) LC-MS/MS concentrations below the limit

of quantification (BLQ). The workflow for IR-MALDESI MSI analyses has been described in greater detail by our group.[197]

Using MATLAB, per-volumetric pixel (voxel) drug response was quantified based on calibration on matched blank spleen tissue.[94] Utilizing a volumetric pixel area of 0.1 mm^2, section thickness of 0.01 mm and a tissue density of 0.00106 g/mm^3, concentrations were converted to units of ng/g tissue. Individual and cumulative (i.e. total ARV responses) ARV maps were corrected for heme contamination and further thresholded by *in vitro* 50% inhibitory concentration (IC_{50}) values to assess the distribution of what might be considered an "effective" ARV concentration in the spleen. The lower limits of quantification for LC-MS/MS (in ng per gram of tissue [ng/g]) were 0.002 for FTC and MVC, 0.005 for EFV, RAL, and ATV, and 0.02 for TFV. The limits of detection for the MSI approach (in ng/g) were 110 for MVC, 130 for ATV, 170 for EFV, 1160 for TFV, 1600 for FTC, and 3040 for RAL. It is important to note that these limits of detection relate to the signal intensity of individual pixels in the image. Because the signal is not uniform across the tissue, the average tissue concentration may be less than the limit of detection, a phenomenon described previously.[198] Therefore, the percent of tissue area occupied by individual ARVs can be measured for all samples, but the quantitation of per-voxel concentrations was more constrained, which is detailed within individual data tables.

The IC_{50} values used in these analyses (in ng/g) were 2.2 for MVC [199], 2.9 for RAL [200], 11.9 for EFV [201], 16.6 for ATV [202], 149 for FTC [203], and 2303 for TFV [203]. To quantify intra-tissue ARV heterogeneity, dynamic ranges (DRs) were calculated as follows: 10 x $\log_{10}$(maximum/minimum intensities).[92]

RNAscope ISH analysis & IHC multiplex

ISH analysis of viral RNA was performed on splenic sections using a modification of the previously published RNAscope protocol.[29,197] Specifically, frozen tissue sections on slides were brought to room temperature and dried for 15 minutes, then incubated for 2 hours in 4% paraformaldehyde (PFA; Electron Microscopy Sciences; Cat. No. 15714-S) fixative in PBS at room temperature and then incubated in 100% ethanol for 5 min x2, then rinsed once in double-distilled water (ddH_2O). Heat-induced epitope retrieval was performed by boiling slides in 1× DAKO target retrieval solution pH9 (Agilent S236784-2) for 5 min, immediately transferred to PBS, incubated in peroxidase blocking solution (3% H_2O_2 diluted in 1x PBS) for 10 min at room temperature, followed by a rinse in double distilled water (ddH2O).

Slides were incubated with the target probe SIV_{mac239} antisense (ACD; Cat. No. 314071) for 2 h at 40°C, and amplification was performed using the RNAscope 2.5 HD Brown detection kit (ACD; Cat. No. 322310) using 0.5× wash buffer (ACD; Cat. No. 310091) in all washing steps. Slides were developed with Alexa Fluor 647-conjugated tyramide (Invitrogen; Cat. No. B40958) at a 1:500 dilution for 2 minutes.

Slides were then stained using rabbit anti-CD4 (Abcam; Cat. No. ab133616, 0143mg/mL) at 1:200 and goat anti-CD20 (Invitrogen; Cat. No. PA1-9024, 0.5 mg/mL) at 1:200 overnight. The slides were then incubated with secondary donkey anti-goat-AF488 (Invitrogen; Cat. No. A11055, 2mg/mL) at 1:200 for one hour and donkey anti-rabbit-AF755 (Invitrogen; Cat. No. SA5-10043, 0.5mg/mL) at 1:200 for one hour. All staining was performed at room temperature, and slides were counterstained with 4′,6-diamidino-2-phenylindole (DAPI; Invitrogen; Cat. No. D1306) at a dilution of 0.5 μg/ml in ddH_2O for 10 min, coverslipped using Prolong Gold antifade

mounting medium, and imaged using a Zeiss scanned on an Axio Scan.Z1 using a Plan Apochromat 20× objective (Zeiss; NA = 0.8, FWD = 0.55 mm).

The relative amount of SIV RNA within infected cells was estimated by quantifying the total SIV RNA signal intensity using the ISH module FISH v1.1 within HALO software (v3.2.1851.393, Indica Labs). We measured the signal intensity (minimum, mean, and maximum) of more than 100 identifiable individual virions within B cell follicles, which corresponds to 2 copies of SIV RNA, then divided by 2 to approximate the signal intensity of a single copy of vRNA. Relative SIV RNA copy number within SIV RNA^+ cells was calculated as (signal intensity within SIV RNA^+ cells [μm^2])/(0.5 × mean signal size for a virion).

IHC analysis for fibrosis markers

To detect collagen type 3, chromogenic immunohistochemistry (IHC) was performed on frozen tissues sectioned at 10 microns. This IHC was carried out using the Leica Bond III Autostainer system. Slides were dewaxed in Bond Dewax solution (AR9222) and hydrated in Bond Wash solution (AR9590). Heat induced antigen retrieval for Collagen III was performed for 20 min at 100ºC in Bond-Epitope Retrieval solution 2 pH-9.0 (AR9640). The antigen retrieval was followed with a 5 min Bond peroxide blocking step (DS9800). After pretreatment, slides were incubated for 1h with Collagen III (1:25) for 30 min. Antibody detection with 3,3'-diaminobenzidine (DAB) was accomplished using the Bond Intense R detection system (DS9263) supplemented with the Novolink Post Primary and Novolink Polymer (Leica, #RE7260-K) secondaries or with the ImmPRESS HRP Anti-Rat IgG (#MP-7444-15, Vector Labs). Stained slides were dehydrated and coverslipped with Cytoseal 60 (8310-4, Thermo Fisher Scientific). Positive and negative controls (no primary antibody) are included for each

assay. IHC stained slides were digitally imaged in the Aperio ScanScope XT (Leica) using 20x objective.

For collagen type 1 and fibrinogen, sequential dual immunofluorescence (IF) was carried out on the Bond fully-automated slide staining system (Leica Microsystems Inc., Norwell, MA) using the Bond Research Detection System kit (Leica, DS9455). Slides were deparaffinized in Leica Bond Dewax solution (AR9222), hydrated in Bond Wash solution (AR9590) and sequentially stained for Collagen I and then Fibrinogen. Specifically, antigen retrieval for Collagen I was performed for 20 min at 1000C in Bond-epitope retrieval solution 2 pH 9.0 (AR9640). After pretreatment, slides were incubated for 2 hours with Collagen I antibody (1:100) followed with Novocastra Post Primary and Novolink Polymer (RE7159 and RE7161, Leica) then TSA Cy5 (FP1117, Akoya Biosciences, Menlo Park, CA). After completion of Collagen I staining, a second round of antigen retrieval was performed for 20 min at 1000C in Bond-epitope retrieval solution 1 pH 6.0 (AR9961). Slides were then incubated with the Fibrinogen antibody (1:1500, 2 hours) then the Novolink Polymer (RE7161, Leica) and detected with TSA Cy3 (FP1046, Akoya Biosciences). Nuclei were stained with Hoechst 33258 (Invitrogen, Carlsbad, CA). The stained slides were mounted with ProLong Gold antifade reagent (Life Technologies, P36930). The antibodies of interest are listed in Appendix 3.2.

Quantitative image analysis and colocalization

The workflow for quantitative imaging analysis of ARVs, fibrosis and viral RNA, has been described previously.[197] Briefly, image analysis and colocalization was performed using MATLAB R2020a (Mathworks, Natick, MA). Final heme-corrected ARV maps generated by IR-MALDESI analyses were overlaid with viral RNA binary images that preserve the areas of the viral RNA by separating the regions from the background (resulting images known as

"masks") to evaluate colocalization, including IC_{50}-thresholded ARV maps to assess virus colocalization with inhibitory drug concentrations. This process was then repeated between fibrosis markers and ARVs. Due to the differences in resolution between IHC/ISH (~0.5 μm/pixel) and IR-MALDESI (100 μm/pixel), virion, cell-associated RNA (caRNA), fibrosis markers, and CD3 masks were downscaled to match the resolution and dimensions of the MSI data, a process known as downsampling.

Statistical analysis

Data are presented as medians (ranges). For these nonparametric data the Mann Whitney *U* test was used for a) differences in raw and heme-corrected individual and cumulative ARV responses and; b) variance in the extent of collagen 1, collagen 3, and fibrinogen coverages between uninfected and RT-SHIV$^+$ spleens. Correlations were assessed via the Spearman rank correlation test for relationships between a) LC-MS/MS and MSI drug concentrations; b) fibrosis and ARV coverages and; c) measures of viral load. All statistical tests were performed using R version 4.0.2 (R Foundation for Statistical Computing, Vienna, Austria). A p-value of <0.05 was considered statistically significant. Initial MSI data processing was performed using the free, open-source MSiReader software (https://www.msireader.wordpress.ncsu.edu/) [204], and quantitative imaging analyses were performed using MATLAB software accessed through a university license (https://www.mathworks.com/products/matlab.html).

Results

MSI analysis of ARVs in spleens

As described in the Methods section, NHP 40422 was excluded due to liver failure; therefore, the total number of NHPs included for analysis was n=17. As **Table 3.1** indicates,

spleen ARV concentrations via quantitative MSI were modestly correlated with LC-MS/MS concentrations after removing the additional outlier uninfected NHP 39510, which received the emtricitabine, tenofovir, maraviroc, and atazanavir regimen. Correlations reached statistical significance for EFV only. Compared to LC-MS/MS, MSI concentrations were approximately 28% lower. Given the large numbers of FTC BLQ values by MSI quantification, subsequent quantitative MSI analyses for FTC were not performed.

Table 3.1: Spleen drug concentrations quantified by LC-MS/MS and MSI

ARV	*n* (*n* BLQ for MSI)	LC-MS/MS concentration (ng/g tissue)	MSI concentration (ng/g tissue)	*rho*	*p*
FTC	17 (14)	27.9 (6.5-45.2)	27.9 (6.5-45.2)	0.3	1
TFV	17 (3)	261 (62-632)	261 (62-632)	0.5	0.1
EFV	8 (1)	505 (3.8-1320)	505 (3.8-1320)	0.1	0.8
RAL	8 (5)	33.9 (4.9-71.3)	33.9 (4.9-71.3)	-1	0.3
MVC	9 (1)	281 (3.7-429)	281 (3.7-429)	0.2	0.7
ATV	9 (3)	17.9 (7.0-27.2)	17.9 (7.0-27.2)	0	1

Data are median (range). MSI concentrations that were BLQ were excluded from this analysis. Correlations (rho) and associated p-values calculated by the nonparametric Spearman's rank correlation. Abbreviations: ARV, antiretroviral; FTC, emtricitabine; TFV, tenofovir; EFV, efavirenz; RAL, raltegravir; MVC, maraviroc; ATV, atazanavir; BLQ, below the limit of quantification; MSI, mass spectrometry imaging.

Figure 3.1 displays representative images of the intensity-scaled and heme-corrected MSI images of the distribution of NHP 42707, an RT-SHIV^{+} NHP treated with the emtricitabine, tenofovir, efavirenz and raltegravir regimen. Heme was present on 37% of this tissue, while heme was present on 40% (range, 17-67%) of all tissues. All analyses focused on heme-corrected ARV concentrations. To visualize the effect of heme contamination, Table 3.2 reports the percentage of the spleen area that registered drug response, both raw and corrected for heme. The heme-corrected cumulative drug response was a median 42% (range, 2-80%) of the spleen tissue area. Correcting for heme contamination reduced drug response by approximately 20%, although

the differences were not statistically significant. Of all ARVs, MVC had the highest coverage across spleen tissue (median 71%), with most concentrations exceeding the *in vitro* IC_{50} value. ARV distributional patterns were heterogeneous as indicated by dynamic ranges summarized in Appendix 3.3 and the MSI images in Appendix 3.4-3.19.

Figure 3.1: Representative intensity-scaled MSI images

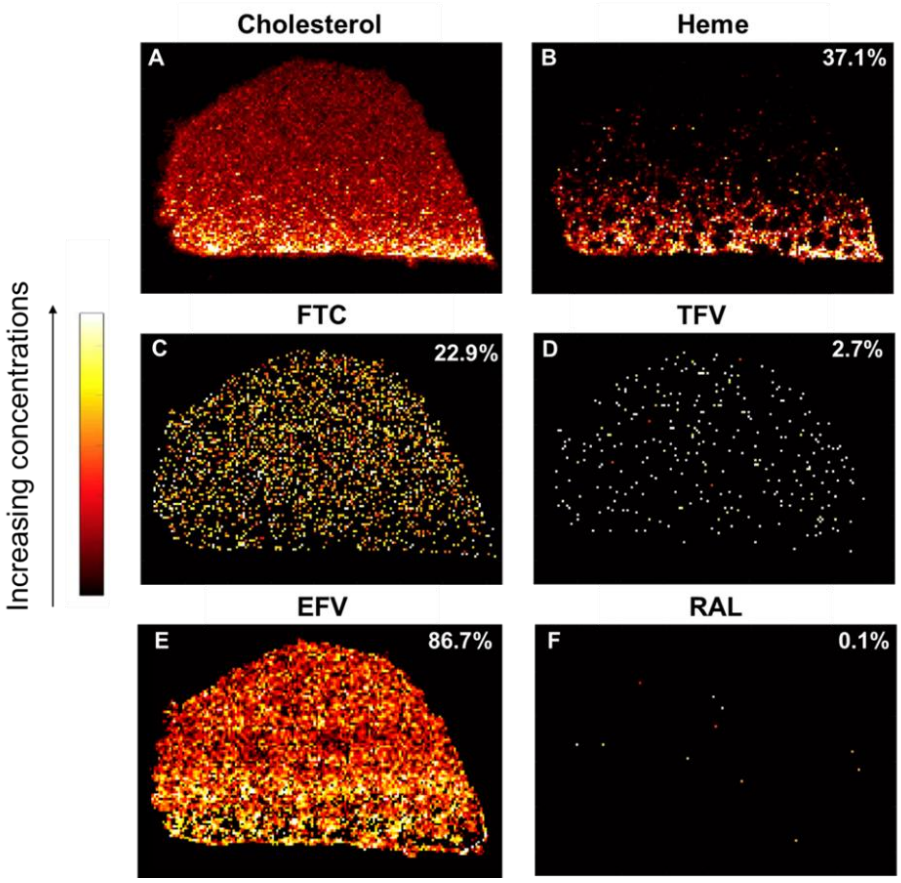

Representative intensity-scaled MSI images of the distribution of cholesterol (A), heme (B), FTC (C), TFV (D), efavirenz (E), and raltegravir (F) in an RT-SHIV+ NHP 42707. Percentages in the top-right corner indicate the MSI area covered by each target. Brighter colors (white and yellow) represent higher MSI signal intensities whereas darker colors (black and red) represent the converse, as indicated by the color bar on the left. Abbreviations: FTC, emtricitabine; TFV, tenofovir; EFV, efavirenz; RAL, raltegravir; MSI, mass spectrometry imaging; RT-SHIV, reverse trascriptase simian-human immunodeficiency virus; NHP, nonhuman primate.

Table 3.2: Spleen area covered by raw and heme-corrected drug response and heme-corrected response greater than the respective IC_{50}

ARV	*N*	Raw	Heme-corrected	Number of NHPs to evaluate per-voxel concentrations	% of heme-corrected ARV area >IC_{50}
FTC	17	0.7 (0.06-45.1)	0.7 (0.05-39.4)	3	---
TFV	17	0.6 (0.2-34.5)	0.5 (0.2-21.3)	14	57.5 (0-100)
EFV	8	15.4 (0.1-96.2)	9.2 (0.1-85.7)	7	100 (100-100)
RAL	8	0.3 (0.1-1.1)	0.3 (0.1-1.1)	3	---
MVC	9	80.1 (1.7-91.8)	71.5 (1.6-79.8)	8	100 (100-100)
ATV	9	0.8 (0.4-53.4)	0.7 (0.3-33.4)	6	---

Data are median (range). Dashes (---) indicate that the low per-voxel sensitivity of FTC and RAL in the spleen tissue precluded per-voxel quantitative analysis to calculate the percent of the heme-corrected area above the respective IC_{50}. P-values calculated via Wilcoxon rank sum test. Abbreviations: ARV, antiretroviral; FTC, emtricitabine; TFV, tenofovir; EFV, efavirenz; RAL, raltegravir; MVC, maraviroc; ATV, atazanavir; NS, not significant; IC_{50}, *in vitro* concentration inhibiting 50% replication.

Examining the coverage of ARVs in spleen tissue slices, in all 17 NHPs, a median of 97% of voxels with detectable drug was due to one ARV only (Figure 3.2). These ARVs were efavirenz and maraviroc. There was a sharp decline in number of voxels that had more than one drug. Sixteen spleens had 2 ARVs colocalized, but this accounted for less than 5% of the tissue area. Twelve NHPs had 3 ARVs colocalized, accounting for 0.3% of tissue area; and 4 NHPs had all 4 ARVs colocalized in a very small percentage of tissue area, ranging from 0.3-3.6%.

Figure 3.2: ARV coverage of spleen tissue area

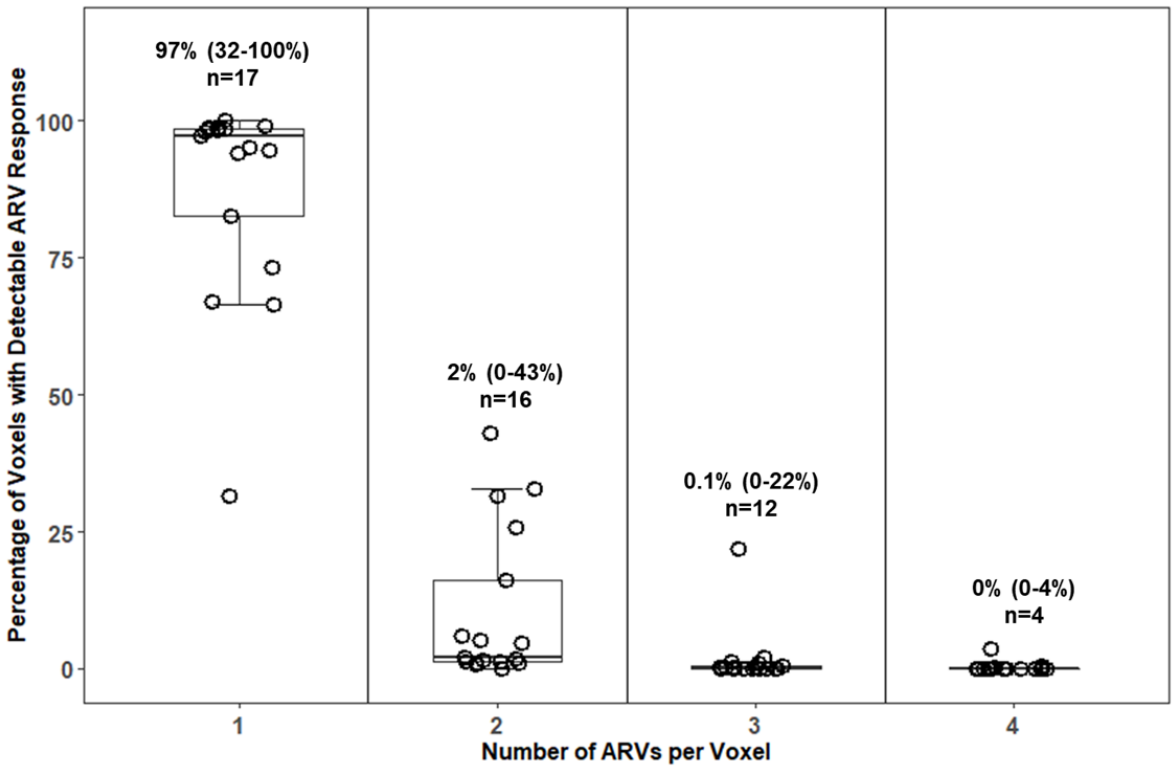

Fraction of spleen area covered by one to four of the ARVs administered in the 4-drug regimen. Data above the boxplots are median (range) percentage of coverage. Sample sizes underneath percentages refer to NHPs containing the specific number of ARVs per voxel. Boxplots represent the median and 25th and 75th percentiles. Abbreviations: ARV, antiretroviral; NHP, nonhuman primate.

Cell-associated RNA and colocalization with ARVs

Representative images of caRNA and detectable drug concentrations are seen in Figure 3.3, and additional viral images are located in Appendix 3.20-3.36. The cell-associated RNA viral load (copies per square millimeter of tissue) was 7.1 (range, 1.6-28.6 copies/mm^2), which amounted to 0.002% (range, 0.002-0.004%) of the tissue area. ARVs were only found to co-localize with caRNA cells in 5 of 9 NHPs, driven by EFV (46%) and MVC (14%), as seen in Table 3.3. RAL and ATV were not detected with any infected cells.

Figure 3.3: Representative images of colocalization between cell-associated RNA and ARVs

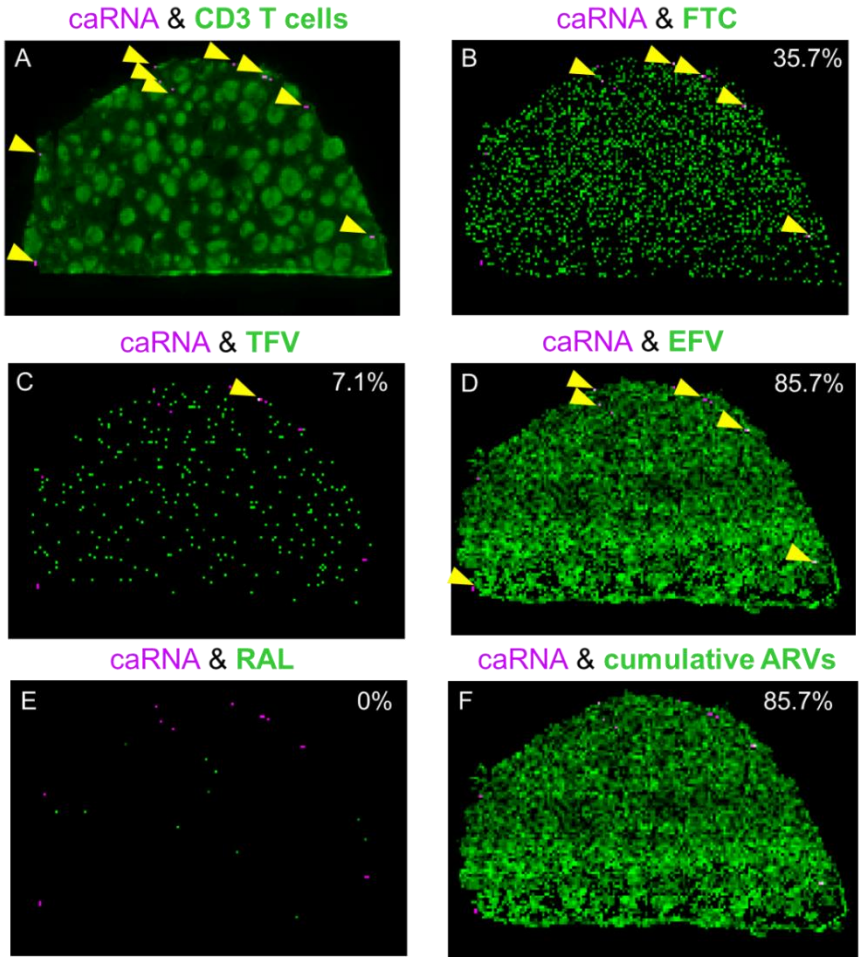

Representative images of the colocalization between cell-associated RNA (magenta) in the RT-SHIV+ NHP 42707: caRNA and CD3+T cells (in green; panel A), caRNA and cumulative FTER (B), and caRNA and individual ARVs (C-F). Percentages in the top-right corner represent the degree of co-localization between ARVs and caRNA. Yellow arrows indicate locations of overlap between ARV and caRNA. Abbreviations: ARV, antiretroviral; FTC, emtricitabine; TFV, tenofovir; EFV, efavirenz; RAL, raltegravir; caRNA, cell-associated RNA; RT-SHIV, reverse transcriptase simian-human immunodeficiency virus; NHP, nonhuman primate.

Table 3.3: Cell-associated RNA covered by any drug response and ARV-covered virus at concentrations greater than the IC_{50}

ARV	*n*	% of virus covered by ARV	Number of NHPs with ARV-covered cell-associated virus	Percent of ARV-covered cell-associated virus with concentrations >IC50
FTC	9	0 (0-35.7)	1	---
TFV	9	0 (0-7.1)	1	100 (100-100)
EFV	4	46.4 (0-100)	2	100 (100-100)
RAL	4	0 (0-0)	0	N/A
MVC	5	14.2 (0-100)	4	100 (100-100)
ATV	5	0 (0-0)	0	N/A
Cumulative	9	44.4 (0-100)	5	100 (100-100)

Data are median (range). Dashes (---) indicate that the low per-voxel sensitivity of FTC in the spleen tissue precluded per-voxel quantitative analyses. N/A indicates that RAL and ATV did not colocalize with cell-associated RNA. Abbreviations: ARV, antiretroviral; FTC, emtricitabine; TFV, tenofovir; EFV, efavirenz; RAL, raltegravir; MVC, maraviroc; ATV, atazanavir;; IC_{50}, concentration inhibiting 50% replication.

Quantitative imaging analysis of fibrosis markers with ARVs

Fibrosis markers covered 62% (range, 49-76%) of the downsampled tissue area. Between the uninfected and RT-SHIV$^+$ NHPs, there was no statistically significant difference in percent coverages of any marker. Correlations between fibrosis marker coverage and individual ARVs were not statistically significant. There were negative relationships between total ARV area coverage versus fibrosis coverage. Only collagen type 3 had a significant negative relationship with total ARV distribution (rho= -0.5; p=0.03; Appendix 3.37).

Discussion

This study explored the spatial relationship of ARVs, RT-SHIV RNA, and fibrosis in the spleens of NHPs using multiple quantitative imaging modalities. The ability to detect FTC and RAL proved to be particularly challenging, producing limits of detection >10x their respective IC_{50} values. Therefore, those were excluded from calculations related to the percent area above inhibitory concentrations in Table 3.1. We noted that for spleen tissue, approximately 20% of the

drug response measured was associated with heme, and was likely due to blood contamination. After correcting for heme, tissue drug distribution was still noted to be diffused throughout the tissue, and the extent of diffusion was drug dependent. Approximately 50% of drug concentrations were above the IC_{50} estimates for TFV, EFV, and MVC. When evaluating TFV, EFV, and MVC, drug detection colocalized with <50% of caRNA. However, when detected, these concentrations were above the IC_{50} values. Finally, while we found a relationship between higher fibrosis marker concentrations and lower drug concentrations for EFV, fibrosis markers may not independently explain low ARV coverage overall.

Previous LC-MS/MS spleen tissue analyses in these NHPs had shown that the three highest ARV concentrations came from MVC, EFV, and TFV.[80] This aligns well with our rankings of the percent of the spleen tissue area occupied by these ARVs using IR-MALDESI. The imaging analyses also demonstrated that these ARV distributions were scattered throughout the spleen and were not necessarily localized to one morphological region. The degree of heme contamination observed in this study is not surprising given the spleen's role in erythrophagocytosis and iron metabolism.[15] Also seen is of the quantifiable drug response, nearly 100% of the responses overall were above the IC_{50} values for TFV, EFV, and MVC.

The finding of incomplete coverage of ARVs with caRNA is similar to our findings with the ileal and rectal tissue, and mesenteric lymph nodes from these same NHPs. [93,197] However, in all of these tissues, nearly 80% of the caRNA was colocalized with ARVs, at concentrations exceeding IC_{50} values.[93]. Furthermore, the large differences in caRNA viral loads seen in the present study in the spleen compared to other known tissue reservoirs.[13,141,196,197,205,206] These data suggest that heterogeneous ARV distribution may contribute to viral persistence in reservoir tissues.

Previous studies hypothesized the role of fibrosis to potentially limit drug disposition in lymphoid tissues, especially in lymph nodes.[54,55] Through IHC imaging and quantitative analysis, over 50% of NHP spleen tissue was inhabited by one of three fibrosis markers studied. Contrary to previous data in mesenteric lymph nodes from these same NHPs, no statistical differences in fibrosis marker concentrations were noted between the spleens of uninfected and RT-SHIV^{+} NHPs. However, given that the spleen is a highly fibrous organ at baseline due to the extensive, fibrillar reticuloendothelial system, detectable increases in fibrosis may be minimal over this short period of time of infection (7 weeks).[15] Since the viral burden was also lower than other tissues, there would reasonably be less immune activation and lower increases in the transforming growth factor β1 (TGF-β1) signaling, which has been previously shown to correspond to the collagen deposition.[49,55,56] Nonetheless, we observed a negative relationship amount of collagen 3 and total ARV tissue distribution (rho= -0.5, p=0.03), lending credence to the hypothesis that for some drugs, fibrosis may limit drug distribution.

The RNAscope analyses permitted us to identify where FDC-trapped virions and caRNA are located within the spleen tissue. As expected, virions were predominantly located within the B cell follicles, where they would be trapped. [29,207,208]. Compared to the LNs from these same NHPs, the caRNA viral load was approximately 10-fold lower in the spleen.[197] This difference had been observed in a previous 26-week longitudinal study of SIV-infected NHPs, where the spleen's contribution to the total viral burden was <1% before and after chronic ART.[13] We did note the significant relationship between the size of the FDC reservoir and the caRNA viral load (rho=0.8, p=0.01), This is aligned with previous findings that demonstrated the correlation of the size of the FDC reservoir and the number of productively infected cells within lymphoid tissues.[207]

The spleen may not be as large of viral reservoir as GALT or LNs, and this might be due to the cellular protective role of the intracellular metabolites of FTC and TFV. Both parent compounds are biotransformed into their active metabolites (FTC triphosphate [FTCtp] and TFV diphosphate [TFVdp] via intracellular phosphorylation. Devanathan et al previously showed that the splenic molar percentages of FTCtp and TFVdp in these spleens, as measured by LC-MS/MS, were 22.3% and 80.3%, respectively.[80] In the LNs and ileal and rectal tissues, these percentages are approximately 5% .[81,137] In the present study, FTC and TFV concentrations were low, and coverage across the tissue, minimal. Therefore, because the active metabolites may be more pharmacologically prevalent, those higher intracellular concentrations could have provided a greater magnitude of cellular protection against viral infection within the spleen. As the sensitivity of the MSI technology precluded the examination of the distribution of the phosphorylated metabolites, this warrants future investigation.

This notable difference between the reservoir size was observed in previous study examining the viral burden in tissues in NHPs before and after 26 weeks of suppressive ART.[13] It was noted that the lymph nodes and gut comprises of over 95% of the total viral burden within the tissue reservoirs; the spleen composed of <0.3%. While the mechanisms behind these stark differences are uncertain, a reasonable hypothesis is that the cellular make-up of the lymphoid tissues is not equivalent. That is, the number and degree of activation of cytotoxic CD8 T cells may permit the greater clearance of viral infected cells. Indeed, the distribution of T-cell subsets is different in the spleen compared to peripheral blood and lymph nodes; the CD4/CD8 ratio in the latter is 2-to-1 whereas in the spleen, it is 1-to-2.[209] Researchers examined this dynamic in cytomegalovirus latently-infected cells and noted this inverted ratio alongside a larger percentage of CD38/HLA-DR double-positive (activated) cyotoxic CD8 T cells and more readily primed

CD4 and CD8 T cells.[209] While the above was demonstrated in cytomegalovirus and because the spleen plays an important role in maintaining cellular immune responses against intracellular pathogens, it is conceivable that this mechanism can be laterally translated to HIV. This hypothesis warrants further investigation, especially over the course of viral infection.

Recently, within the context of HIV cure research, non-nucleoside reverse transcriptase inhibitors (NNRTIs) have demonstrated pyroptotic activity by increasing the intracellular processing of Gag and Gag-Pol within MT4, a transformed T cell line, in a concentration-dependent manner; 50% cytotoxicity occurred at EFV concentrations approximately 1.71 uM (~540 ng/mL).[210] This was further demonstrated in resting and activated primary CD4 T cells, with 50% cell death observed at concentrations ~500 ng/mL.[211] In the 4 infected NHPs herein, median EFV concentrations via MSI and LC-MS/MS were 66 and 183 ng/g, respectively. Interestingly, in our tissues, caRNA displayed a negative relationship with percent EFV coverage across the spleen tissue (rho= -0.8, p=0.2). Further exploration of this finding with tissue-resident cells (e.g. CD4 T cells within the spleen) is warranted.

There are limitations to this study. First, these analyses represent a single point in time (24 hours following necropsy); therefore, it is difficult to extrapolate tissue ARV distribution across a dosing interval, specifically at the times of maximum concentrations, to elucidate dynamic diffusion processes. However, longitudinal sampling across a dosing interval would require a large number of animals which would be technically challenging to implement. Second, a tissue slice, while being 10 microns thick, represent only one two-dimensional examination of a three-dimensional organ. It is conceivable that different sections may have different viral RNA responses and extents of fibrosis. To mitigate this, our measures utilized sections in the middle of the spleens of NHPs to account for potential heterogeneity in responses.

Third, we found lower IR MALDESI sensitivity to ARVs in spleen tissue compared to other tissues from these same animals. Tissue matrix effects were particularly challenging due to either the analytical interference from water in blood plasma or a higher endogenous response in the spleen tissue compared to other tissues. Therefore, limits of detection for FTC, RAL, and ATV, in particular, tended to be higher than their respective IC_{50} values, and precluded quantitative analyses. Fourth, the resolution of MSI images (100 μm/pixel) is lower than IHC/ISH images (0.5 μm/pixel).[96,212] To overlay and coregister MSI and IHC/ISH images, it was necessary to match all images to the resolution of the MSI data. While this likely overestimates the degree of colocalization, this represents the "best case" scenario and any lower colocalization would further confirm the hypothesis of heterogeneous distribution and viral persistence. Nevertheless, the process of downsampling provides novel visualizations of ARVs alongside ISH and IHC images. Further optimization of the IR-MALDESI sensitivity and resolution is ongoing.

In conclusion, we demonstrated the utility of combinatorial imaging modalities to evaluate ARV, viral RNA, and fibrosis distribution in the spleens of NHPs to test the hypothesis that heterogenous ARV distribution permits the persistence of virus. We showed that ARV distribution is heterogeneous in the spleen tissue, although not necessarily caused by fibrosis this early in infection. Yet certain drugs and tissues may be more sensitive to the effects of fibrosis than others. Interestingly, less than 50% of RT-SHIV virions and infected cells were exposed to any detectable ARV, suggesting that there may be a pharmacologic rationale for viral persistence in the spleen. These data not only have implications for drug therapy, but also have implications for the development of "kick-and-kill" cure strategies, which rely on the premise of protective

ARV coverage of uninfected cells during latency reversal in lymphoid tissue reservoirs such as the spleen.

CHAPTER 4: PHYSIOLOGICALLY-BASED PHARMACOKINETIC MODELING OF SPLENIC ANTIRETROVIRAL PENETRATION IN NONHUMAN PRIMATES AND HUMANS

Summary

Combination antiretroviral (ARV) therapy has transformed HIV from a fatal to a chronic condition. However, critical barriers remain due to HIV reservoirs, one of which is the spleen, potentially related to low tissue drug exposure. Splenic biopsies to quantify ARV concentrations carry anatomical and hematological risks, making computational methods to address pharmacokinetics clinically attractive. Here we characterize the exposure of two important ARVs (emtricitabine [FTC] and tenofovir [TFV]) and their active metabolites FTC triphosphate (FTCtp) and TFV diphosphate (TFVdp) in the plasma and spleens of non-human primates (NHPs) and humans. After constructing whole-body physiologically-based pharmacokinetic (PBPK) models, we recapitulated plasma parent and splenic parent and metabolite concentrations in both species. We found a closer alignment of the metabolite half-lives with those of peripheral blood mononuclear cells (PBMCs) versus red blood cells (RBCs). In NHPs, FTC and TFV AUC penetration ratios (PRs) were ~60% lower compared to single-point 24h PRs. By contrast, these were not significantly different in humans. Decreasing partitioning coefficients by 25 and 50% yielded proportional changes in splenic exposure except for FTC in NHPs. Splenic blood flow changes minimally changed C_{max} values, indicating permeability-limited tissue distribution. In this work, we noted important species differences that highlight how tissue penetration should be considered at the sites of action germane to HIV reservoirs during the drug development as

experimental formulations and/or therapeutics are examined for HIV treatment and cure.

Introduction

The advent of combination antiretroviral therapy (ART) in 1996 revolutionized the prognosis of human immunodeficiency virus (HIV) from a fatal to a chronic condition, with the life expectancy of people living with HIV (PLWH) comparable to that of persons living without HIV.[1] Following the interruption of therapy, rebound viremia occurs, indicating that lifelong therapy is required.[5,6] This recrudescence emerges from anatomical sites – also known as reservoirs – and may be locations in which HIV replication/infection occurs despite undetectable HIV RNA in the plasma with consistent ART.[3] Examples of these reservoirs are the brain, lymph nodes, spleen, gut-associated lymphoid tissue (GALT), and the genital tract, with drug exposure being an important factor in virologic response.[12,213]

In addition to inter-tissue variability described above, there is also intra-tissue variability, and elucidating this within-tissue geographical distribution of ARVs is important in studying pharmacological efficacy.[195] This is especially true given the potential overestimation of drug concentrations using tissue homogenates.[91] Indeed, novel mass spectrometry imaging (MSI) computational methods in the gut, brain, and lymph nodes have illuminated heterogeneous ARV distribution within those tissues of NHPs and humans.[93,148,197]

The spleen is the largest secondary lymphoid organ and the primary site of initial viral antigen presentation.[16] Given its importance in the immune system, it is imperative to understand splenic pharmacology. However, routine studies examining ARV exposure in the spleen can't be routinely performed given the invasiveness and hematological risk of a biopsy procedure. Fortunately, computational methods may obviate the need for longitudinal spleen sampling. Specifically, physiologically based pharmacokinetic (PBPK) modeling provides quantitative

characterization of concentration-time curves in these difficult-to-obtain tissues, allowing insight into the cross-species and inter-tissue differences in the distribution of ARVs.[214] Indeed, our group has elucidated cross-species differences in the ARV exposure in the lymph nodes using this PBPK approach.[215] However, no predictive model of ARV exposure in the spleen currently exists.

Given this research gap, we characterized the splenic exposure of two nucleoside reverse transcriptase inhibitors (NRTIs), emtricitabine (FTC) and tenofovir (TFV), as well as their active intracellular phosphorylated metabolites FTC triphosphate (FTCtp) and TFV diphosphate (TFVdp) in nonhuman primates (NHPs) and humans. We then compare these patterns to those of other known putative tissue reservoirs

Methods

PBPK Model Development and Validation

Whole-body PBPK models were developed using the R-based programming package mrgsolve version 0.10.7 (https://mrgsolve.github.io/). Physiologic and drug-specific parameters were derived from previous literature values and drug package inserts.

The constructed plasma PBPK models were validated against concentrations previously reported in the literature; experimental concentration data were derived from NHPs utilizing a previously described dosing regimen [80] and concentrations for human PBPK models were derived from Cottrell *et al.*[157] Plasma validation was determined by the 95% confidence intervals of 2 PK parameters (peak concentration [C_{max}] and area under the curve over the dosing interval [AUC_{τ}]), being between 0.5- and 2-fold within the observed values.

Following the development and validation of the plasma models, models for the NHP and human spleens were similarly constructed with a virtual set of 100 subjects. Penetration ratios

(PRs) were calculated by the AUC of the ARV in the spleen (AUC_{spleen}) divided by the AUC of the ARV in plasma (ARV_{plasma}) and compared to historical PRs.[80] Spleen samples for NHPs were abstracted at one time point (at necropsy, 24h after the dose), and while 13 human samples were obtained from the repository, only 2 could be used based on post-mortem timing and information about drug dosing. This limited the ability to extrapolate regional tissue concentrations more accurately across a dosing interval.

For the formation of the active phosphorylated metabolites within the spleen, parameter values were derived from Garrett *et al*.[216] The dispositional parameters from human peripheral blood mononuclear cells (PBMCs) were optimized to capture the spleen metabolite concentration versus time profiles. The metabolism FTC to FTCtp follows Michaelis-Menten nonlinear formation kinetics, and the metabolism of TFV to TFVdp follows a first-order rate process, as described previously.[216] Concentrations are reported in femtomoles per gram (fmol/g).

Finally, spleen concentration-time profiles were collated and visually compared to previously developed PBPK models in lymph nodes, brain, and gut.[215] This was done across a dosing interval under steady-state conditions. Because the most common cause of treatment failure is nonadherence to ARVs, TFV skipped doses were modeled to examine implications for tissue concentrations, and their relationship to TFV's IC_{50} value (201.6 ng/g).[217]

Sensitivity Analyses

Sensitivity analyses were performed by mimicking clinical scenarios related to HIV-induced inflammation. To mimic the effects of fibrotic deposition in the lymphoid tissues, partition coefficient values were sequentially decreased by 25 and 50%, and the T_{max} values were evaluated. To simulate the effect of hypo- and hypersplenism observed in inflammatory

processes, splenic blood flow was decreased by 50% and increased by 50 and 100%, respectively. The C_{max} parameters were evaluated for comparisons. Fold change from base models are reported as geometric means and 95% CIs.

Software Programs and Statistical Analyses

Statistical analyses and data visualization were performed using R Foundation for Statistical Computing, version 4.0.3 (Vienna, Austria). Non-compartmental analyses (NCA) were performed using Phoenix 64, version 8.2.0.4383 (St. Louis, MO). Data are reported as median with interquartile ranges or geometric mean and 95% CIs as indicated. Comparisons between PRs were assessed via Mann-Whitney *U* test. Correlations between follicular and red pulp concentrations were calculated with Spearman's rank correlation coefficient. P-values < 0.05 were statistically significant.

Results

Plasma Models Validation

Parent plasma simulation models for NHPs and humans were validated, and PK parameters are summarized in Table 4.1. Overall, the models captured the experimental or observed data points well, as seen in Appendix 4.1 and Appendix 4.2 The predicted PK estimates agreed with the observed values, with all parameters and accompanying 95% CIs within the 0.5-2.0 ranges, as described in the Methods section.

Table 4.1: Base model predicted vs. observed plasma parameters for FTC and TFV in NHPs and humans							
ARV	Parameter	NHP			Human		
		Predicted mean	Observed mean	Pred/obs ratio	Predicted mean	Observed mean	Pred/obs ratio
FTC	$AUC_{0\text{-}24hr}$ (ng·hr/mL)	7275	7599	1.0	8657	11074	8657
	$C_{max,0\text{-}24hr}$ (ng/mL)	1631	1251	0.8	1417	1483	1.0
TFV	$AUC_{0\text{-}24hr}$ (ng·hr/mL)	12954	17162	1.3	2610	2585	1.0
	$C_{max,0\text{-}24hr}$ (ng/mL)	2976	2963	1.0	314	337	1.1
Data are geometric means. Abbreviations: FTC, emtricitabine; TFV, tenofovir; NHP, nonhuman primate; Cmax, maximum concentration; AUC, area under the curve							

Spleen Concentration Models - Parent

Similarly, FTC and TFV concentrations in the spleen were visually captured by the models, as seen in Figure 4.1. Concentrations in the spleen across the dosing interval were greater than respective concentrations in plasma. Median (IQR) AUC PRs are summarized in Table 4.2. Compared to the single-point PRs reported previously[80], AUC PRs for NHPs were approximately 60% lower ($p < 0.001$ for both ARVs); these same values were not statistically significantly different for humans.

Figure 4.1: Spleen parent concentration models

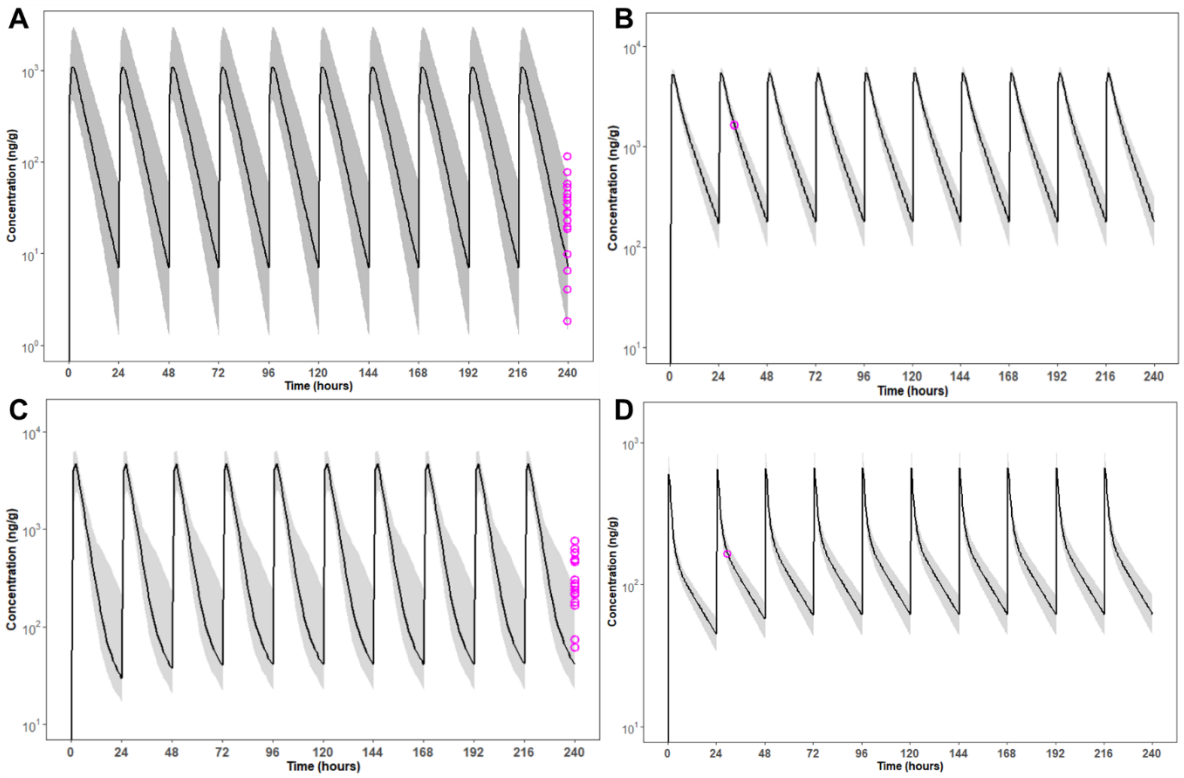

Spleen parent concentration models of FTC (top row) and TFV (bottom row) for NHPs (A and C) and humans (B and D). Solid lines represent median simulated values and gray shading represent the 5th and 95th percentiles. Magenta circles represent individual observed splenic concentrations. Abbreviations: FTC, emtricitabine; TFV, tenofovir; NHP, nonhuman primate.

Table 4.2. FTC and TFV penetration into the Spleens of NHPs and Humans

Antiretroviral	Species	Single-point PRs	AUC PRs	P-value
FTC	NHP	2.4 (1.6 – 3.0)	0.8 (0.7 – 1.0)	<0.001
	Human	2.6 (1.1 – 28.8)	3.3 (2.9 – 3.9)	0.7
TFV	NHP	4.7 (3.7 – 7.8)	1.7 (1.5 – 2.0)	<0.001
	Human	0.7 (0.1 – 1.9)	1.4 (1.3 – 1.5)	0.5

Data are median (interquartile range). P-values calculated via Mann Whitney U test. Abbreviations: FTC, emtricitabine; TFV, tenofovir; NHP, nonhuman primate; PR, penetration ratio.

Spleen Concentration Models – Metabolites

Figure 4.2 displays the active metabolite concentrations versus time profiles for NHPs

and humans. The models visually captured the observed concentration data. For observed FTCtp in human spleens, the point was excluded due to the inability to confirm time after dose. Median (IQR) steady-state half-lives of FTCtp for NHPs and humans were 29.7 hours (22.5-58.8 hours) and 20.9 hours (12.7-39.5 hours), respectively. These values for TFVdp were 121 hours (94.9-181 hours) and 130 hours (127- 135 hours).

Figure 4.2: Spleen metabolite concentration models

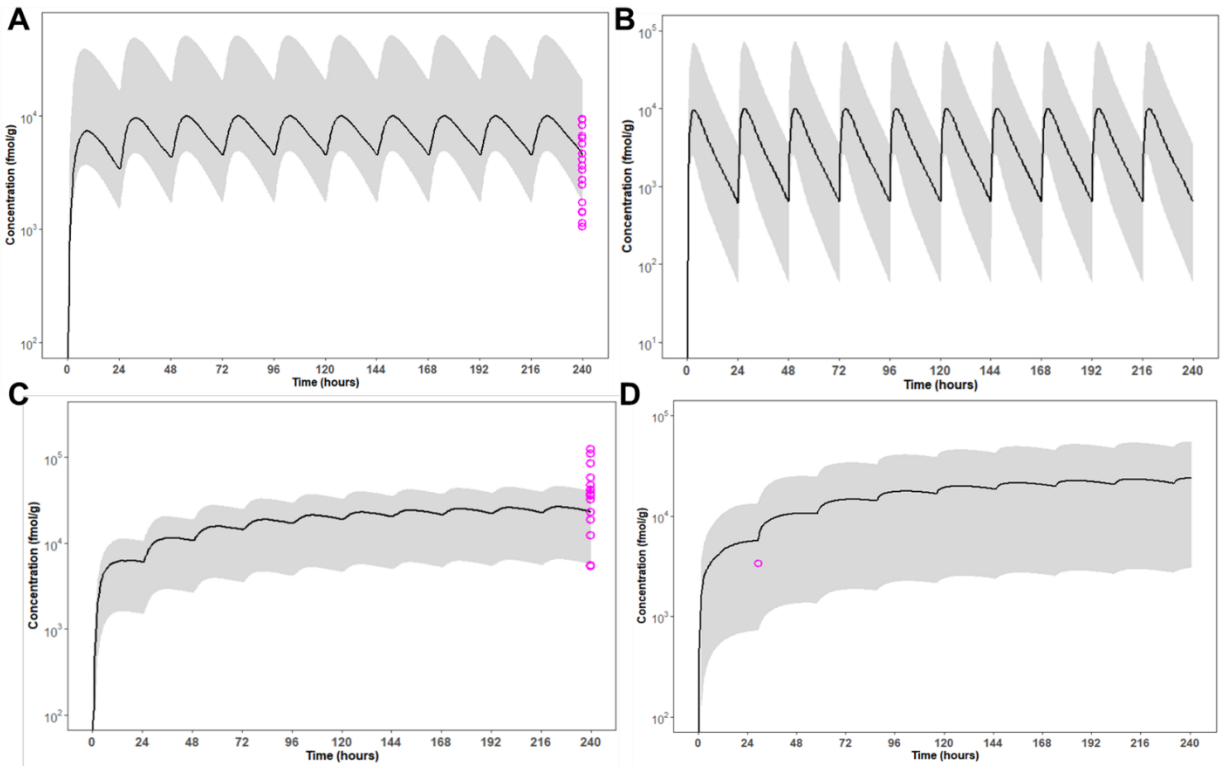

Spleen metabolite concentration models of FTCtp (top row) and TFVdp (bottom row) for NHPs (A and C) and humans (B and D). Solid lines represent median simulated values and gray shading represent the 5th and 95th percentiles. Magenta circles represent individual observed splenic concentrations. Abbreviations: FTCtp, emtricitabine triphosphate; TFVdp, tenofovir diphosphate; NHP, nonhuman primate.

Sensitivity Analyses

Sensitivity analyses for FTC are presented in Tables 4.3 and 4.4. For the NHPs, decreases of 25 and 50% in the partition coefficients did not lead to changes in T_{max} values. Regardless,

partition coefficients remained above 1, indicating a potential preferential distribution into the spleen. As the percent blood flow changed in NHPs, accompanying changes in C_{max} values were of equal magnitude. In humans, the same magnitude decreases in partition coefficients also did not lead to changes in T_{max} values. This contrasts with the changes in percent blood flow where 150 and 200% increases minimally changed C_{max} values.

The effects of changes in partition coefficients and percent blood flow to the spleen for TFV are shown in Tables 4.3 and 4.4. For the NHPs and humans, the decreases of the partition coefficients yielded no changes in the T_{max} values.For both NHPs and humans, changes in splenic blood flow minimally changed C_{max} values.

Table 4.3. Sensitivity analyses for FTC and TFV in NHP spleens

FTC		
Kp	Percent of Base Kp	Tmax (hr)
3.9	100	2.0 (1.6-2.6)
2.925	75	2.0 (1.6-2.6)
1.95	50	2.0 (1.6-2.5)
% blood flow	Percent of base blood flow	Cmax (ng/g)
0.01	100	1012 (478 – 2143)
0.015	150	1372 (688 – 2735)
0.02	200	1652 (773 – 3532)
0.005	50	547 (272 – 1101)
TFV		
Kp	Percent of Base Kp	Tmax (hr)
3.9	100	1.9 (1.2-3.0)
2.925	75	2.0 (1.3-3.1)
1.95	50	1.9 (1.3-2.8)
% blood flow	Percent of base blood flow	Cmax (ng/g)
0.01	100	4527 (1989 – 10302)
0.015	150	4446 (2301 – 8592)
0.02	200	4527 (2281 – 8982)
0.005	50	4544 (2398 – 8611)

Data are geometric mean (95% CI). Abbreviations: FTC, emtricitabine; TFV, tenofovir; NHP, nonhuman primate; Kp, partition coefficient; AUC, area under the curve.

Table 4.4. Sensitivity analyses for FTC and TFV in human spleens		
FTC		
Kp	Percent of Base Kp	Tmax (hr)
3.9	100	1.2 (0.8-1.7)
2.925	75	1.2 (0.8-1.7)
1.95	50	1.1 (0.8-1.6)
% blood flow	Percent of base blood flow	Cmax (ng/g)
0.01	100	5203 (4186 – 6466)
0.015	150	5161 (4191 – 6355)
0.02	200	5340 (4312 – 6615)
0.005	50	4227 (3221 – 5548)
TFV		
Kp	Percent of Base Kp	Tmax (hr)
3.9	100	0.5 (0.4-0.8)
2.925	75	0.5 (0.4-0.8)
1.95	50	0.5 (0.-0.7)
% blood flow	Percent of base blood flow	Cmax (ng/g)
0.01	100	595 (357 – 990)
0.015	150	560 (315 – 994)
0.02	200	575 (341 – 971)
0.005	50	593 (344 – 1021)
Data are geometric mean (95% CI). Abbreviations: FTC, emtricitabine; TFV, tenofovir; NHP, nonhuman primate; Kp, partition coefficient; AUC, area under the curve.		

Discussion

This is the first report of spleen exposure over time for two clinically-relevant ARVs. NHPs have long been utilized to recapitulate the development of HIV infection in mammals, but we noted some species differences between NHPs and humans. Sensitivity analyses suggested that the spleen model is a well-stirred model. No differences were seen in the T_{max} values after changing the partition coefficients, indicating that the organ uptake is rate-limited by blood flow and not permeation across the spleen cell membrane. Ideally, spleen tissue samples taken at approximately the T_{max} would validate these findings.

To overcome overestimation of single-point 24h PRs reported previously, we examined the AUC PRs computationally. This would be particularly important if tissue clearance was slower than plasma clearance, which we have noted before in the female genital tract and intestine.[218,219] We found that the AUC PRs were ~60% lower for FTC and TFV in the NHPs but not in humans. This may be related to higher renal clearance in monkeys for TFV and FTC compared to humans, which would significantly increase the single-point 24h PRs that incorporate merely the 24h concentrations in plasma in the denominator.

This difference between FTC and TFV may be explained by biotransformation into their respective intracellular metabolites. Devanathan et al. previously quantified molar percentages of active metabolites seen in NHP and human spleen tissue homogenates, whereby FTCtp accounted for 22% and TFVdp accounted for 80.3% of total drug load.[80] Higher TFVdp conversion would relate to lower concentrations of TFV across the dosing interval, which was seen here. However, the rates or extent of metabolism may be slower in other extravascular sites, yielding lower metabolite concentrations overall in peripheral tissues, as had been previously seen in the brain.[220]

In this analysis, we found a closer alignment of the metabolite half-lives with those of PBMCs versus RBCs.[221–223]. Since the spleen is home to an extensive mononuclear phagocyte system in the reticular connective tissue located in the red pulp[15], it is conceivable that these cells (red pulp macrophages) and other mononuclear splenocytes are responsible – alongside RBCs – for the intracellular biotransformation of the NRTIs. Additionally, since the spleen clears opsonized effete RBCs that undergo senescent cellular changes, and those changes include a specific loss of protein kinases (e.g. protein kinase C) without significant loss of hemoglobin[224,225], these RBCs may not be converting parent drug to active metabolite as

efficiently in the spleen as in other parts of the circulatory system. This differential intracellular metabolism warrants further investigation within the spleen lymphoid tissue to understand the primary contributor of FTCtp and TFVdp concentrations.

Strategies to enhance ARV exposure in tissues are desired to achieve complete virologic suppression, especially considering the window of time for potential recrudescence that arises following nonadherence. Dyavar et al demonstrated improvements in drug penetration into the lymphoid tissues when using intramuscular and subcutaneous administration of ARVs (versus oral), but decreases within the brain and testes, dependent on the ARV.[226] This variability may be partially explained by the physicochemical properties of the ARVs themselves or enhanced absorption into the lymphatic vessels at the site of injection.[227–229] Long-acting formulations – and thus less frequent administered regimens – are more convenient. To this end, Spreen et al noted that following a single cabotegravir injection to males (n=8) and females (n=8), tissue-to-plasma ratios ranged from 16-28% in the female tract and <8% in rectal tissue, highlighting low penetration into the mucosal tissues.[230] Across different lymph nodes, ratios for cabotegravir following injection ranged from 15-23%.[231] The penetration and pharmacology within tissues of those formulations should be assessed similarly.

There are some limitations to the PBPK analyses herein. First, the parameters for the metabolism of the NRTIs into the respective phosphorylated metabolites were originated from those observed in PBMCs from a validated population pharmacokinetic model.[216] We believe this is a valid assumption given the abundance of immune cells that are capable of the intracellular metabolism within the spleen. Second, the spleen samples for NHPs were abstracted at one time point (necropsy); longitudinal sampling would have allowed for further validation beyond plasma concentrations from these same NHPs. In addition to the spleen samples from

NHPs, our observed spleen tissue data from autopsied humans were sparse and were obtained from very ill patients with many comorbidities, coinfections, and concomitant medications that may have affected plasma and tissue ARV exposure. Furthermore, time points of the model validation data were assumed to be at trough, and we relied on plasma viral load to select validation data that most likely reflected patients at steady-state.

In conclusion, we have developed important PBPK models that recapitulate the penetration of FTC and TFV and their respective phosphorylated metabolites in the spleens of NHPs and humans. Knowing the differential distribution of drugs within tissues assists in understanding risks with nonadherence. Furthermore, as experimental formulations and/or therapeutics are examined for HIV treatment and cure, tissue penetration should be considered at the sites of action germane to HIV reservoirs.

CHAPTER 5: CONCLUSIONS, LIMITATIONS, AND FUTURE DIRECTIONS

As discussed in Chapter 1, the spleen plays a major role in immune functions, containing a wealth of immune cells that highlight its importance as an HIV reservoir during suppressive antiretroviral therapy (ART). This dissertation sought to fill important pharmacology research gaps related to the persistence of HIV in lymphoid tissue by expanding our knowledge of antiretroviral (ARV) pharmacology within the spleen. This was addressed by utilizing a multitude of pharmacologic techniques. Prior to this work, factors (physiologic, biologic, etc.) that affect ARV pharmacology in the spleen was grossly understudied, and the spatial relationship between virus and ARVs within the spleen tissue had never been characterized. Additionally, there had been no data related to the comparisons between and among species utilized in HIV pharmacology research.

To this end, Chapter 2 explored the influence of drug transporters, sex, and viral infection on the penetration of six ARVs in the spleens of three species. Tissue penetration ratios provide a normalization procedure of tissue concentrations against the accompanying plasma concentrations at the end of a drug dosing interval. Calculating these penetration ratios, we determined that the drug penetration into the spleen differed by ARV, and maraviroc, efavirenz, and tenofovir penetrated to the greatest extent, while raltegravir was lowest. These trends were generally consistent across species. Furthermore, we did not find meaningful differences in penetration into the spleen based on sex or viral infection. We had found that the protein binding potential in the spleen tissue was lower than that in plasma. This indicates a higher percentage of

the drug is available to exert the pharmacologic effect. Basing effective drug concentration on plasma for the spleen tissue would be erroneous as the higher protein binding potential in the plasma would potentially underestimate the efficacy for drugs that are highly protein bound. Utilizing quantitative proteomics techniques, drug transporter expression was overall minimal in the spleen tissue. We did not find a statistical relationship between drug transporters and ARV tissue concentration, suggesting a more passive process of ARVs distributing into the spleen tissue.

The limitations of the experiments detailed in Chapter 2 included blood contamination in tissue homogenates. While this is a concern for all tissue, it's notable in the spleen. Also, the penetration ratios in the spleen were calculated using only one time point rather than exposure over a dosing interval, which was addressed in Chapter 4. While these specific limitations were addressed, there are a number of limitations that remain, many of which are ripe for future investigation, as discussed below.

Metabolizing enzymes and their individual pharmacogenetic variations may influence ARV concentrations within the spleen tissue, but was not explored here. However, according to The Human Protein Atlas (www.proteinatlas.org), RNA or protein expression of many different drug metabolizing enzymes for ARVs (i.e. CYP3A4, CYP3A5, UGT1A1) is negligible .[232] Alternatively, the quantification of known metabolites of ARVs that are metabolized by these enzymes may shed light on the capability of metabolism within the spleen: an area for future work.

The transporter analyses discussed herein also had limitations. First, drug transporters selected in these analyses were based on associations with ARVs and known expression in other tissue reservoir locations (i.e. brain, gastrointestinal tract, etc.). We did detect three transporters

within the spleen tissue: BCRP, MRP4, and ENT1. These align well with previous analyses of lymph nodes from these same animal models, suggesting transporter expression related to lymphoid tissues.[137] However, the analyses by themselves do not account for transporter activity. To this end, we performed immunohistochemistry (IHC) imaging of these three transporters in spleen tissue sections, but colorimetric staining was generally nonspecific; this made it difficult to determine if transporters were located on the cellular membranes or in the cytoplasm. We had encountered tissue quality issues during staining analyses, potentially due to elapsed time and/or freeze/thaw cycles. For future studies, focus should be placed on tissue integrity, particularly cellular integrity via novel embedding media or limiting time between necropsy and analysis.

The tissue imaging as previously discussed in Chapter 3 was performed through multiple methods and analysis workflows. Our aim was to quantify the variability of the distribution of ARVs within the spleen tissues of the nonhuman primates (NHPs) alongside viral RNA and fibrosis markers. While nearly 100% of the detected ARV exposure exceeded inhibitory concentrations, approximately 50% of the spleen tissue area was not covered by any ARV, and coverage of the remaining area was primarily due to maraviroc or efavirenz. However, to the degree of assay sensitivity and specificity, approximately 50% of the cell-associated viral RNA was unexposed to any ARV. Regarding fibrosis markers, 49-76% of the spleen tissue was covered, but did not appear to influence drug distribution patterns and was not significantly increased in infected tissues. As discussed in Chapter 3, this may be due to both the high baseline fibrous nature of the spleen tissue and the shorter duration of infection.

Our findings from Chapter 3 have important implications for the HIV cure field and help address the limitations in characterizing ARV pharmacology within tissue reservoirs. As previously mentioned, conventional methods (i.e. LC-MS/MS) utilize tissue homogenates, and

ARV concentrations are averaged across the mass of the tissue homogenized. They do not account for the spatial drug heterogeneity that our group has previously shown in the intestines, brain, and lymph nodes.[93,148,197] The implication is that this method may inaccurately predict true drug exposure in the spleen tissue. Additionally, blood contamination is especially concerning for the spleen tissue, given its role in erythrophagocytosis.[15] In Chapter 3, we accounted for the spatial drug heterogeneity and heme contamination via our MSI methodologies, and found that the heme contamination decreased concentrations by 40%; this would be the same biopsies of tissues where blood contamination is an issue with the procedure.

Our work highlights the utility of MSI as an integral tool of drug development in the context of the tissue distribution of novel, exploratory HIV cure strategies (e.g. latency reversal agents, nanotherapeutics, etc.). Limitations to our work are related to the MSI analyses. First, the sensitivity of the MSI analysis was particularly challenging with the spleen tissue. This may be related to the abundance of blood, which contains water, and may have innately interfered with using ice as a matrix to detect ARVs. Second, the resolution of the MSI analysis (100 uM) required down-sampling the higher resolution viral RNA images (10 uM); this inevitably results in a loss of tissue detail and granularity of the drug location, necessary components to more fully understand the relationship between drug exposure and viral persistence within the spleen at a cellular level. Third, coregistration of multiple targets to understand the overlap between these methods introduces error due to resolution differences. This would be mitigated via analyzing ion signatures of viral proteins/peptides such that only one type of analysis would need to be performed, such as IR-MALDESI, to capture all these targets. Lastly, similar to the limitations of Chapter 2, only one time point was evaluated, after 10 days of ART. Therefore, we cannot assess the dynamics between viral and ART distribution over the long-term. Future studies would

benefit from multiple time-point sampling of spleen tissues during chronic suppression to determine the dynamism of ARV distribution and the viral reservoir.

Chapter 4 introduced another computational methodology to address a limitation of the one time-point analysis of the penetration ratios from Chapter 2. Utilizing novel physiologically-based pharmacokinetic (PBPK) models, we characterized the distribution of two common ARVs: emtricitabine (FTC) and tenofovir (TFV) as well as their phosphorylated metabolites FTC triphosphate (FTCtp) and TFV diphosphate (TFVdp) in the spleens of NHPs and humans. The final models captured our observed data and the predicted:observed AUC and Cmax ratios were within the acceptance criteria (0.5-2.0) for both drugs and species. Addressing the limitation of Chapter 2, model-predicted penetration ratios between tissue and plasma $AUC_{0\text{-}24hr}$ measurements aligned well with the humans but noted discordance with the NHPs. AUC PRs for NHPs were approximately 60% lower compared to 24-hour PRs ($p < 0.001$ for both ARVs); these same values were not statistically significantly different for humans.

Sensitivity analyses suggested that ARVs are perfusion-limited in the spleen. Ideally, spleen tissue samples taken at approximately the T_{max} would validate these findings. In this analysis, we found a closer alignment of the metabolite half-lives with those of PBMCs versus RBCs.[221–223]. Since the spleen is home to an extensive mononuclear phagocyte system in the reticular connective tissue located in the red pulp[15], it is conceivable that these cells (red pulp macrophages) and other mononuclear splenocytes are responsible – alongside RBCs – for the intracellular biotransformation of the NRTIs.

This computational approach that utilized PBPK models provide a key translational resource to simulate drug penetration and exposure in a noninvasive way. This is particularly important as obtaining spleen tissue biopsies are quite costly in NHP models and prohibitively

invasive in humans. Indeed, we had only one spleen sample from humans that could be used as an observed data point for model development, indicating a major limitation of this work. Tissue databanks are a key resource to obtain spleen tissue, and archives of medical data and dosing times are often incomplete. Furthermore, patients within these databanks succumb to severe illness and have comorbidities that may alter the disposition of ARVs in plasma and spleen tissues. Our models would need to be refined based on additional data from these sources as one data point to help validate spleen tissue concentrations is not comprehensive for dosing schema across species, especially if future therapeutics rely on these ARVs.

These PBPK models, nonetheless, provide an important framework for understanding the penetration of small molecules within the spleen tissue; this can be extrapolated to other disease states also. Importantly, patterns based on physicochemical properties emerged as had been assessed in Chapters 2 and 3. We had observed that FTC, a hydrophilic ARV with a logP of -0.5, did not distribute well into the NHP spleen tissue. These properties can help make *a priori* assumptions about the tissue distribution of small molecules being actively explored in the HIV cure research space. For instance, this same property for romidepsin and panobinostat are 2.2 and 3, respectively.[233,234] From this, we may presume that the cellular permeability within the spleen tissue may be better than that seen with hydrophilic compounds. The use of PBPK models to predict exposure in the spleen tissue may be better suited for exogenous compounds that rely on clearance from the spleen, such as antibodies[108], which are also bring studied for HIV cure.[120] These computational approaches will help determine optimal combination dosing schemes to understand the exposure of these agents at the tissue level to maximize efficacy and minimize toxicity.

In this dissertation work, we had noted that quantifying ARV concentrations within tissue homogenates (Chapter 2) is only the start of holistically understanding tissue pharmacology. As mentioned, because concentrations are averaged across tissue homogenates, intratissue heterogeneity and variability cannot be assessed. We addressed this through Chapter 3, noting disparities between the methods of LC-MS/MS of tissue homogenates and MSI, particularly in the spleen lymphoid tissue. Lastly, the PBPK approach (Chapter 4) can help us predict concentrations to streamline drug development. This highlights the gap between what occurs theoretically and in reality, which is illustrated in Appendix 5.1.

Future studies to understand HIV latency are warranted and would benefit from emerging technologies alongside what has been described in this dissertation work. Spatial transcriptomics can be performed alongside methodologies herein. Spatial transcriptomics builds upon traditional RNA sequencing by preserving spatial information, and has been utilized to characterize intratumor heterogeneity of tumor subpopulations within a single histological slice.[235] This technological advance has yet to be studied within the HIV/AIDS research space and provides an additional dimension to understanding the HIV reservoir. A recent review has examined the utilization of spatial transcriptomics alongside novel single-cell sequencing within the CNS reservoir as a powerful tool to understand HIV latency phenotypes and therapeutic responses.[236] The latter argument is germane to the imaging technologies presented in this dissertation work, particularly the MSI results from IR-MALDESI.

For instance, from a tissue slice, if the phenotypic profiles of cell-associated RNA is detailed via transcriptomics, this can be colocalized with the ARV distributional patterns from IR-MALDESI. Theoretically, we could ultimately relate ARV exposure with the potential for spatial, viral evolution within tissues. Additionally, examining the specific ARVs at each

sampling location will allow us to conclude if certain combinations – or lack thereof – of ARVs yield differential viral sequencing. Gathering these data over multiple tissue slices provides useful information that would work towards creating a three-dimensional atlas of the tissue reservoir in question. Lastly, obtaining these data over time will be incredibly beneficial to understand the viral reservoir dynamics within lymphoid tissues. This combinatorial approach should be prospectively utilized in the era of experimental therapeutics for the HIV treatment and cure fields and potentially bring an end to the HIV epidemic.

Conclusion

From this dissertation work, we utilized a multifactorial approach of quantitative and computational techniques to comprehensively investigate ARV distribution and HIV persistence within the spleen lymphoid tissue in multiple, relevant species. We explored a multitude of biologically and physiologically-relevant factors that influence ARV concentrations, quantified the spatial relationship between ARVs and virus, and characterized splenic exposure of ARVs over the dosing interval. These addressed major pharmacology gaps in the literature and vastly improve our understanding of the ARV pharmacology in the spleen reservoir, and knowing the differential distribution of drugs within tissues assists in understanding risks with nonadherence. Furthermore, as experimental formulations and/or therapeutics are examined for HIV treatment and cure, tissue penetration should be considered at the sites of action germane to HIV reservoirs.

APPENDIX 2.1: DISTRIBUTION OF SPLEEN CONCENTRATIONS IN THREE SPECIES BY INFECTION STATUS

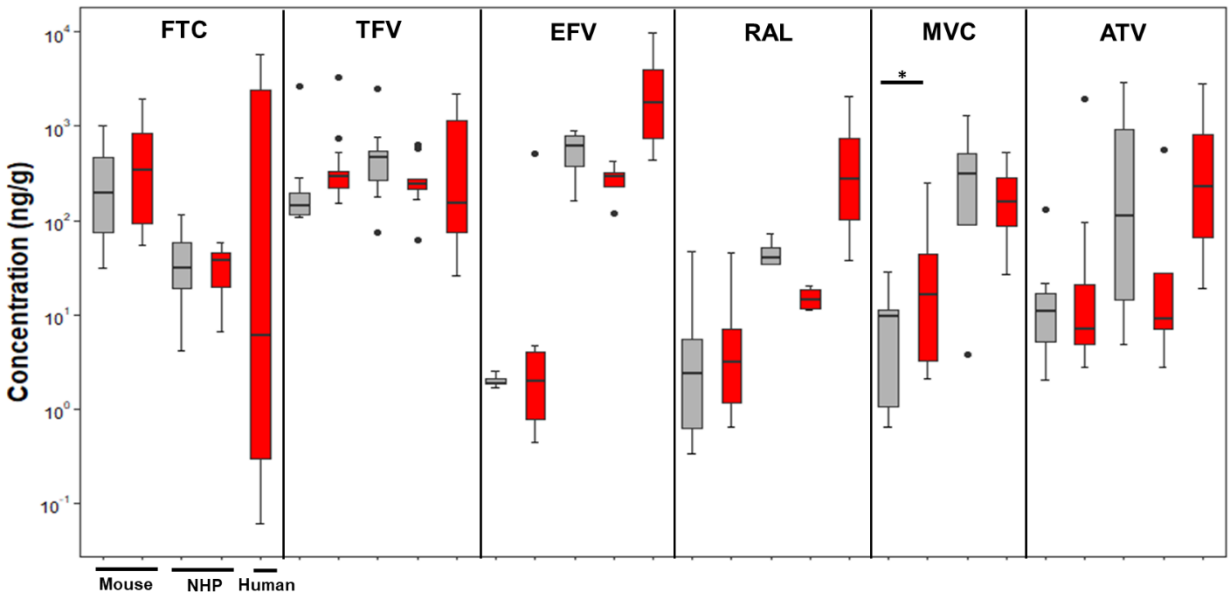

Boxplots are medians with 25th and 75th percentiles. Whiskers display the data point still within 1.5-times the interquartile range below and above the lower and upper quartile values, respectively. Uninfected is in gray, and infected is in red. *p<0.05 via Kruskal-Wallis One Way ANOVA test followed by Dunn's test with the Holm-Sidek p-value corrections for multiple comparisons. FTC, emtricitabine; TFV, tenofovir; EFV, efavirenz; RAL, raltegravir; MVC, maraviroc; ATV, atazanavir; NHP, nonhuman primate. Located: M:\DPET\CPAC General Lab\GRADUATE STUDENTS\Aaron D\Spleen\R Graphs\Drug Concentrations

APPENDIX 2.2: DISTRIBUTION OF SPLEEN CONCENTRATIONS BY SEX

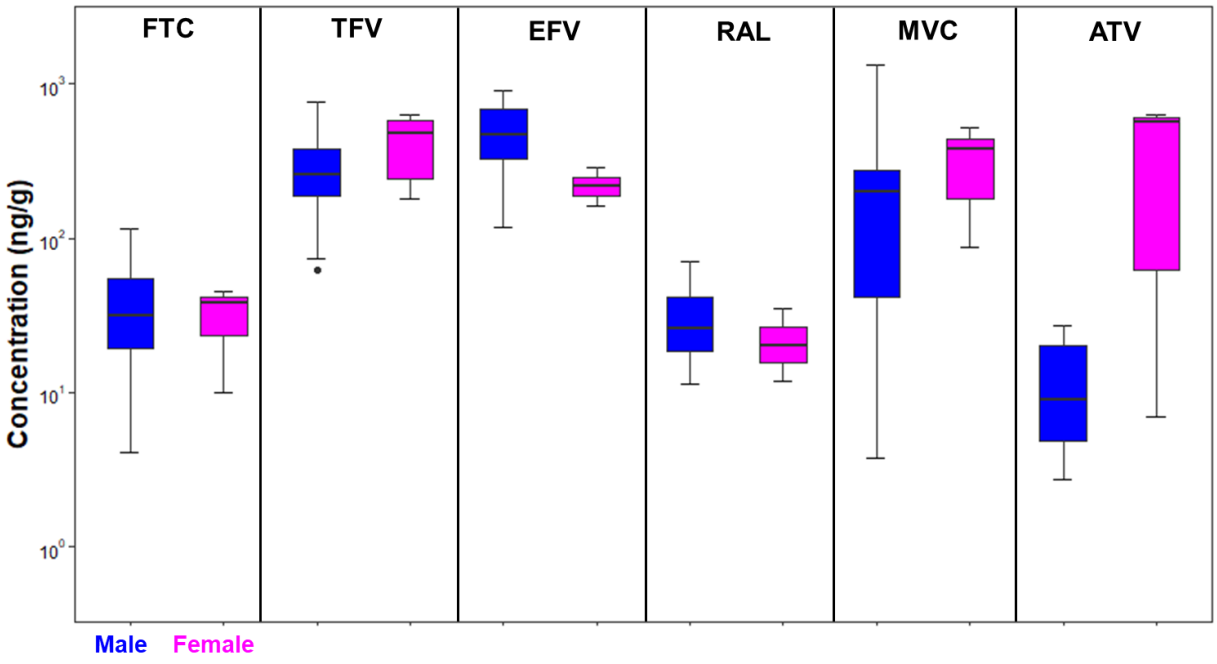

Boxplots are medians with 25th and 75th percentiles. Whiskers display the data point still within 1.5-times the interquartile range below and above the lower and upper quartile values, respectively. Males are in blue, and females are in magenta. *p<0.05 via Kruskal-Wallis One Way ANOVA test followed by Dunn's test with the Holm-Sidek p-value corrections for multiple comparisons. FTC, emtricitabine; TFV, tenofovir; EFV, efavirenz; RAL, raltegravir; MVC, maraviroc; ATV, atazanavir; NHP, nonhuman primate. Located: M:\DPET\CPAC General Lab\GRADUATE STUDENTS\Aaron D\Spleen\R Graphs\Drug Concentrations

APPENDIX 2.3: DISTRIBUTION OF METABOLITE-TO-ENDOGENOUS NUCLEOTIDE RATIOS FOR THE TWO ACTIVE METABOLITES BY SEX

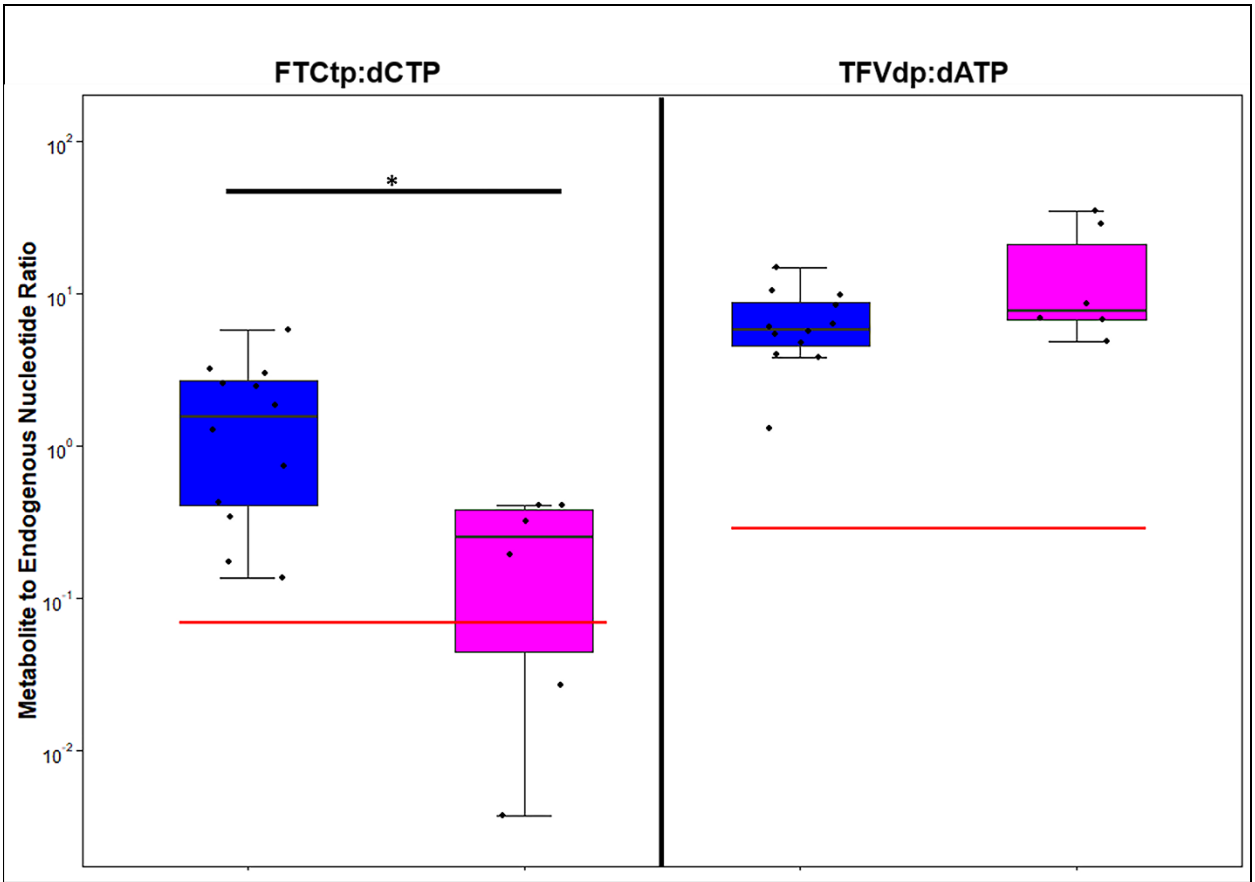

Boxplots are medians with 25th and 75th percentiles. Whiskers display the data point still within 1.5-times the interquartile range below and above the lower and upper quartile values, respectively. Horizontal lines indicate the 90% effective ratios from Cottrell et al.[157] Males are in blue, and females are in magenta. *p<0.05 via Wilcoxon Rank Sum Test. FTCtp, emtricitabine triphosphate; dCTP, deoxycytidine triphosphate; TFVdp, tenofovir diphosphate; dATP, deoxyadenosine triphosphate. Located: M:\DPET\CPAC General Lab\GRADUATE STUDENTS\Aaron D\Spleen\R Graphs\Drug Concentrations

APPENDIX 2.4: DISTRUBTION OF FREE FRACTIONS BY INFECTION STATUS

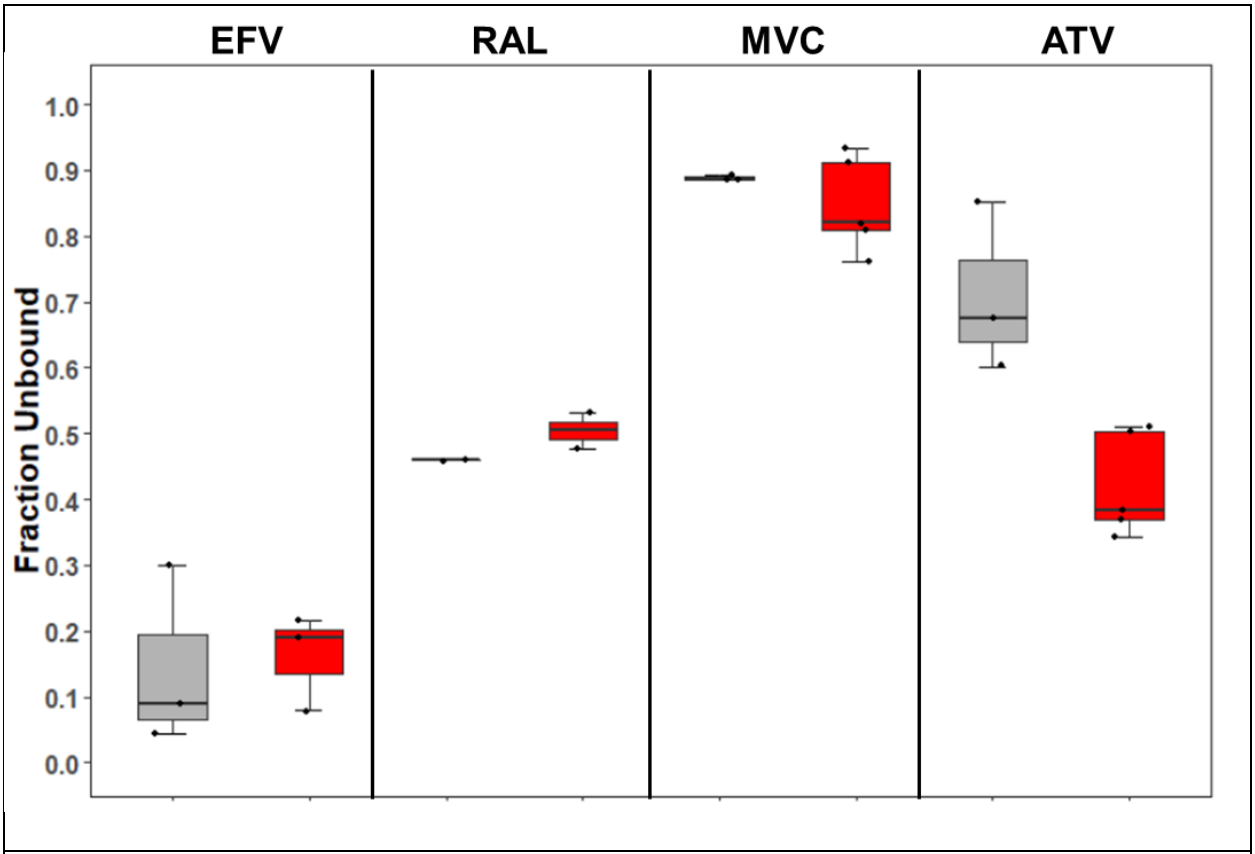

Boxplots are medians with 25th and 75th percentiles. Whiskers display the data point still within 1.5-times the interquartile range below and above the lower and upper quartile values, respectively. Uninfected NHPs are in gray, and infected NHPs are in red. *p<0.05 via Wilcoxon Rank Sum Test. EFV, efavirenz; RAL, raltegravir; MVC, maraviroc; ATV, atazanavir; NHP, nonhuman primate. Located: M:\DPET\CPAC General Lab\GRADUATE STUDENTS\Aaron D\Spleen\R Graphs\Drug Concentrations

APPENDIX 2.5: DISTRUBTION OF FREE FRACTIONS UNBOUND BY SEX

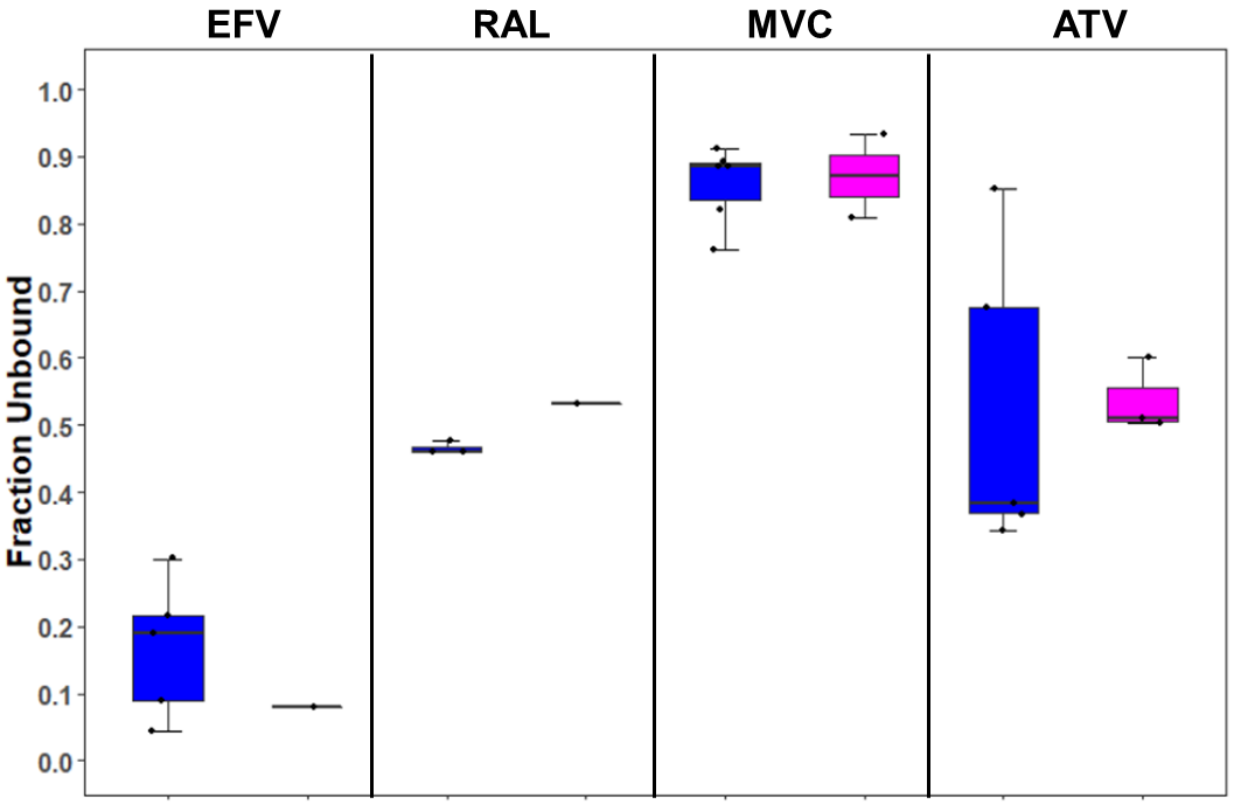

Boxplots are medians with 25th and 75th percentiles. Whiskers display the data point still within 1.5-times the interquartile range below and above the lower and upper quartile values, respectively. Males are in blue, and females are in magenta. *p<0.05 via Wilcoxon Rank Sum Test. EFV, efavirenz; RAL, raltegravir; MVC, maraviroc; ATV, atazanavir; NHP, nonhuman primate. Located: M:\DPET\CPAC General Lab\GRADUATE STUDENTS\Aaron D\Spleen\R Graphs\Drug Concentrations

APPENDIX 2.6: DISTRUBTION OF UNBOUND PENETRATION RATIOS BY INFECTION STATUS

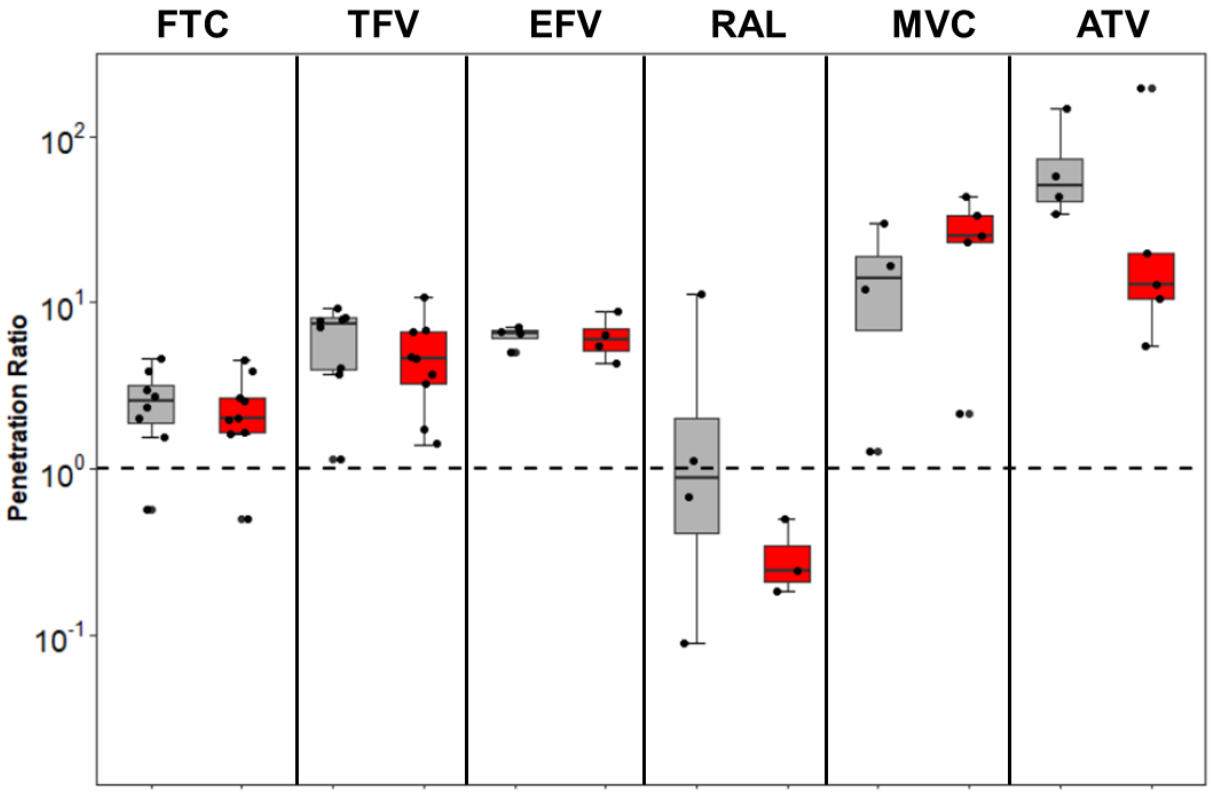

Boxplots are medians with 25th and 75th percentiles. Whiskers display the data point still within 1.5-times the interquartile range below and above the lower and upper quartile values, respectively. Uninfected NHPs are in gray, and infected NHPs are in red. *p<0.05 via Wilcoxon Rank Sum Test. FTC, emtricitabine; TFV, tenofovir; EFV, efavirenz; RAL, raltegravir; MVC, maraviroc; ATV, atazanavir; NHP, nonhuman primate. Located: M:\DPET\CPAC General Lab\GRADUATE STUDENTS\Aaron D\Spleen\R Graphs\Drug Concentrations

APPENDIX 2.7: DISTRUBTION OF UNBOUND PENETRATION RATIOS BY SEX

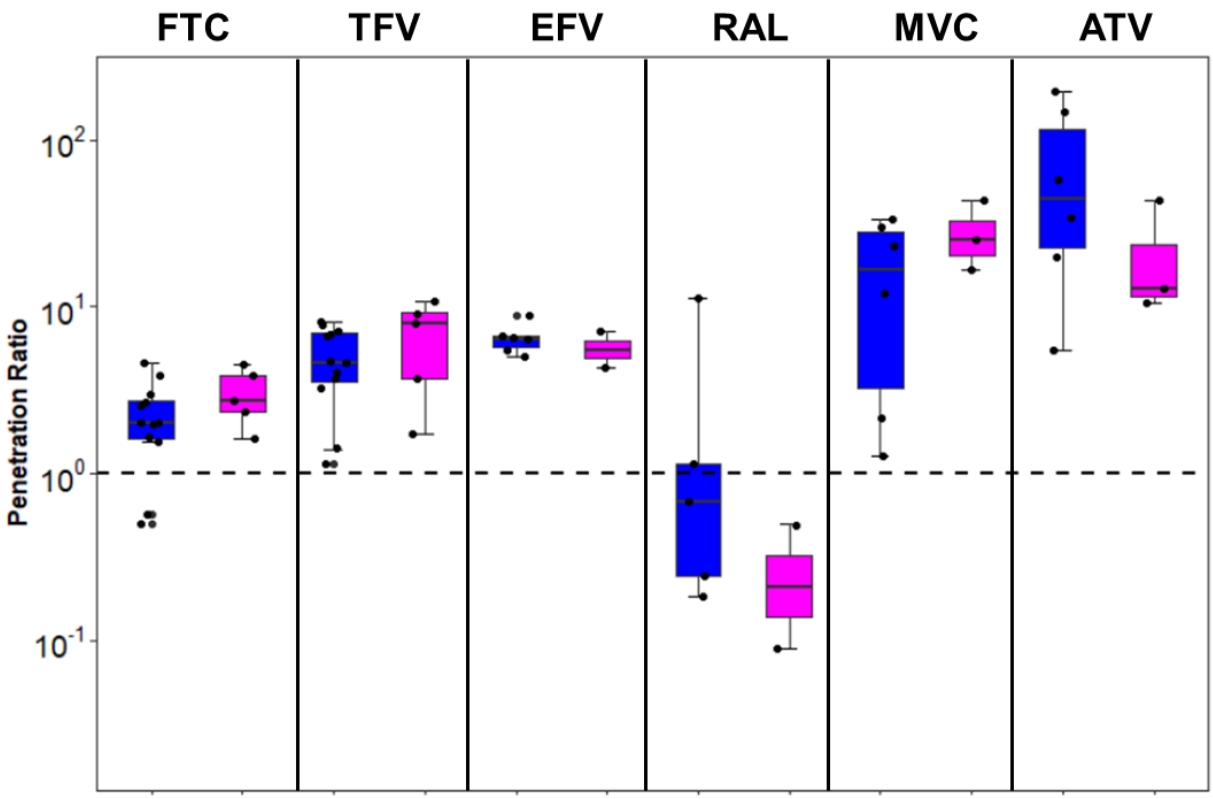

Boxplots are medians with 25th and 75th percentiles. Whiskers display the data point still within 1.5-times the interquartile range below and above the lower and upper quartile values, respectively. Males are in blue, and females are in magenta. *p<0.05 via Wilcoxon Rank Sum Test. FTC, emtricitabine; TFV, tenofovir; EFV, efavirenz; RAL, raltegravir; MVC, maraviroc; ATV, atazanavir; NHP, nonhuman primate. Located: M:\DPET\CPAC General Lab\GRADUATE STUDENTS\Aaron D\Spleen\R Graphs\Drug Concentrations

APPENDIX 2.8: DISTRIBUTION OF TRANSPORTER CONCENTRATIONS IN NONHUMAN PRIMATES (NHPS) BY INFECTION STATUS

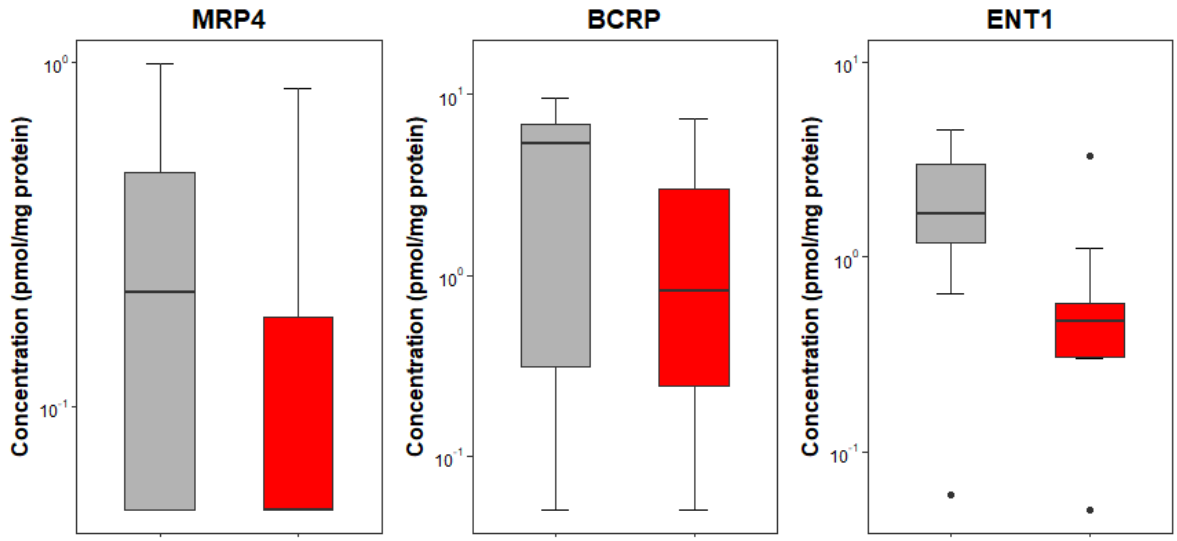

Boxplots are medians with 25th and 75th percentiles. Whiskers display the data point still within 1.5-times the interquartile range below and above the lower and upper quartile values, respectively. Uninfected NHPs are in gray, and infected NHPs are in red. *p<0.05 via Wilcoxon Rank Sum Test. Located: M:\DPET\CPAC General Lab\GRADUATE STUDENTS\Aaron D\Spleen\R Graphs\Drug Concentrations

APPENDIX 2.9: DISTRIBUTION OF TRANSPORTER CONCENTRATIONS IN NONHUMAN PRIMATES (NHPS) BY SEX

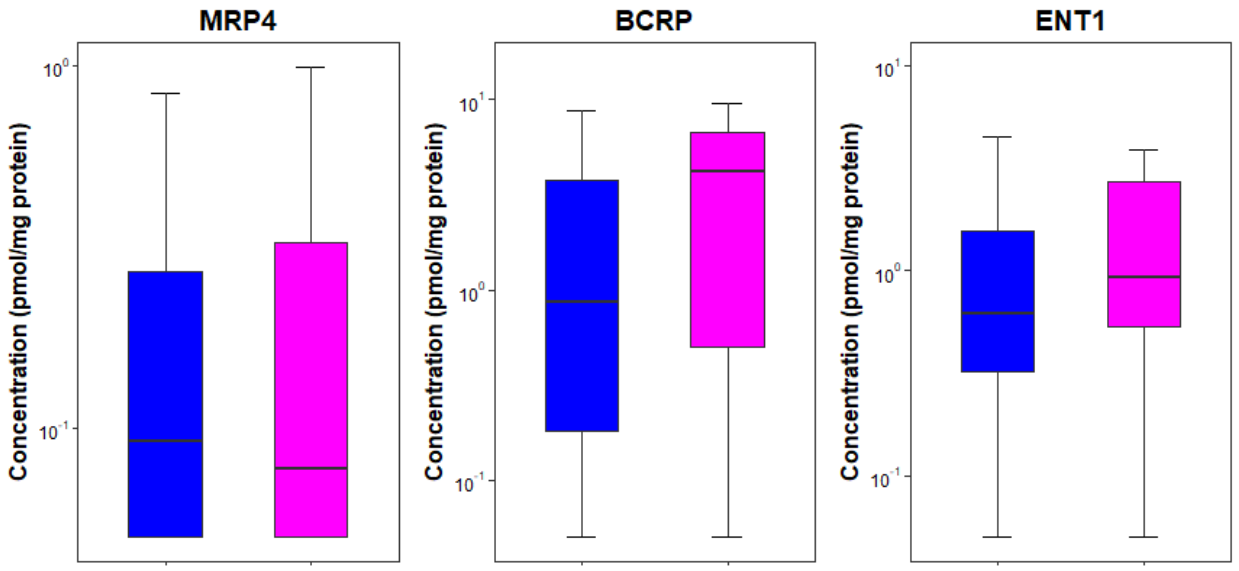

Boxplots are medians with 25th and 75th percentiles. Whiskers display the data point still within 1.5-times the interquartile range below and above the lower and upper quartile values, respectively. Males are in blue, and females are in magenta. *p<0.05 via Wilcoxon Rank Sum Test. Located: M:\DPET\CPAC General Lab\GRADUATE STUDENTS\Aaron D\Spleen\R Graphs\Drug Concentrations

APPENDIX 2.10: TRANSPORTER CORRELATIONS WITH ARV CONCENTRATIONS

ARV	BCRP	MRP4	ENT1
FTC			-0.2
TFV	-0.3	-0.1	-0.4
EFV	-0.1		
Unbound EFV	-0.1		
RAL	0.6		
Unbound RAL	0.6		
MVC			
Unbound MVC			
ATV			
Unbound ATV			

Correlations calculated by Spearman Rho Correlation Coefficient.
Abbreviations: ARV, antiretroviral; FTC, emtricitabine; TFV, tenofovir; EFV, efavirenz; RAL, raltegravir; MVC, maraviroc; ATV, atazanavir.
Located: M:\DPET\CPAC General Lab\GRADUATE STUDENTS\Aaron D\Spleen\R Graphs\Drug Concentrations

APPENDIX 3.1: VIRAL LOAD MEASUREMENTS FOR RT-SHIV+ NONHUMAN PRIMATES

NHP	Sex	Regimen	Day of peak pVL	Peak pVL (copies/mL)	Day of ART start	ART day 0 pVL (copies/mL)	pVL at necropsy (copies/mL)	Spleen VL at necropsy (copies/10^6 cells)
40422*	F	FTER	21	1,200,000	42	130,000	3,800	797,938
40437	M	FTER	14	6,900,000	42	1,100,000	1,900	3,693,968
42226	M	FTER	21	250,000	42	28,000	7.5	1,281
42707¶	F	FTER	14	16,000,000	42	1,900,100	340	144,633
42971	M	FTER	21	1,500,000	42	97,000	380	396,448
41380	M	FTMA	14	60,000,000	42	3,000,000	68,000	5,417,501
42350	F	FTMA	14	13,000,000	42	150,000	2,200	913,280
42706	F	FTMA	14	17,000,000	42	2,400,000	30,000	335,240
42827	M	FTMA	14	9,800,000	42	130,000	1,100	2,138,860
42966	M	FTMA	14	11,000,000	42	4,400,000	19,000	1,891,979

Asterisk (*) indicates NHP 40422, which was excluded from analysis due to the development of hepatic failure. Paragraph indent symbol (¶) indicates NHP 42707, for which representative images were provided in the manuscript text. Abbreviations: RT-SHIV, reverse transcriptase simian-human immunodeficiency virus. NHP, nonhuman primate; FTER, regimen consisting of emtricitabine/tenofovir/efavirenz/raltegravir; FTMA, regimen consisting of emtricitabine/tenofovir/maraviroc/atazanavir; pVL, plasma viral load; ART, antiretroviral therapy. These were the same NHPs as reported in previous publications.[80,197]

APPENDIX 3.2: FIBROSIS ANTIBODIES INFORMATION

Antibody	Catalogue#/Vendor	Concentration	Primary incubation time	Protocol
Collagen I	C2456/Sigma	1:100	2 hrs	ER2(20); Leica Novolink Post Primary and Polymer
Collagen III	HPA007583/Sigma	1:25	1 hr	ER2(20); Leica Novolink Post Primary and Polymer
Fibrinogen	HPA001900/Sigma	1:1500	2 hrs	ER2(20); Leica Novolink Post Primary and Polymer

APPENDIX 3.3: DYNAMIC RANGES OF ARV DISTRIBUTIONS WITH SPLEEN TISSUE

ARV	N	Dynamic Range
FTC	17	7.4 (2.1-15.8)
TFV	17	5.8 (0.5-11.7)
EFV	8	6.1 (1.2-179)
RAL	8	5.4 (4.1-9.2)
MVC	9	57.5 (0.8-183)
ATV	9	7.9 (5.9-20.6)

Data are median (range). Dynamic Range = 10 x $\log_{10}$(maximum/minimum intensities).[92] Abbreviations: ARV, antiretroviral; FTC, emtricitabine; TFV, tenofovir; EFV, efavirenz; RAL, raltegravir; MVC, maraviroc; ATV, atazanavir.

APPENDIX 3.4: ADDITIONAL INTENSITY-SCALED MSI IMAGE #1

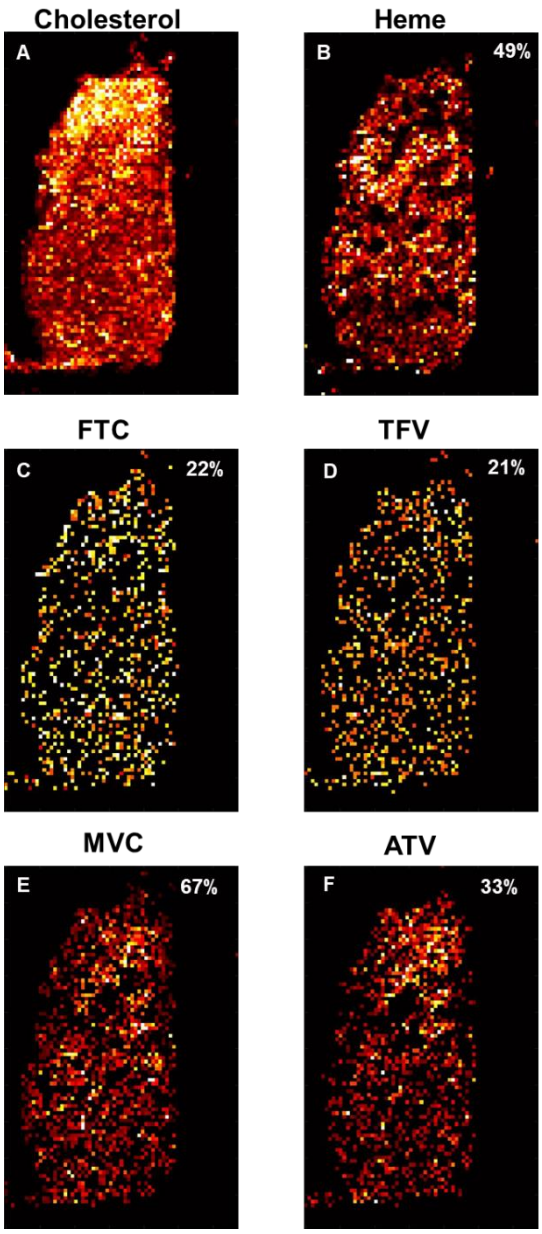

Intensity-scaled MSI images of the distribution of cholesterol (A), heme (B), FTC (C), TFV (D), MVC (E), and ATV (F) in an RT-SHIV- NHP. Percentages in the top-right corner indicate the MSI area covered by each target. Brighter colors (white and yellow) represent higher MSI signal intensities whereas darker colors (black and red) represent the converse. Abbreviations: FTC, emtricitabine; TFV, tenofovir; MVC, maraviroc; ATV, atazanavir; MSI, mass spectrometry imaging; RT-SHIV, reverse trascriptase simian-human immunodeficiency virus; NHP, nonhuman primate. Located M:\DPET\CPAC General Lab\GRADUATE STUDENTS\Aaron D\Spleen\MALDESI

APPENDIX 3.5: ADDITIONAL INTENSITY-SCALED MSI IMAGE #2

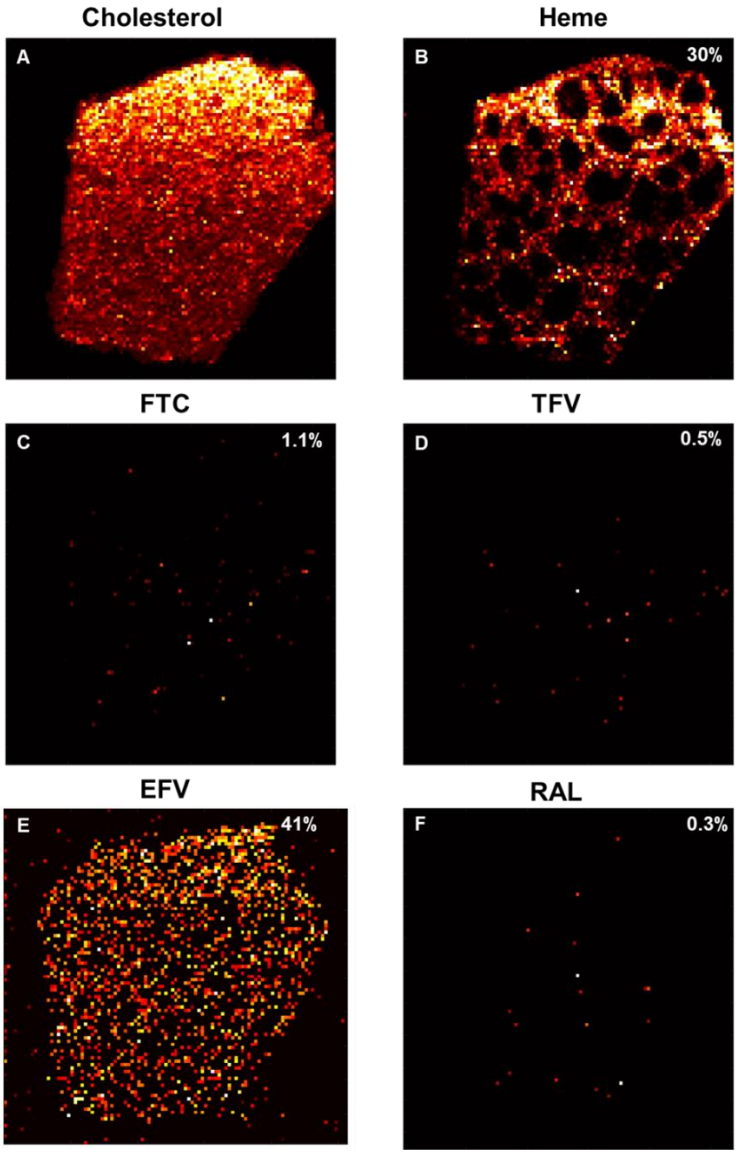

Intensity-scaled MSI images of the distribution of cholesterol (A), heme (B), FTC (C), TFV (D), EFV (E), and RAL (F) in an RT-SHIV+ NHP. Percentages in the top-right corner indicate the MSI area covered by each target. Brighter colors (white and yellow) represent higher MSI signal intensities whereas darker colors (black and red) represent the converse. Abbreviations: FTC, emtricitabine; TFV, tenofovir; MVC, maraviroc; ATV, atazanavir; MSI, mass spectrometry imaging; RT-SHIV, reverse trascriptase simian-human immunodeficiency virus; NHP, nonhuman primate. Located M:\DPET\CPAC General Lab\GRADUATE STUDENTS\Aaron D\Spleen\MALDESI

APPENDIX 3.6: ADDITIONAL INTENSITY-SCALED MSI IMAGE #3

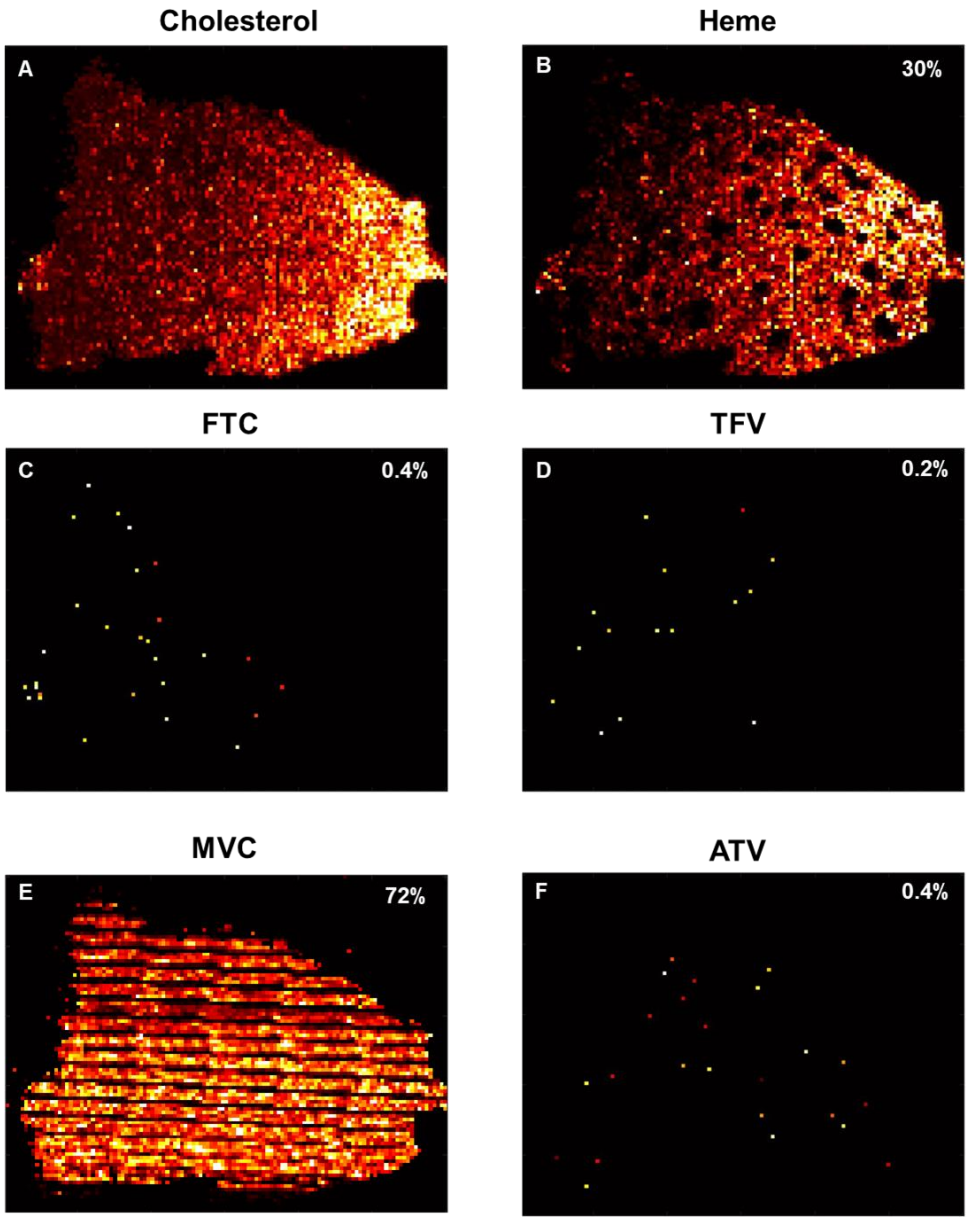

Intensity-scaled MSI images of the distribution of cholesterol (A), heme (B), FTC (C), TFV (D), MVC (E), and ATV (F) in an RT-SHIV- NHP. Percentages in the top-right corner indicate the MSI area covered by each target. Brighter colors (white and yellow) represent higher MSI signal intensities whereas darker colors (black and red) represent the converse. Abbreviations: FTC, emtricitabine; TFV, tenofovir; MVC, maraviroc; ATV, atazanavir; MSI, mass spectrometry imaging; RT-SHIV, reverse trascriptase simian-human immunodeficiency virus; NHP, nonhuman primate. Located M:\DPET\CPAC General Lab\GRADUATE STUDENTS\Aaron D\Spleen\MALDESI

APPENDIX 3.7: ADDITIONAL INTENSITY-SCALED MSI IMAGE #4

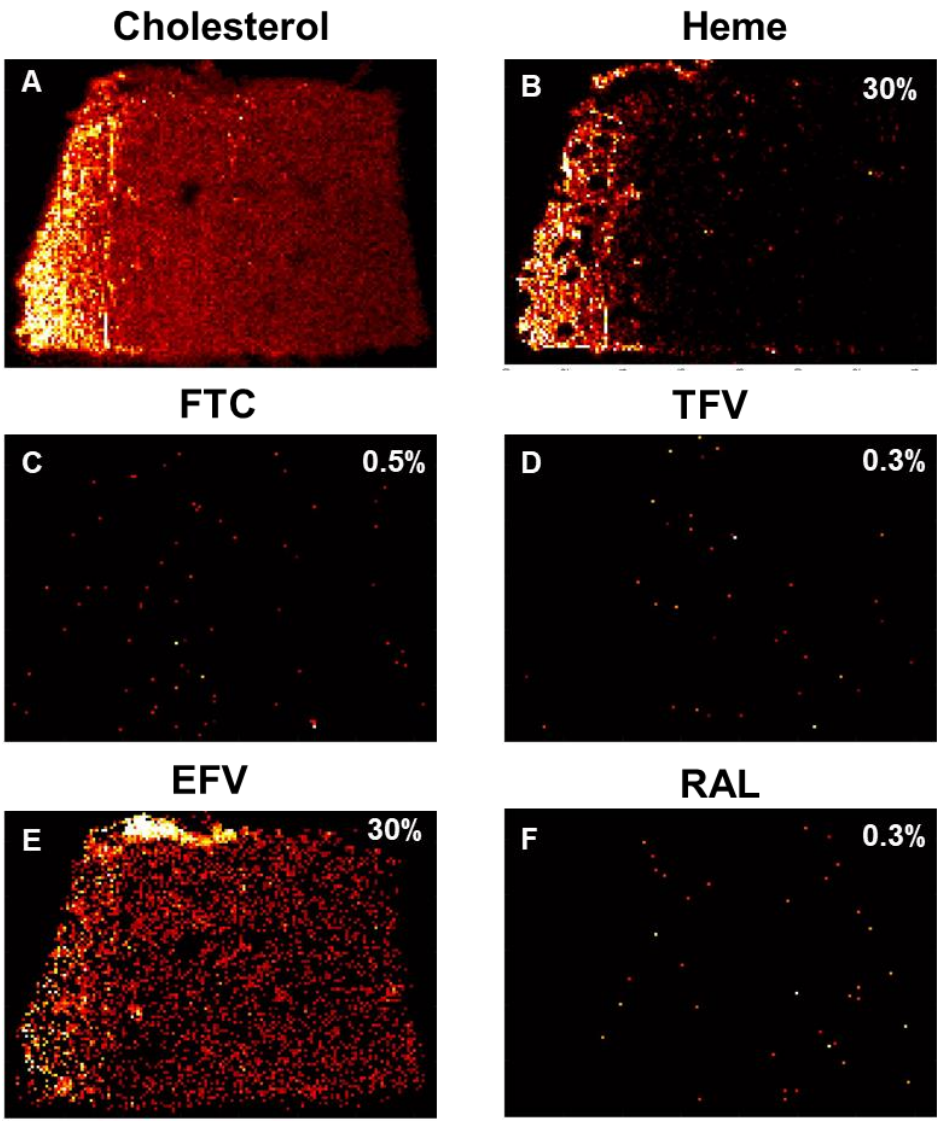

Intensity-scaled MSI images of the distribution of cholesterol (A), heme (B), FTC (C), TFV (D), EFV (E), and RAL (F) in an RT-SHIV- NHP. Percentages in the top-right corner indicate the MSI area covered by each target. Brighter colors (white and yellow) represent higher MSI signal intensities whereas darker colors (black and red) represent the converse. Abbreviations: FTC, emtricitabine; TFV, tenofovir; MVC, maraviroc; ATV, atazanavir; MSI, mass spectrometry imaging; RT-SHIV, reverse trascriptase simian-human immunodeficiency virus; NHP, nonhuman primate. Located M:\DPET\CPAC General Lab\GRADUATE STUDENTS\Aaron D\Spleen\MALDESI

APPENDIX 3.8: ADDITIONAL INTENSITY-SCALED MSI IMAGE #5

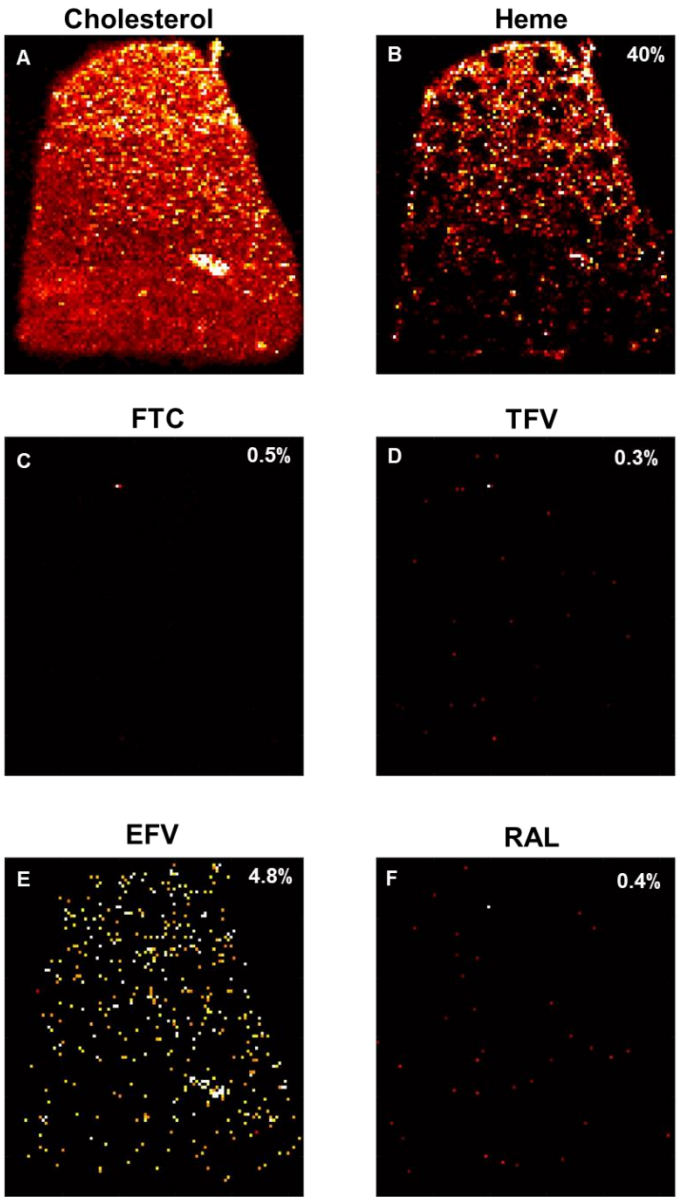

Intensity-scaled MSI images of the distribution of cholesterol (A), heme (B), FTC (C), TFV (D), EFV (E), and RAL (F) in an RT-SHIV- NHP. Percentages in the top-right corner indicate the MSI area covered by each target. Brighter colors (white and yellow) represent higher MSI signal intensities whereas darker colors (black and red) represent the converse. Abbreviations: FTC, emtricitabine; TFV, tenofovir; MVC, maraviroc; ATV, atazanavir; MSI, mass spectrometry imaging; RT-SHIV, reverse trascriptase simian-human immunodeficiency virus; NHP, nonhuman primate. Located M:\DPET\CPAC General Lab\GRADUATE STUDENTS\Aaron D\Spleen\MALDESI

APPENDIX 3.9: ADDITIONAL INTENSITY-SCALED MSI IMAGE #6

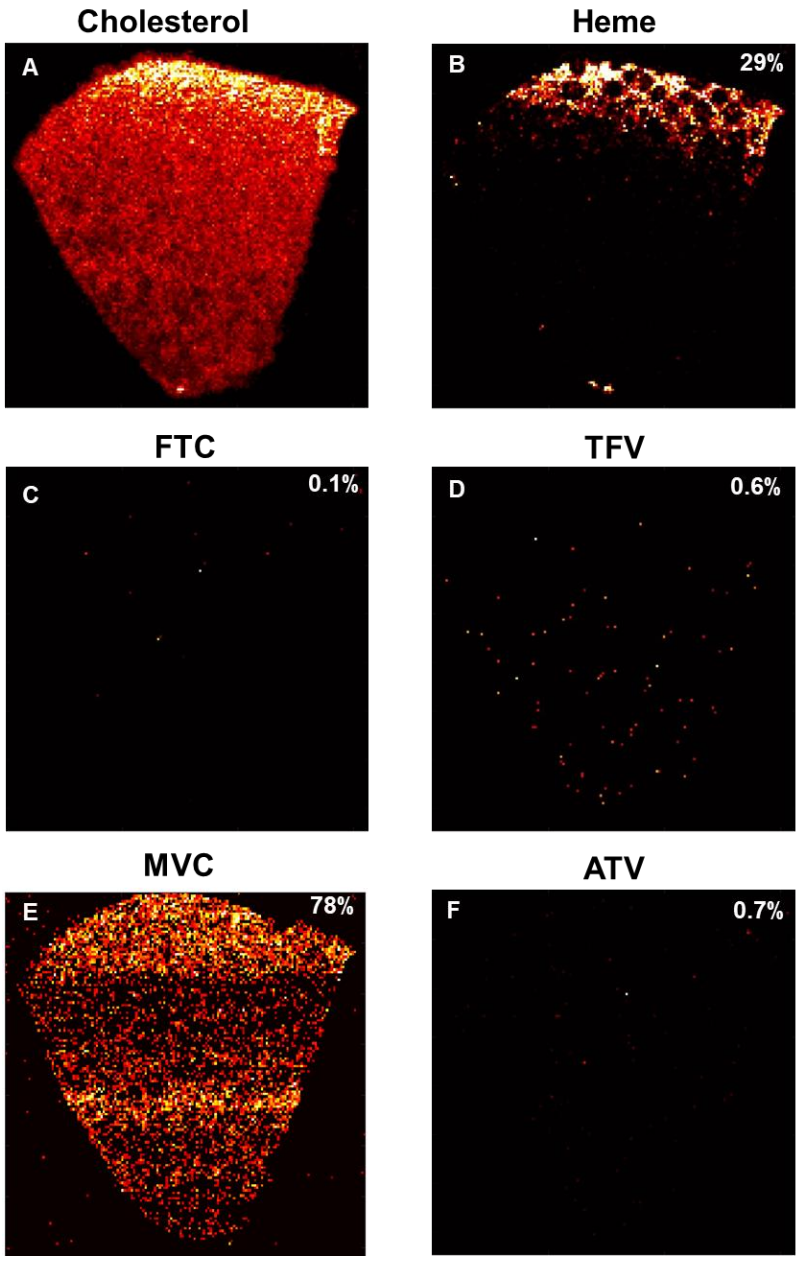

Intensity-scaled MSI images of the distribution of cholesterol (A), heme (B), FTC (C), TFV (D), MVC (E), and ATV (F) in an RT-SHIV+ NHP. Percentages in the top-right corner indicate the MSI area covered by each target. Brighter colors (white and yellow) represent higher MSI signal intensities whereas darker colors (black and red) represent the converse. Abbreviations: FTC, emtricitabine; TFV, tenofovir; MVC, maraviroc; ATV, atazanavir; MSI, mass spectrometry imaging; RT-SHIV, reverse trascriptase simian-human immunodeficiency virus; NHP, nonhuman primate. Located M:\DPET\CPAC General Lab\GRADUATE STUDENTS\Aaron D\Spleen\MALDESI

APPENDIX 3.10: ADDITIONAL INTENSITY-SCALED MSI IMAGE #7

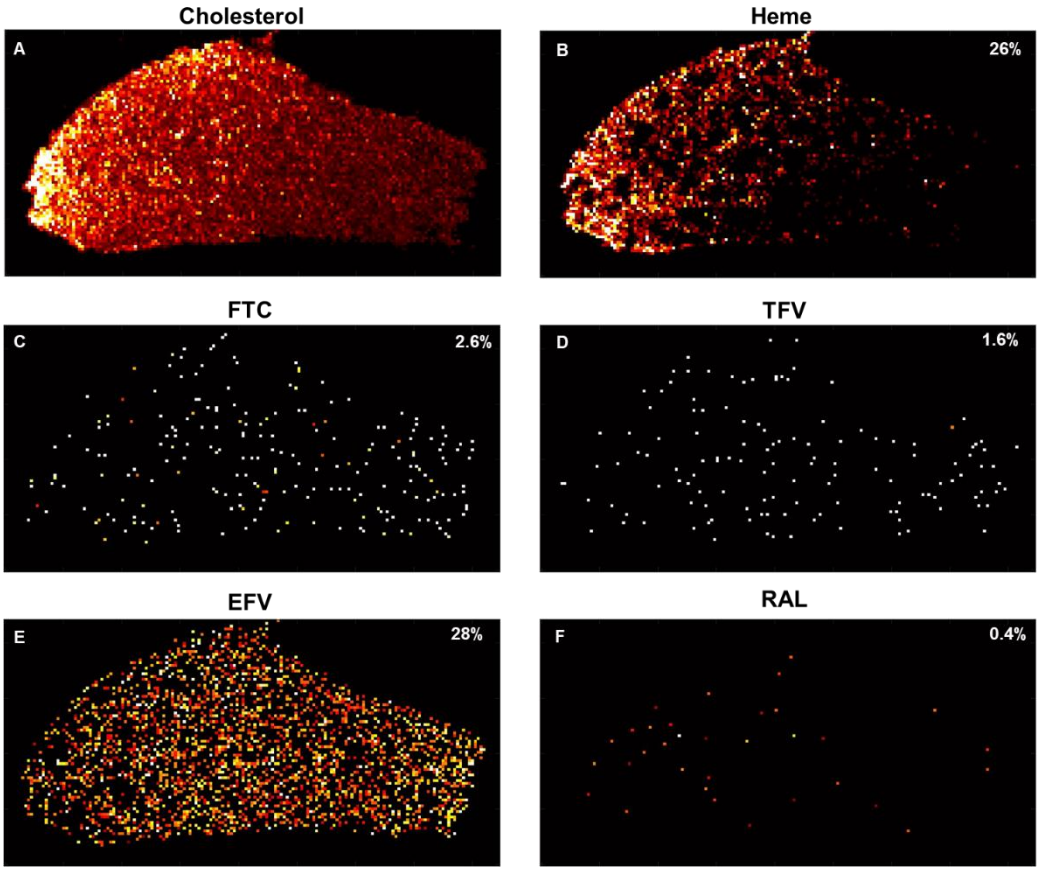

Intensity-scaled MSI images of the distribution of cholesterol (A), heme (B), FTC (C), TFV (D), EFV (E), and RAL (F) in an RT-SHIV- NHP. Percentages in the top-right corner indicate the MSI area covered by each target. Brighter colors (white and yellow) represent higher MSI signal intensities whereas darker colors (black and red) represent the converse. Abbreviations: FTC, emtricitabine; TFV, tenofovir; MVC, maraviroc; ATV, atazanavir; MSI, mass spectrometry imaging; RT-SHIV, reverse trascriptase simian-human immunodeficiency virus; NHP, nonhuman primate. Located M:\DPET\CPAC General Lab\GRADUATE STUDENTS\Aaron D\Spleen\MALDESI

APPENDIX 3.11: ADDITIONAL INTENSITY-SCALED MSI IMAGE #8

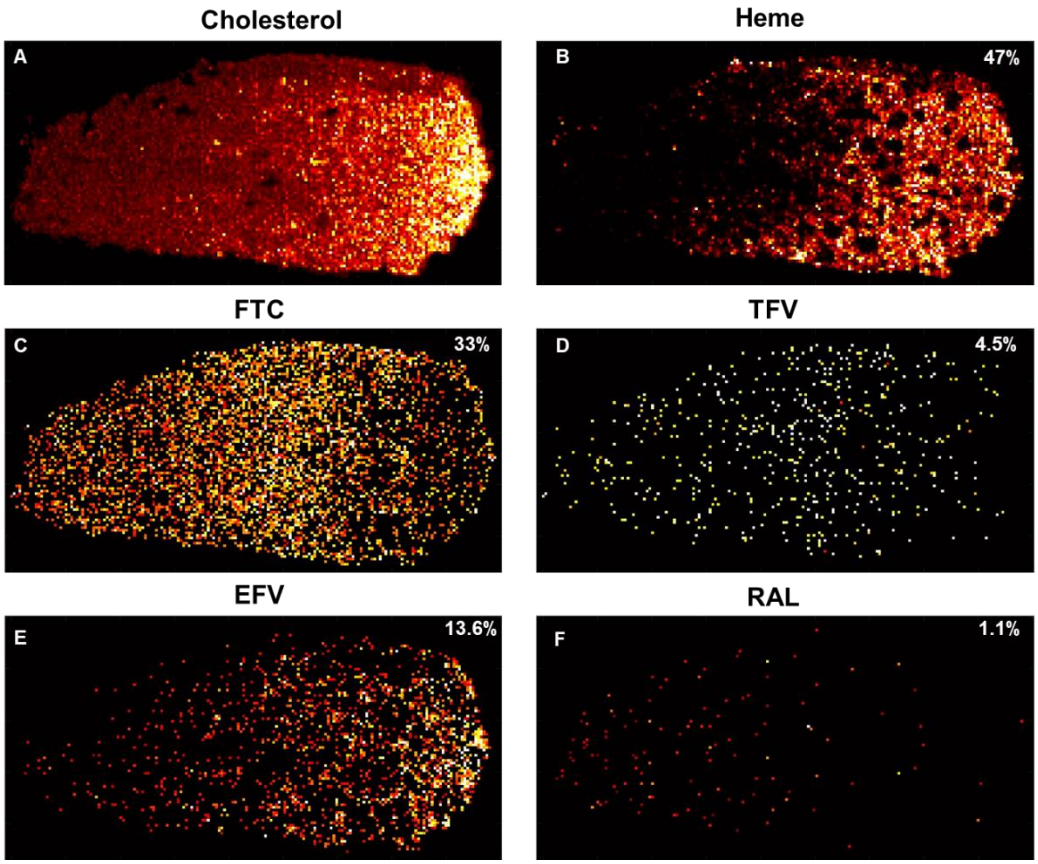

Intensity-scaled MSI images of the distribution of cholesterol (A), heme (B), FTC (C), TFV (D), EFV (E), and RAL (F) in an RT-SHIV- NHP. Percentages in the top-right corner indicate the MSI area covered by each target. Brighter colors (white and yellow) represent higher MSI signal intensities whereas darker colors (black and red) represent the converse. Abbreviations: FTC, emtricitabine; TFV, tenofovir; MVC, maraviroc; ATV, atazanavir; MSI, mass spectrometry imaging; RT-SHIV, reverse trascriptase simian-human immunodeficiency virus; NHP, nonhuman primate. Located M:\DPET\CPAC General Lab\GRADUATE STUDENTS\Aaron D\Spleen\MALDESI

APPENDIX 3.12: ADDITIONAL INTENSITY-SCALED MSI IMAGE #9

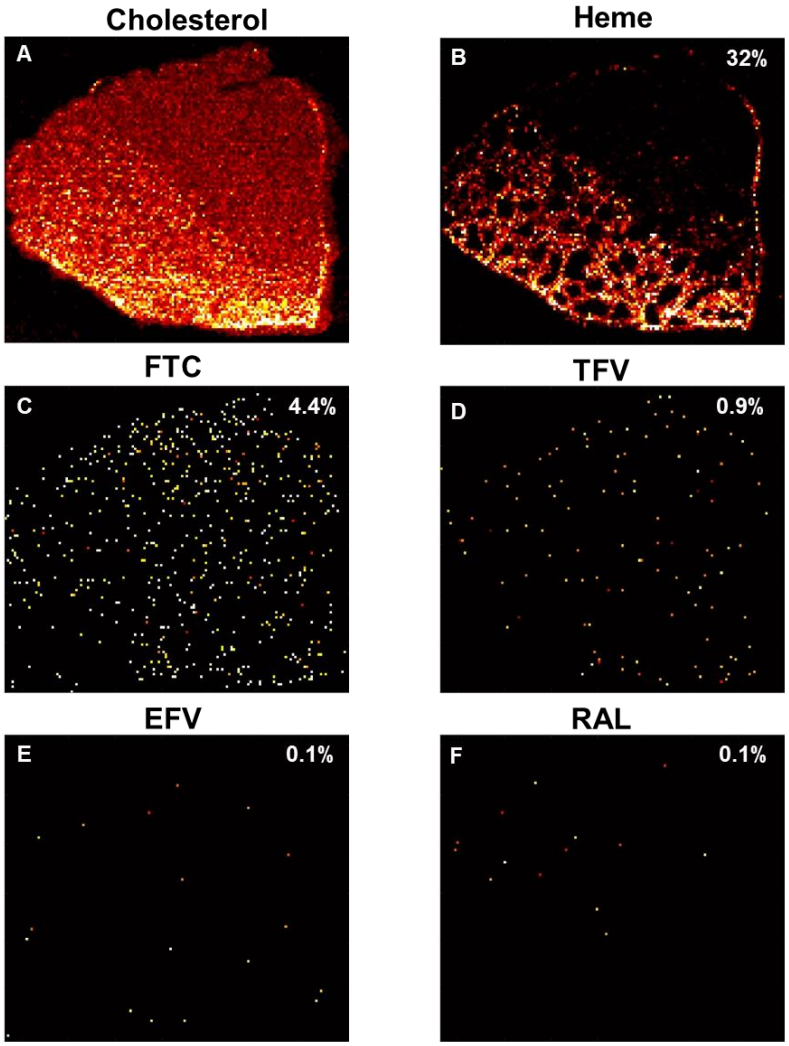

Intensity-scaled MSI images of the distribution of cholesterol (A), heme (B), FTC (C), TFV (D), EFV (E), and RAL (F) in an RT-SHIV+ NHP. Percentages in the top-right corner indicate the MSI area covered by each target. Brighter colors (white and yellow) represent higher MSI signal intensities whereas darker colors (black and red) represent the converse. Abbreviations: FTC, emtricitabine; TFV, tenofovir; MVC, maraviroc; ATV, atazanavir; MSI, mass spectrometry imaging; RT-SHIV, reverse trascriptase simian-human immunodeficiency virus; NHP, nonhuman primate. Located M:\DPET\CPAC General Lab\GRADUATE STUDENTS\Aaron D\Spleen\MALDESI

APPENDIX 3.13: ADDITIONAL INTENSITY-SCALED MSI IMAGE #10

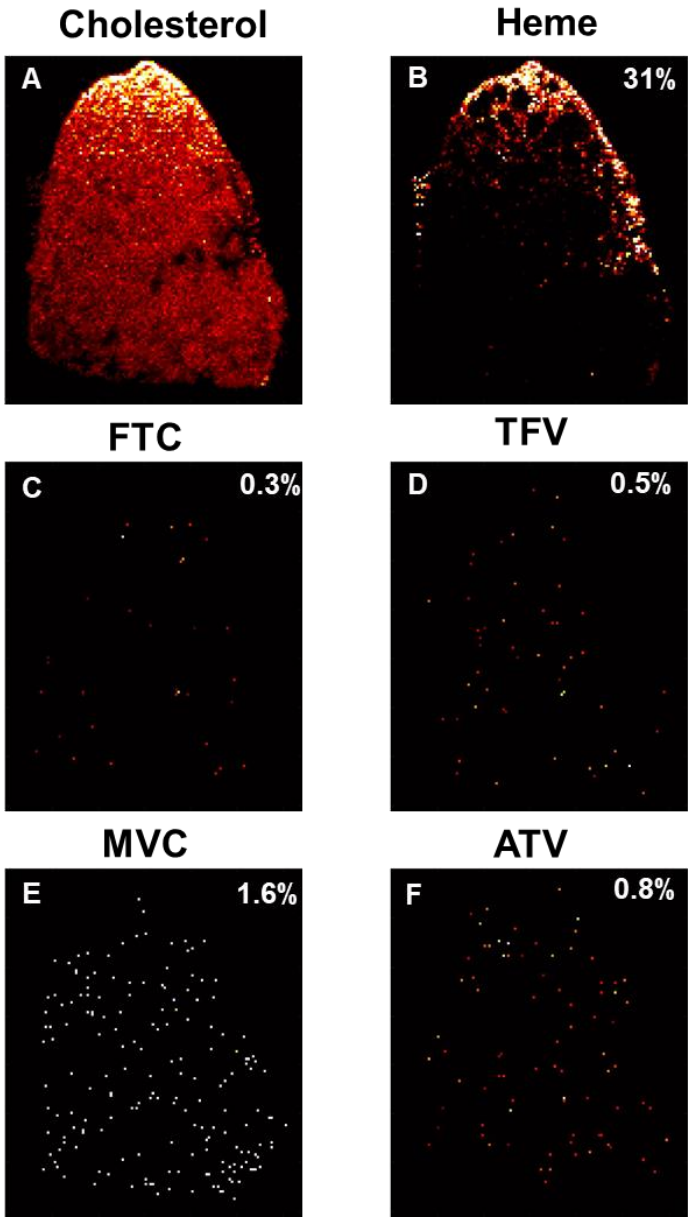

Intensity-scaled MSI images of the distribution of cholesterol (A), heme (B), FTC (C), TFV (D), MVC (E), and ATV (F) in an RT-SHIV+ NHP. Percentages in the top-right corner indicate the MSI area covered by each target. Brighter colors (white and yellow) represent higher MSI signal intensities whereas darker colors (black and red) represent the converse. Abbreviations: FTC, emtricitabine; TFV, tenofovir; MVC, maraviroc; ATV, atazanavir; MSI, mass spectrometry imaging; RT-SHIV, reverse trascriptase simian-human immunodeficiency virus; NHP, nonhuman primate. Located M:\DPET\CPAC General Lab\GRADUATE STUDENTS\Aaron D\Spleen\MALDESI

APPENDIX 3.14: ADDITIONAL INTENSITY-SCALED MSI IMAGE #11

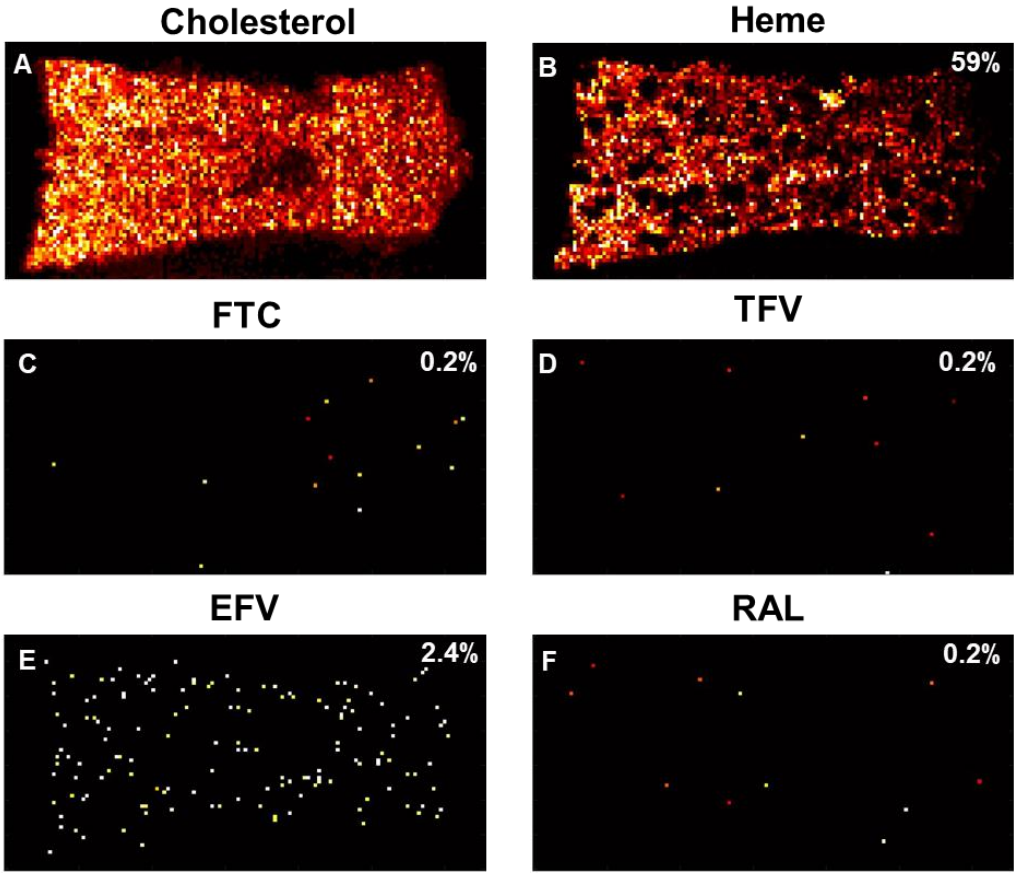

Intensity-scaled MSI images of the distribution of cholesterol (A), heme (B), FTC (C), TFV (D), EFV (E), and RAL (F) in an RT-SHIV- NHP. Percentages in the top-right corner indicate the MSI area covered by each target. Brighter colors (white and yellow) represent higher MSI signal intensities whereas darker colors (black and red) represent the converse. Abbreviations: FTC, emtricitabine; TFV, tenofovir; MVC, maraviroc; ATV, atazanavir; MSI, mass spectrometry imaging; RT-SHIV, reverse trascriptase simian-human immunodeficiency virus; NHP, nonhuman primate. Located M:\DPET\CPAC General Lab\GRADUATE STUDENTS\Aaron D\Spleen\MALDESI

APPENDIX 3.15: ADDITIONAL INTENSITY-SCALED MSI IMAGE #12

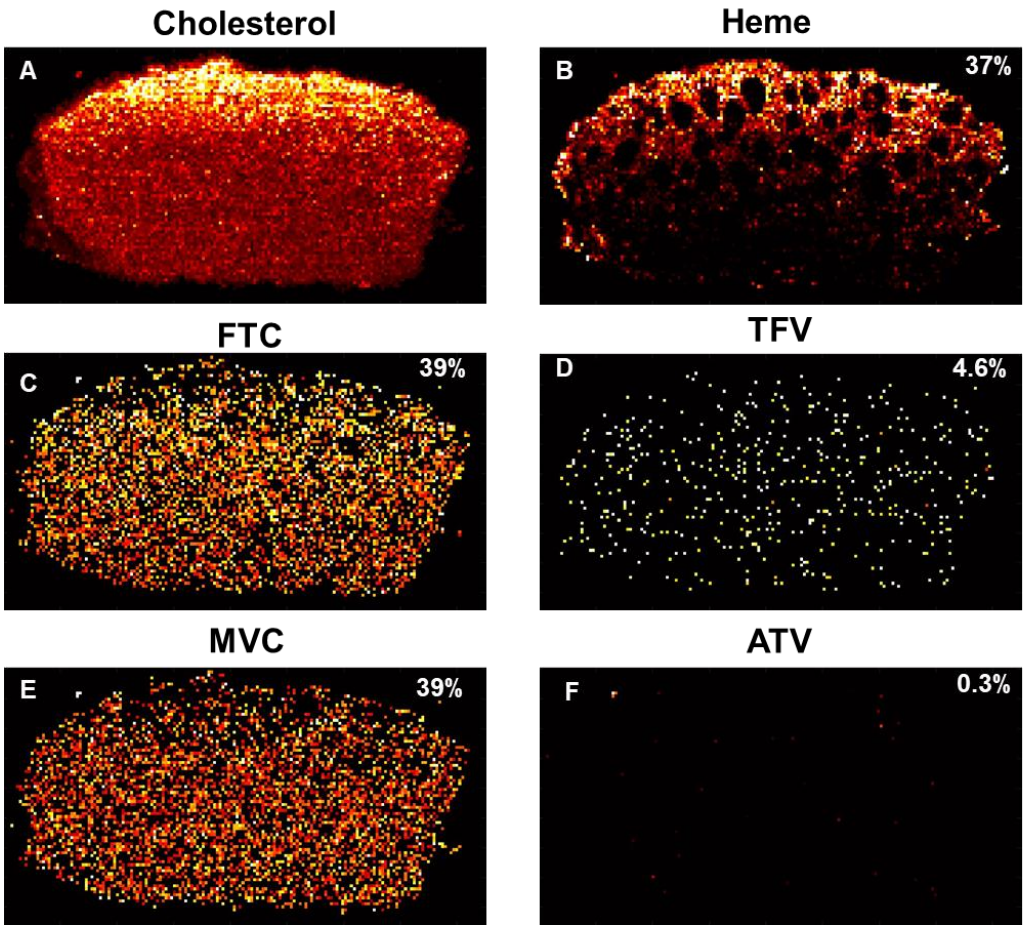

Intensity-scaled MSI images of the distribution of cholesterol (A), heme (B), FTC (C), TFV (D), MVC (E), and ATV (F) in an RT-SHIV- NHP. Percentages in the top-right corner indicate the MSI area covered by each target. Brighter colors (white and yellow) represent higher MSI signal intensities whereas darker colors (black and red) represent the converse. Abbreviations: FTC, emtricitabine; TFV, tenofovir; MVC, maraviroc; ATV, atazanavir; MSI, mass spectrometry imaging; RT-SHIV, reverse trascriptase simian-human immunodeficiency virus; NHP, nonhuman primate. Located M:\DPET\CPAC General Lab\GRADUATE STUDENTS\Aaron D\Spleen\MALDESI

APPENDIX 3.16: ADDITIONAL INTENSITY-SCALED MSI IMAGE #13

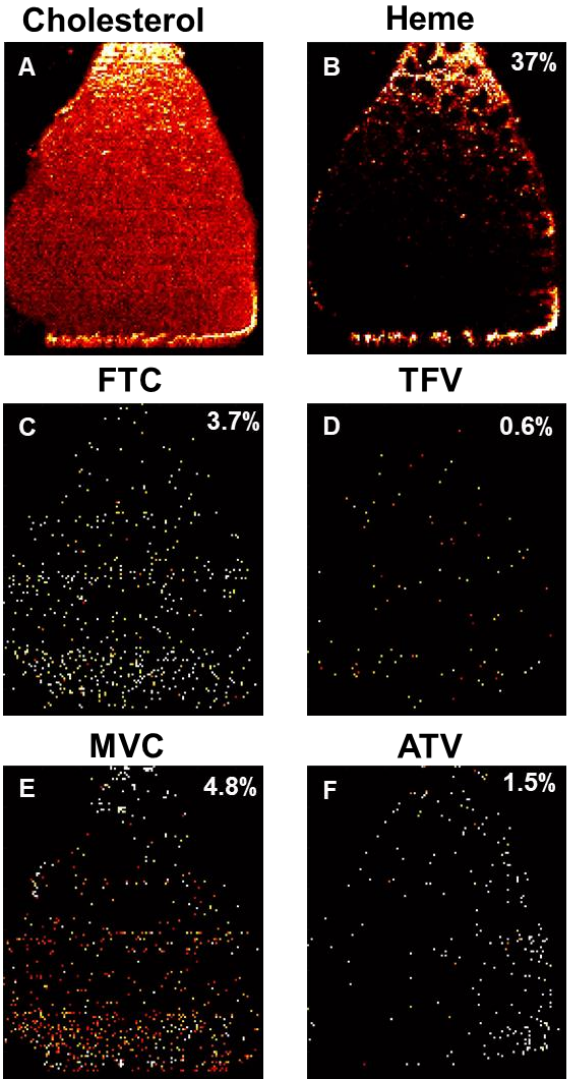

Intensity-scaled MSI images of the distribution of cholesterol (A), heme (B), FTC (C), TFV (D), MVC (E), and ATV (F) in an RT-SHIV+ NHP. Percentages in the top-right corner indicate the MSI area covered by each target. Brighter colors (white and yellow) represent higher MSI signal intensities whereas darker colors (black and red) represent the converse. Abbreviations: FTC, emtricitabine; TFV, tenofovir; MVC, maraviroc; ATV, atazanavir; MSI, mass spectrometry imaging; RT-SHIV, reverse trascriptase simian-human immunodeficiency virus; NHP, nonhuman primate. Located M:\DPET\CPAC General Lab\GRADUATE STUDENTS\Aaron D\Spleen\MALDESI

APPENDIX 3.17: ADDITIONAL INTENSITY-SCALED MSI IMAGE #14

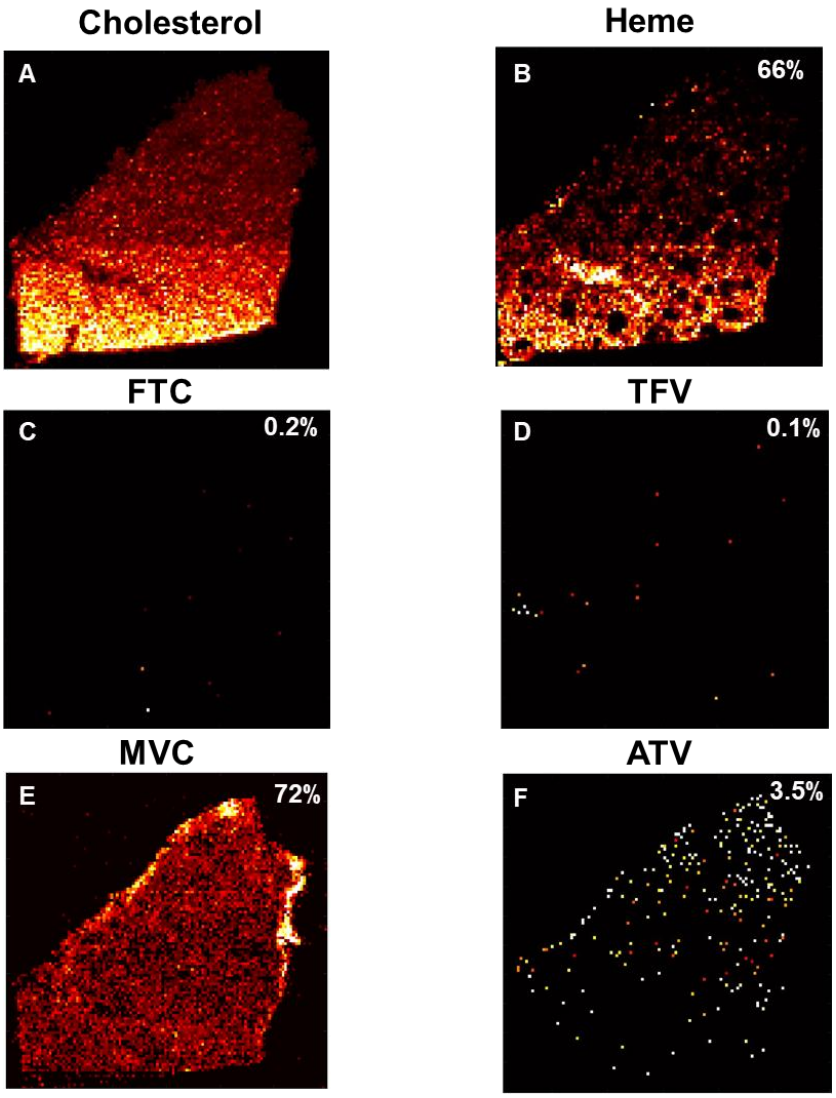

Intensity-scaled MSI images of the distribution of cholesterol (A), heme (B), FTC (C), TFV (D), MVC (E), and ATV (F) in an RT-SHIV- NHP. Percentages in the top-right corner indicate the MSI area covered by each target. Brighter colors (white and yellow) represent higher MSI signal intensities whereas darker colors (black and red) represent the converse. Abbreviations: FTC, emtricitabine; TFV, tenofovir; MVC, maraviroc; ATV, atazanavir; MSI, mass spectrometry imaging; RT-SHIV, reverse trascriptase simian-human immunodeficiency virus; NHP, nonhuman primate. Located M:\DPET\CPAC General Lab\GRADUATE STUDENTS\Aaron D\Spleen\MALDESI

APPENDIX 3.18: ADDITIONAL INTENSITY-SCALED MSI IMAGE #15

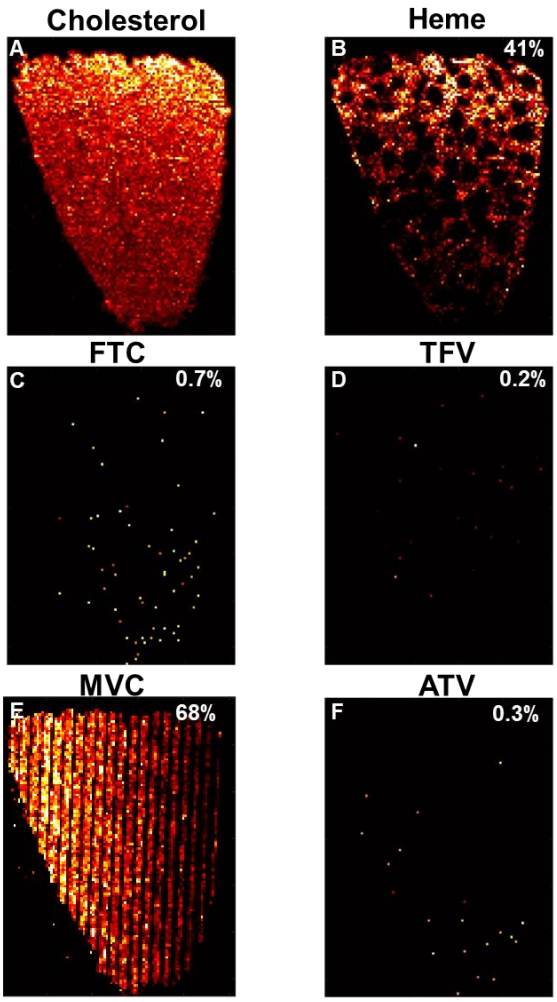

Intensity-scaled MSI images of the distribution of cholesterol (A), heme (B), FTC (C), TFV (D), MVC (E), and ATV (F) in an RT-SHIV+ NHP. Percentages in the top-right corner indicate the MSI area covered by each target. Brighter colors (white and yellow) represent higher MSI signal intensities whereas darker colors (black and red) represent the converse. Abbreviations: FTC, emtricitabine; TFV, tenofovir; MVC, maraviroc; ATV, atazanavir; MSI, mass spectrometry imaging; RT-SHIV, reverse trascriptase simian-human immunodeficiency virus; NHP, nonhuman primate. Located M:\DPET\CPAC General Lab\GRADUATE STUDENTS\Aaron D\Spleen\MALDESI

APPENDIX 3.19: ADDITIONAL INTENSITY-SCALED MSI IMAGE #16

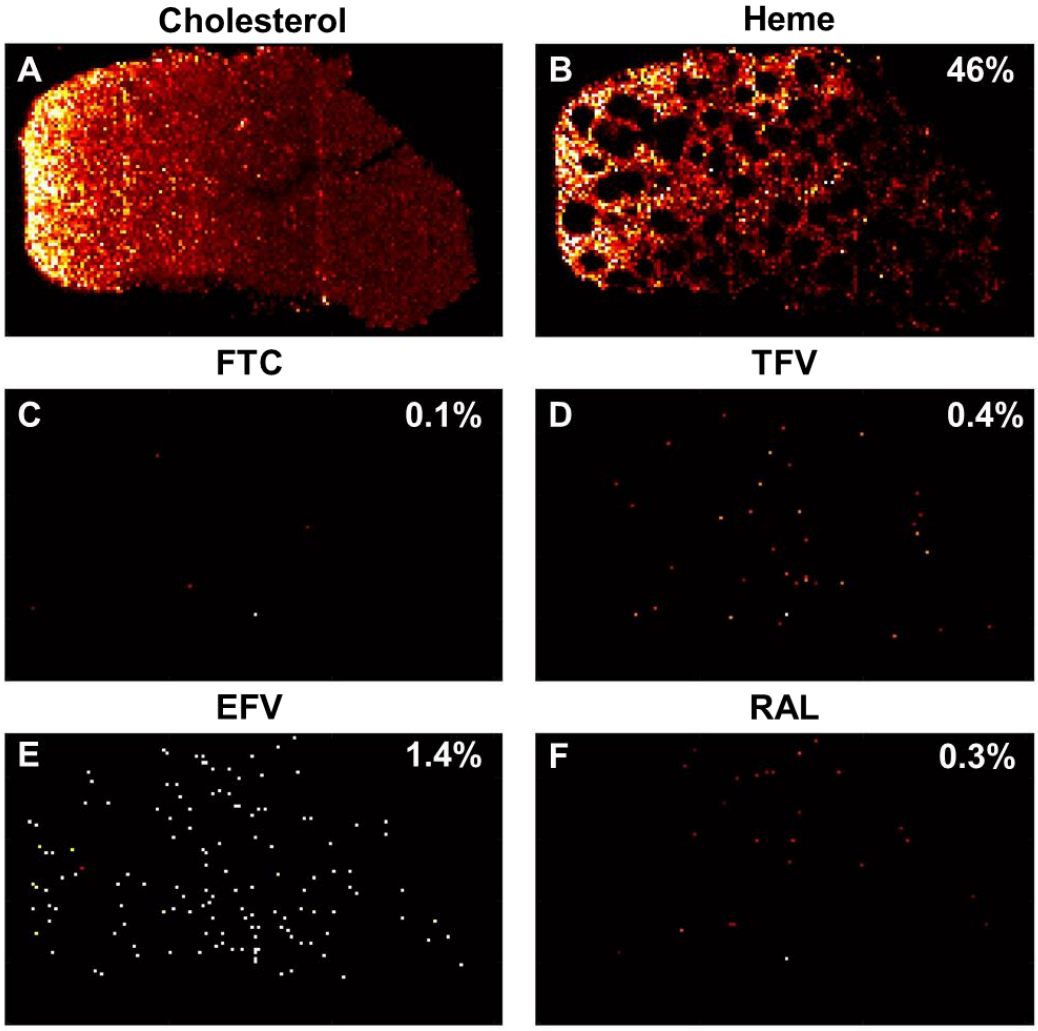

Intensity-scaled MSI images of the distribution of cholesterol (A), heme (B), FTC (C), TFV (D), EFV (E), and RAL (F) in an RT-SHIV+ NHP. Percentages in the top-right corner indicate the MSI area covered by each target. Brighter colors (white and yellow) represent higher MSI signal intensities whereas darker colors (black and red) represent the converse. Abbreviations: FTC, emtricitabine; TFV, tenofovir; MVC, maraviroc; ATV, atazanavir; MSI, mass spectrometry imaging; RT-SHIV, reverse trascriptase simian-human immunodeficiency virus; NHP, nonhuman primate. Located M:\DPET\CPAC General Lab\GRADUATE STUDENTS\Aaron D\Spleen\MALDESI

APPENDIX 3.20: ADDITIONAL CELL-ASSOCIATED RNA IMAGE #1

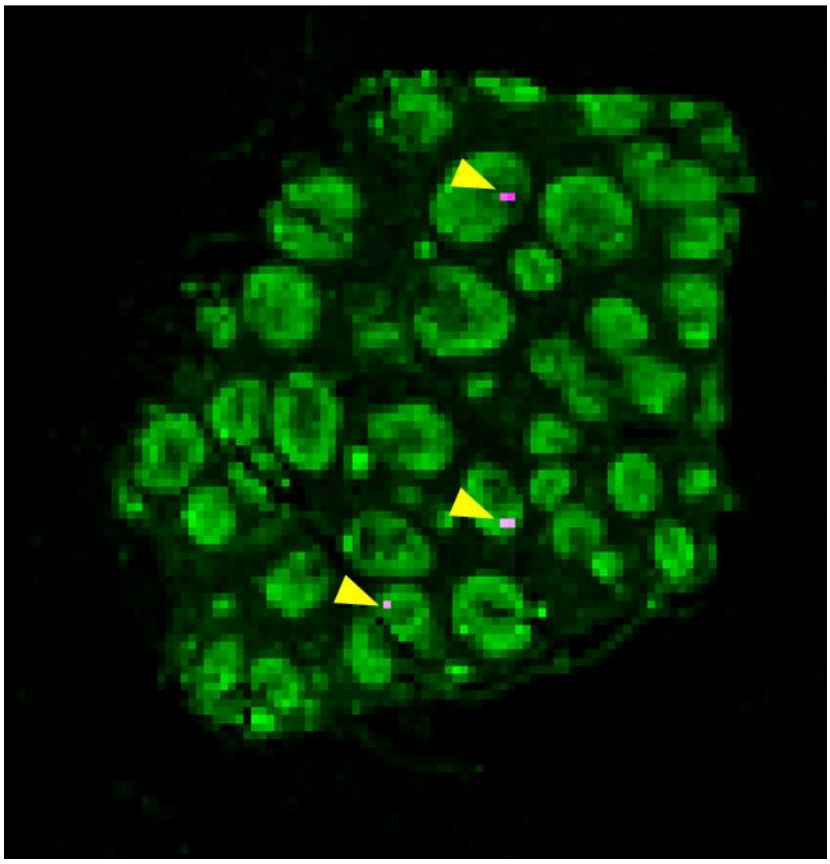

Image of the cell-associated RNA (magenta) in the RT-SHIV+ NHP 40437 and CD3+T cells (in green). Yellow arrows indicate locations of caRNA
Abbreviations: caRNA, cell-associated RNA; RT-SHIV, reverse transcriptase simian-human immunodeficiency virus; NHP, nonhuman primate. Located M:\DPET\CPAC General Lab\GRADUATE STUDENTS\Aaron D\Spleen\ISH

APPENDIX 3.21: ADDITIONAL CELL-ASSOCIATED RNA IMAGE #2

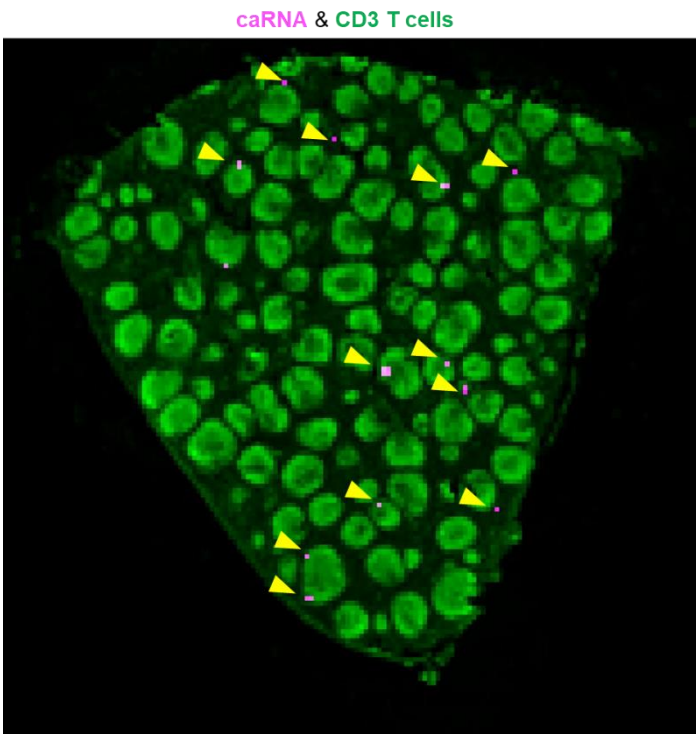

Image of the cell-associated RNA (magenta) in the RT-SHIV+ NHP 41380 and CD3+T cells (in green). Yellow arrows indicate locations of caRNA Abbreviations: caRNA, cell-associated RNA; RT-SHIV, reverse transcriptase simian-human immunodeficiency virus; NHP, nonhuman primate. Located M:\DPET\CPAC General Lab\GRADUATE STUDENTS\Aaron D\Spleen\ISH

APPENDIX 3.22: ADDITIONAL CELL-ASSOCIATED RNA IMAGE #3

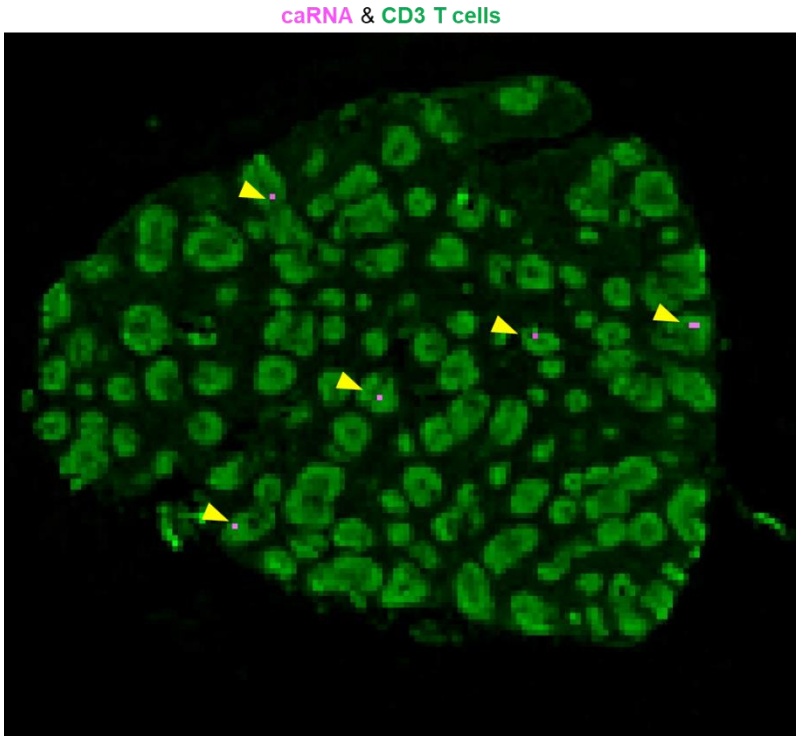

Image of the cell-associated RNA (magenta) in the RT-SHIV+ NHP 42226 and CD3+T cells (in green). Yellow arrows indicate locations of caRNA
Abbreviations: caRNA, cell-associated RNA; RT-SHIV, reverse transcriptase simian-human immunodeficiency virus; NHP, nonhuman primate. Located M:\DPET\CPAC General Lab\GRADUATE STUDENTS\Aaron D\Spleen\ISH

APPENDIX 3.23: ADDITIONAL CELL-ASSOCIATED RNA IMAGE #4

caRNA & CD3 T cells

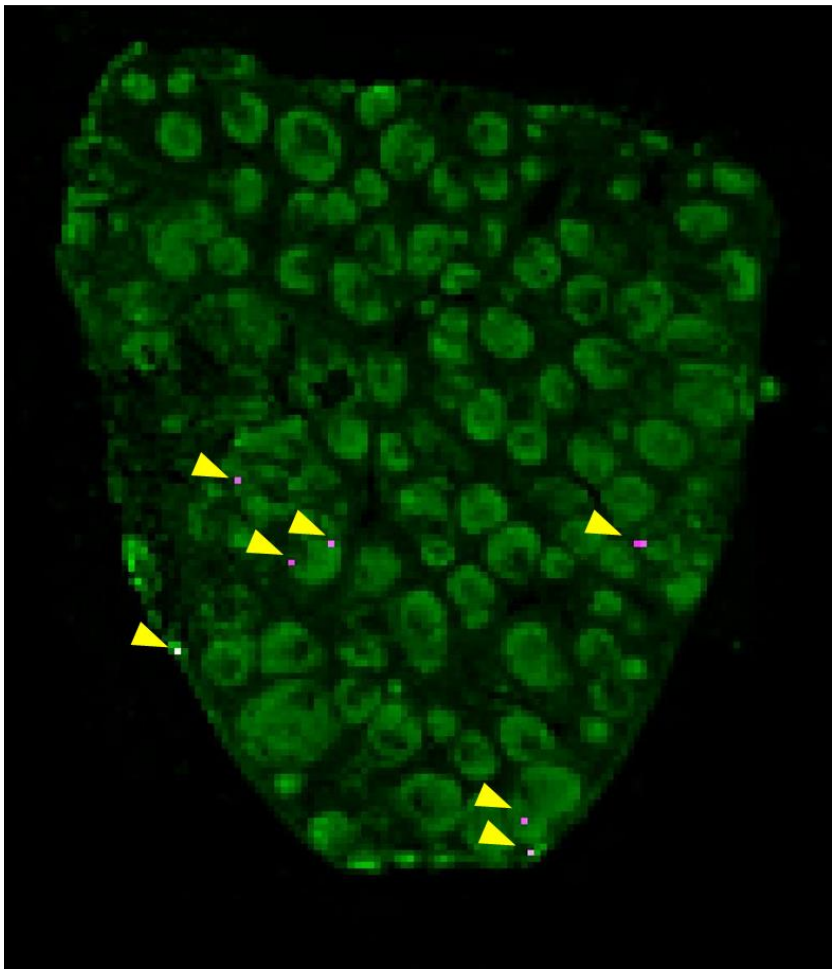

Image of the cell-associated RNA (magenta) in the RT-SHIV+ NHP 42350 and CD3+T cells (in green). Yellow arrows indicate locations of caRNA Abbreviations: caRNA, cell-associated RNA; RT-SHIV, reverse transcriptase simian-human immunodeficiency virus; NHP, nonhuman primate. Located M:\DPET\CPAC General Lab\GRADUATE STUDENTS\Aaron D\Spleen\ISH

APPENDIX 3.24: ADDITIONAL CELL-ASSOCIATED RNA IMAGE #5

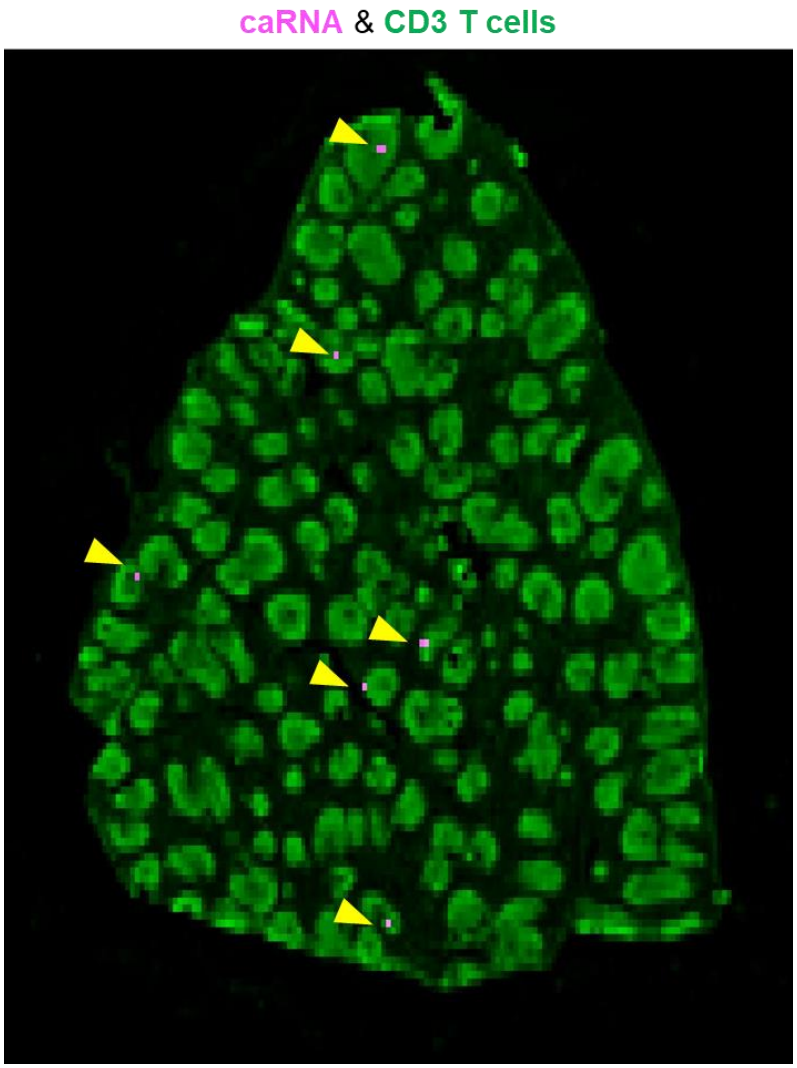

Image of the cell-associated RNA (magenta) in the RT-SHIV+ NHP 42706 and CD3+T cells (in green). Yellow arrows indicate locations of caRNA Abbreviations: caRNA, cell-associated RNA; RT-SHIV, reverse transcriptase simian-human immunodeficiency virus; NHP, nonhuman primate. Located M:\DPET\CPAC General Lab\GRADUATE STUDENTS\Aaron D\Spleen\ISH

APPENDIX 3.25: ADDITIONAL CELL-ASSOCIATED RNA IMAGE #6

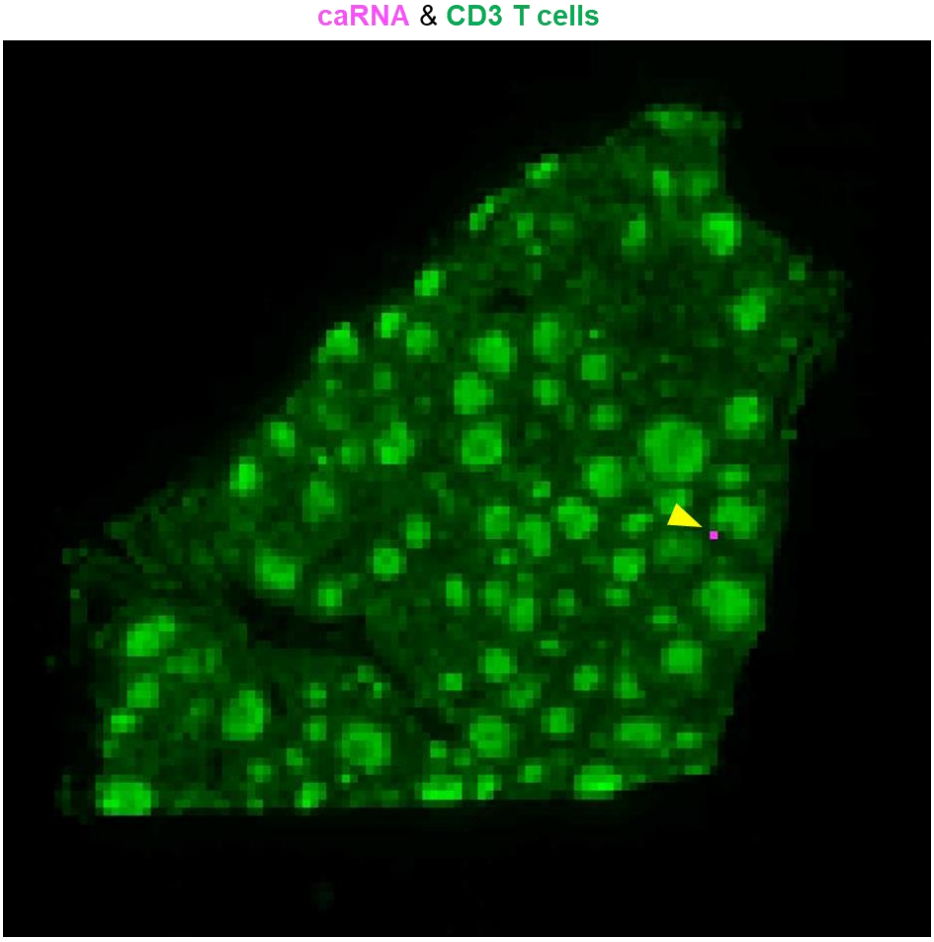

Image of the cell-associated RNA (magenta) in the RT-SHIV+ NHP 42528 and CD3+T cells (in green). Yellow arrows indicate locations of caRNA
Abbreviations: caRNA, cell-associated RNA; RT-SHIV, reverse transcriptase simian-human immunodeficiency virus; NHP, nonhuman primate. Located M:\DPET\CPAC General Lab\GRADUATE STUDENTS\Aaron D\Spleen\ISH

APPENDIX 3.26: ADDITIONAL CELL-ASSOCIATED RNA IMAGE #7

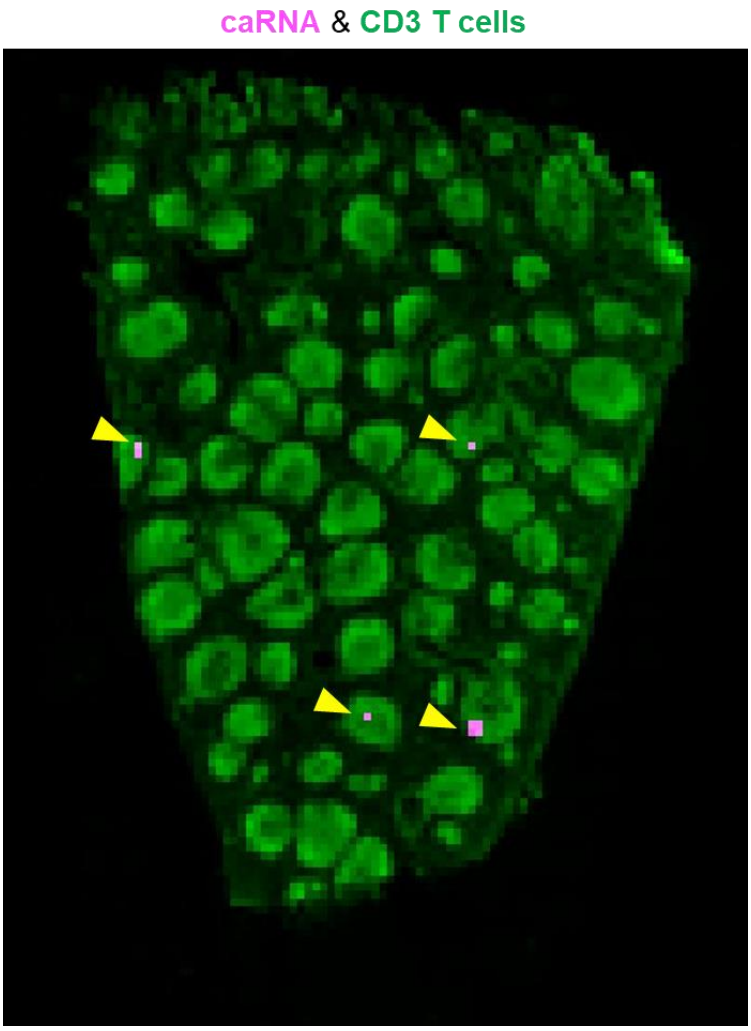

Image of the cell-associated RNA (magenta) in the RT-SHIV+ NHP 42966 and CD3+T cells (in green). Yellow arrows indicate locations of caRNA Abbreviations: caRNA, cell-associated RNA; RT-SHIV, reverse transcriptase simian-human immunodeficiency virus; NHP, nonhuman primate. Located M:\DPET\CPAC General Lab\GRADUATE STUDENTS\Aaron D\Spleen\ISH

APPENDIX 3.27: ADDITIONAL CELL-ASSOCIATED RNA IMAGE #8

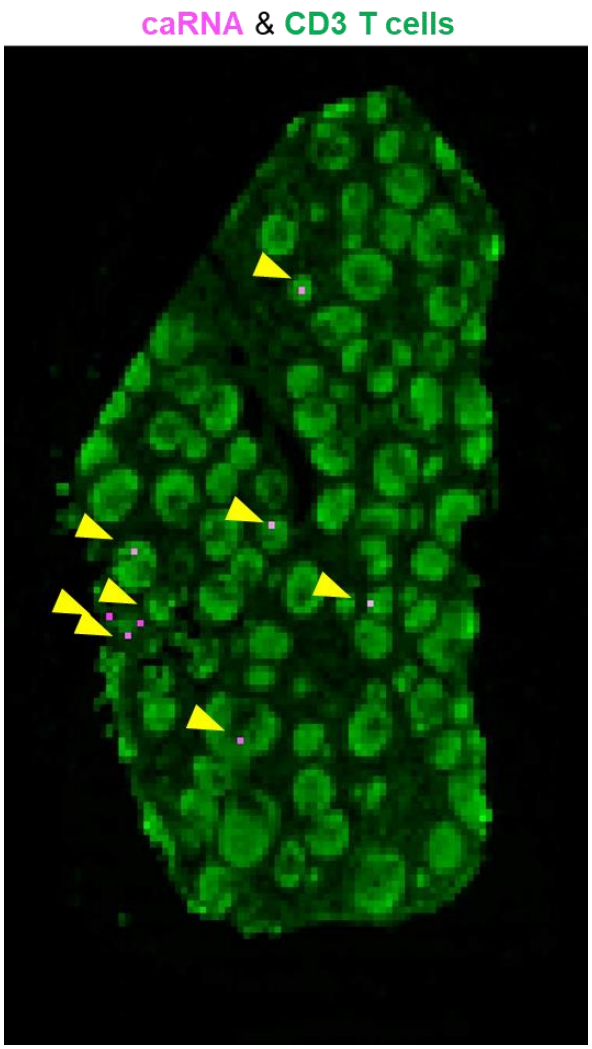

Image of the cell-associated RNA (magenta) in the RT-SHIV+ NHP 42971 and CD3+T cells (in green). Yellow arrows indicate locations of caRNA Abbreviations: caRNA, cell-associated RNA; RT-SHIV, reverse transcriptase simian-human immunodeficiency virus; NHP, nonhuman primate. Located M:\DPET\CPAC General Lab\GRADUATE STUDENTS\Aaron D\Spleen\ISH

APPENDIX 3.28: ADDITIONAL FOLLICULAR DENDRITIC CELL-ASSOCIATED RNA IMAGE #1

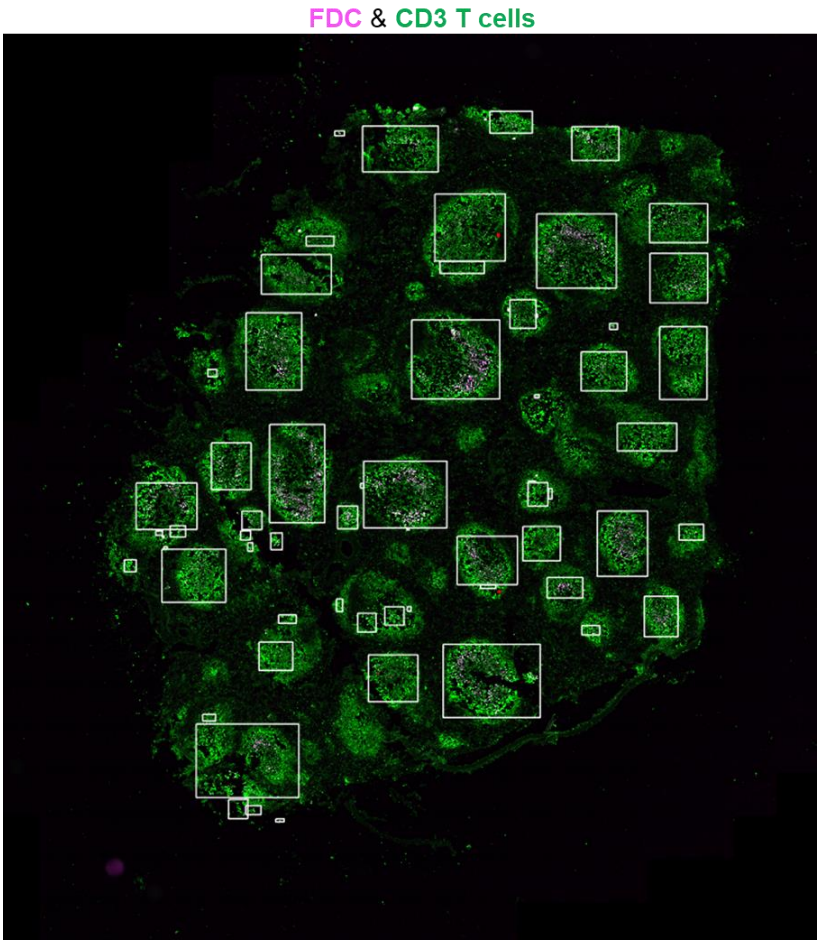

Image of the FDC RNA (magenta) in the RT-SHIV+ NHP 40437 and CD3+T cells (in green). White boxes indicate locations of FDC-associated RNA Abbreviations: FDC, follicular dendritic cell; RT-SHIV, reverse transcriptase simian-human immunodeficiency virus; NHP, nonhuman primate. Located M:\DPET\CPAC General Lab\GRADUATE STUDENTS\Aaron D\Spleen\ISH

APPENDIX 3.29: ADDITIONAL FOLLICULAR DENDRITIC CELL-ASSOCIATED RNA IMAGE #2

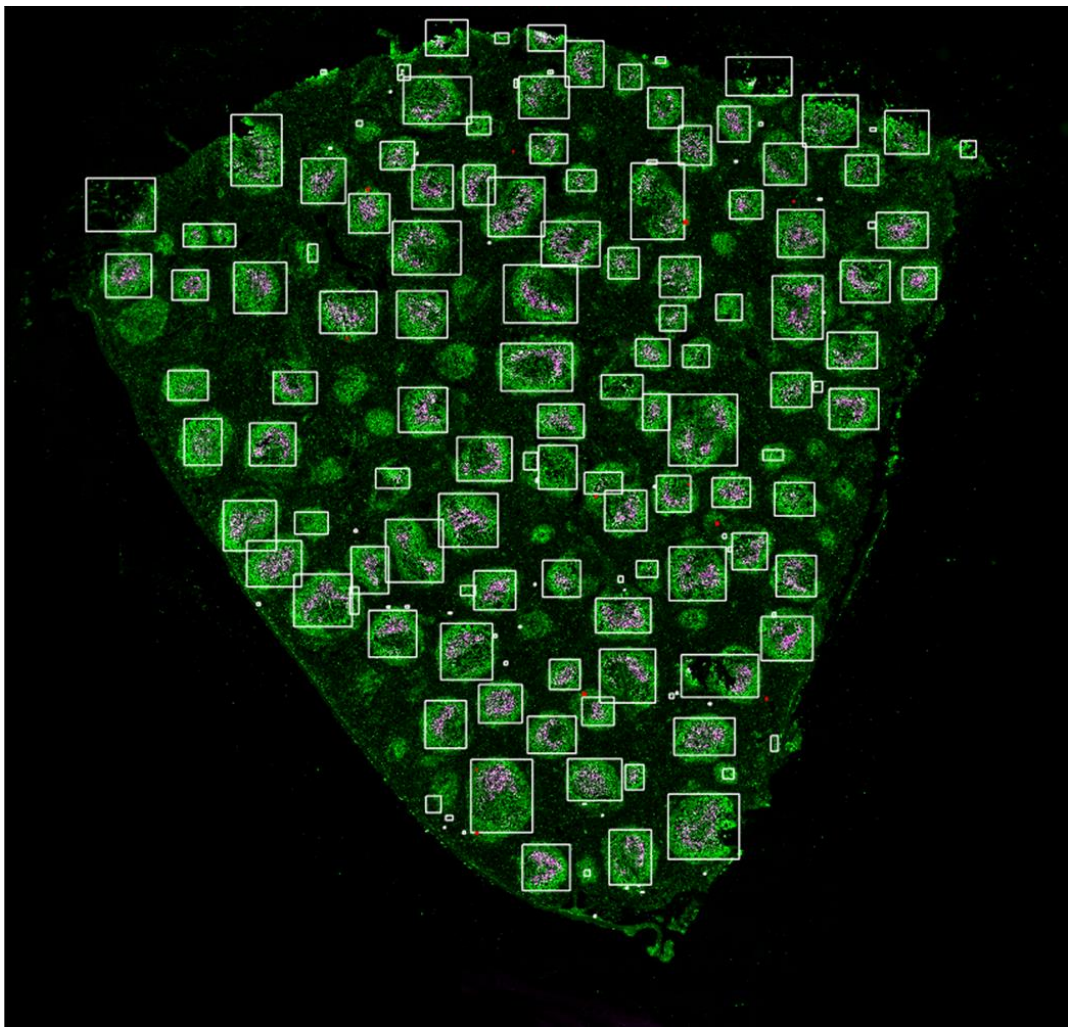

Image of the FDC RNA (magenta) in the RT-SHIV+ NHP 41380 and CD3+T cells (in green). White boxes indicate locations of FDC-associated RNA Abbreviations: FDC, follicular dendritic cell; RT-SHIV, reverse transcriptase simian-human immunodeficiency virus; NHP, nonhuman primate. Located M:\DPET\CPAC General Lab\GRADUATE STUDENTS\Aaron D\Spleen\ISH

APPENDIX 3.30: ADDITIONAL FOLLICULAR DENDRITIC CELL-ASSOCIATED RNA IMAGE #3

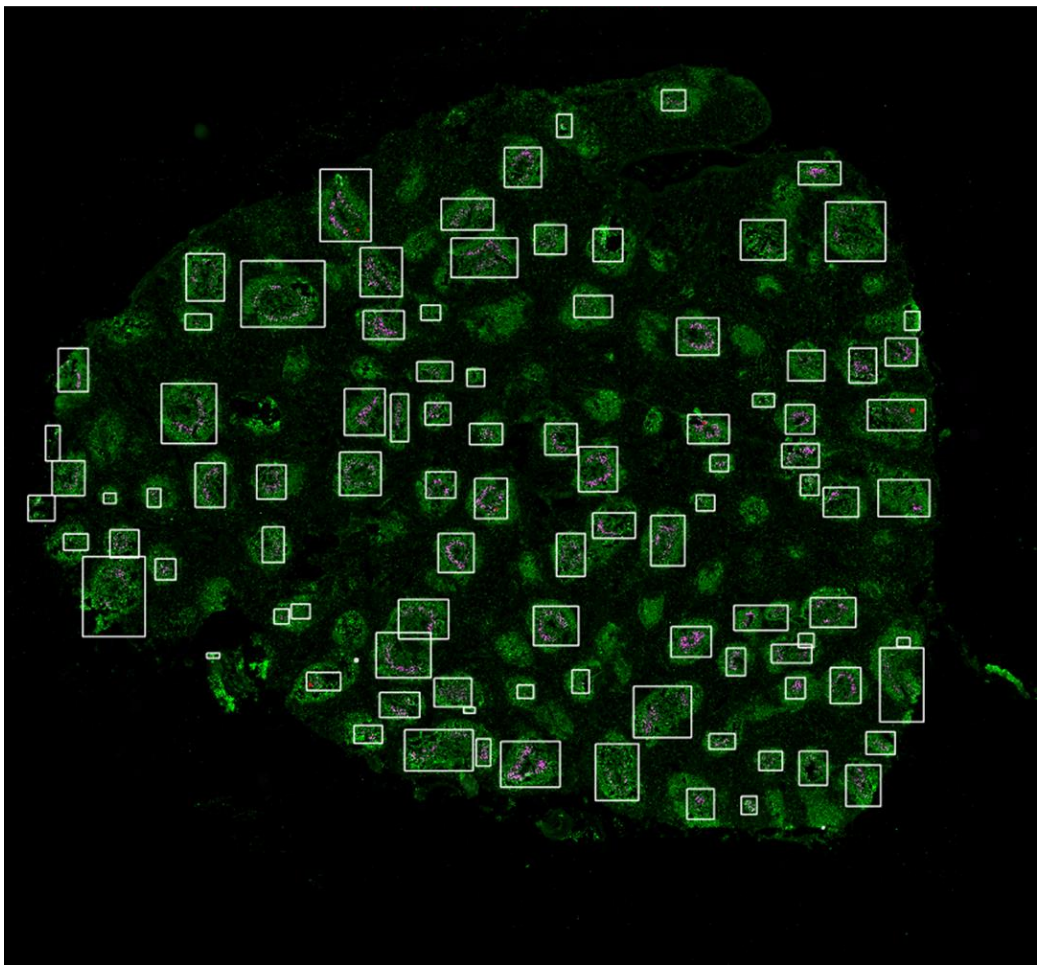

Image of the FDC RNA (magenta) in the RT-SHIV+ NHP 42226 and CD3+T cells (in green). White boxes indicate locations of FDC-associated RNA
Abbreviations: FDC, follicular dendritic cell; RT-SHIV, reverse transcriptase simian-human immunodeficiency virus; NHP, nonhuman primate. Located M:\DPET\CPAC General Lab\GRADUATE STUDENTS\Aaron D\Spleen\ISH

APPENDIX 3.31: ADDITIONAL FOLLICULAR DENDRITIC CELL-ASSOCIATED RNA IMAGE #4

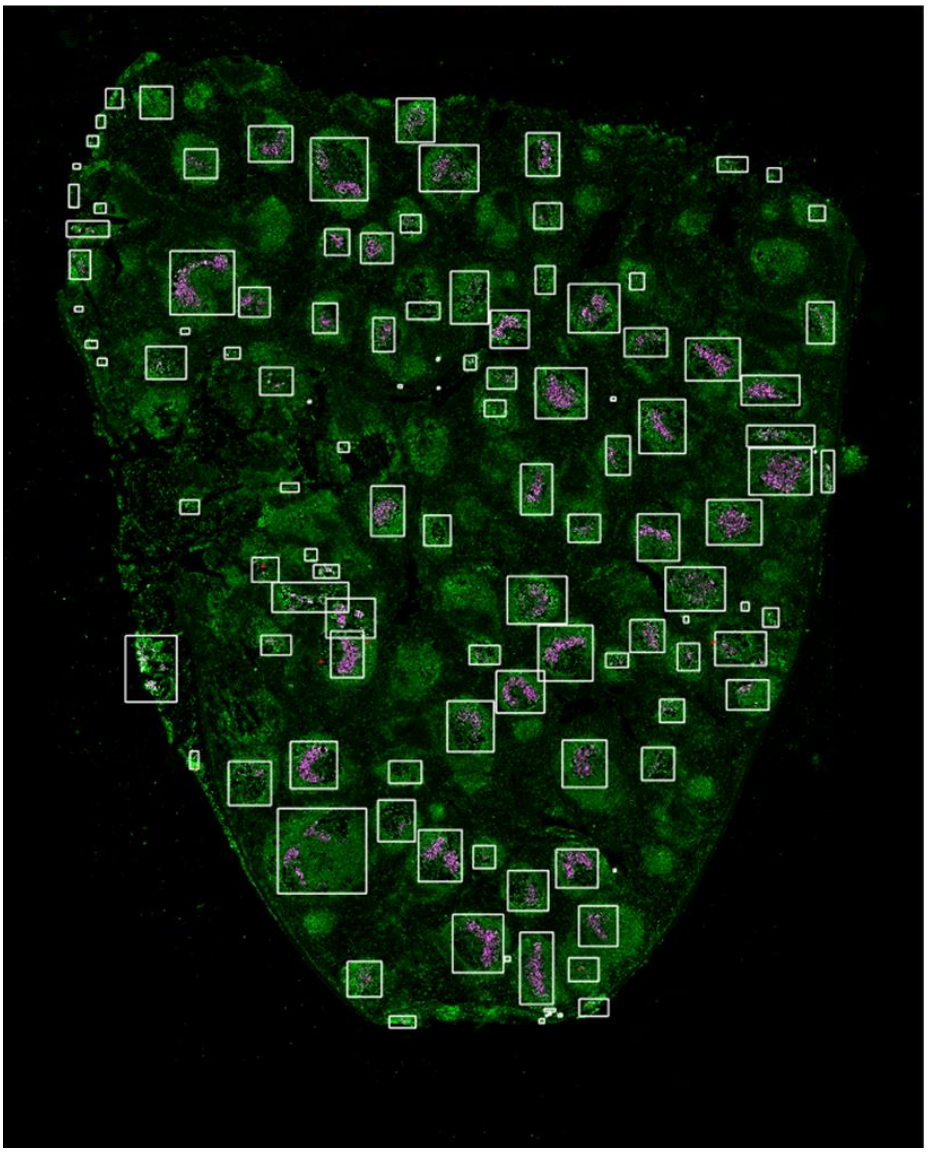

Image of the FDC RNA (magenta) in the RT-SHIV+ NHP 42350 and CD3+T cells (in green). White boxes indicate locations of FDC-associated RNA Abbreviations: FDC, follicular dendritic cell; RT-SHIV, reverse transcriptase simian-human immunodeficiency virus; NHP, nonhuman primate. Located M:\DPET\CPAC General Lab\GRADUATE STUDENTS\Aaron D\Spleen\ISH

APPENDIX 3.32: ADDITIONAL FOLLICULAR DENDRITIC CELL-ASSOCIATED RNA IMAGE #5

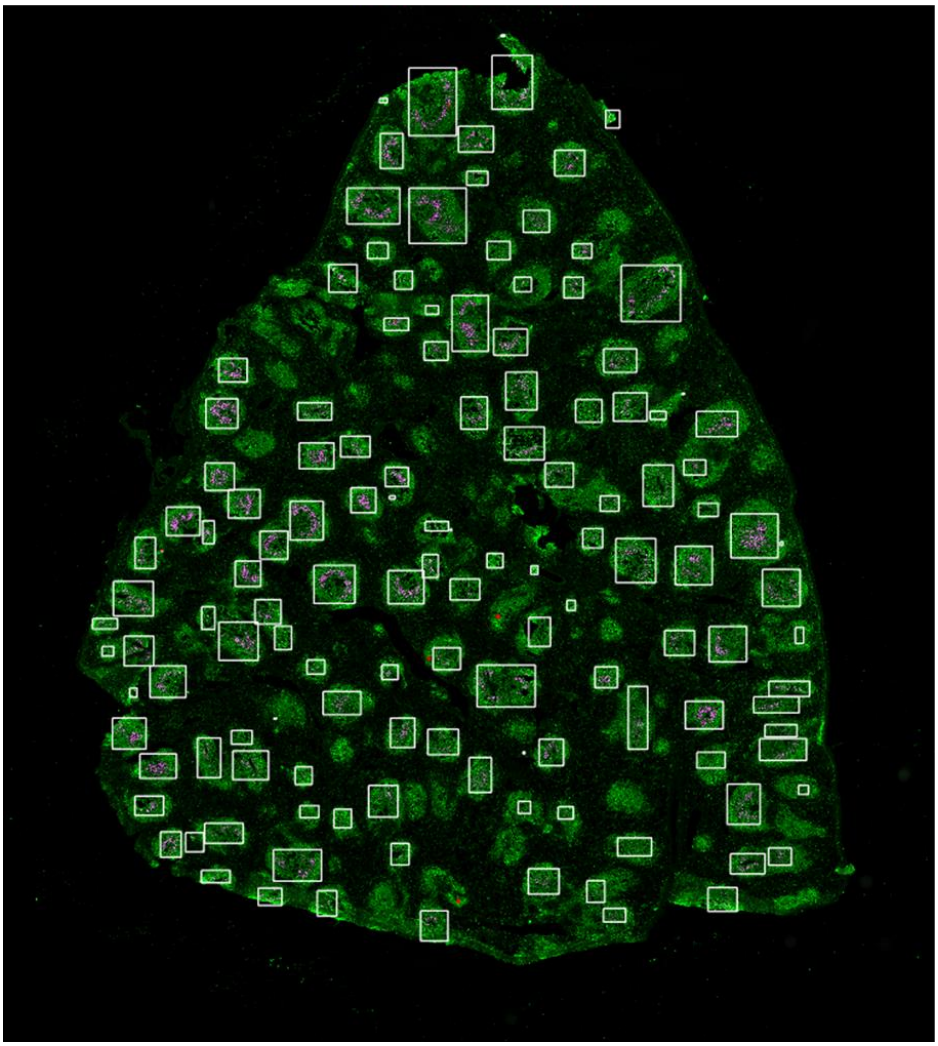

Image of the FDC RNA (magenta) in the RT-SHIV+ NHP 42706 and CD3+T cells (in green). White boxes indicate locations of FDC-associated RNA Abbreviations: FDC, follicular dendritic cell; RT-SHIV, reverse transcriptase simian-human immunodeficiency virus; NHP, nonhuman primate. Located M:\DPET\CPAC General Lab\GRADUATE STUDENTS\Aaron D\Spleen\ISH

APPENDIX 3.33: ADDITIONAL FOLLICULAR DENDRITIC CELL-ASSOCIATED RNA IMAGE #6

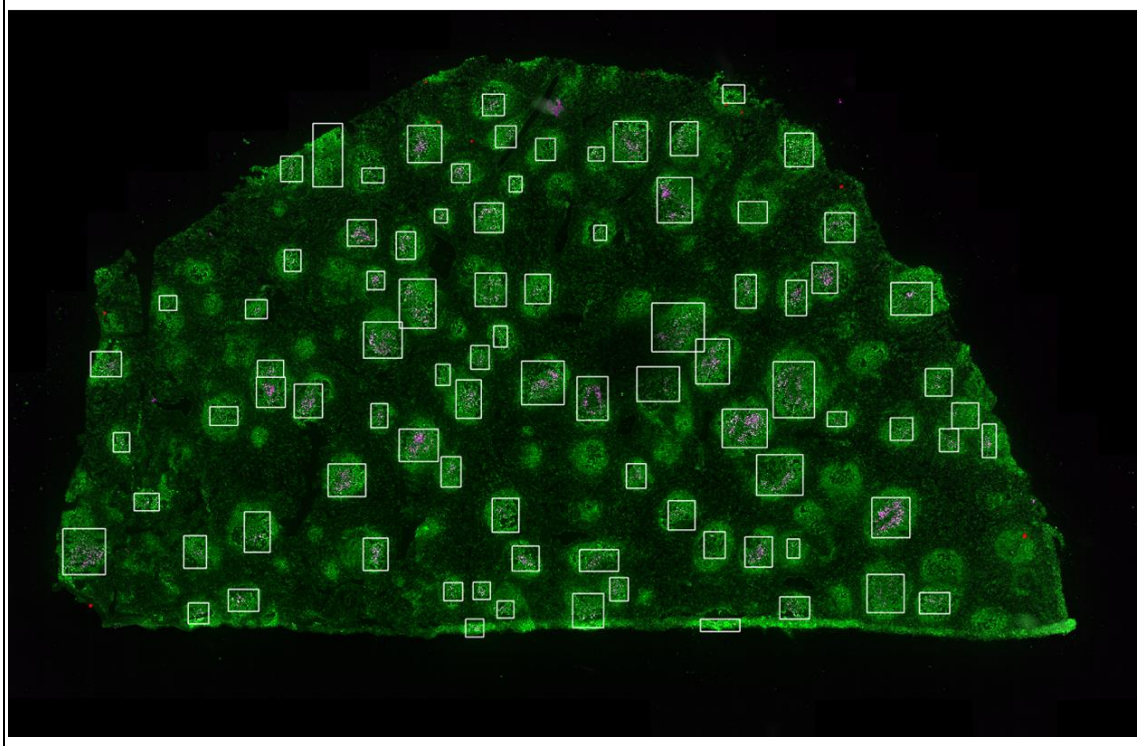

Image of the FDC RNA (magenta) in the RT-SHIV+ NHP 42707 and CD3+T cells (in green). White boxes indicate locations of FDC-associated RNA Abbreviations: FDC, follicular dendritic cell; RT-SHIV, reverse transcriptase simian-human immunodeficiency virus; NHP, nonhuman primate. Located M:\DPET\CPAC General Lab\GRADUATE STUDENTS\Aaron D\Spleen\ISH

APPENDIX 3.34: ADDITIONAL FOLLICULAR DENDRITIC CELL-ASSOCIATED RNA IMAGE #7

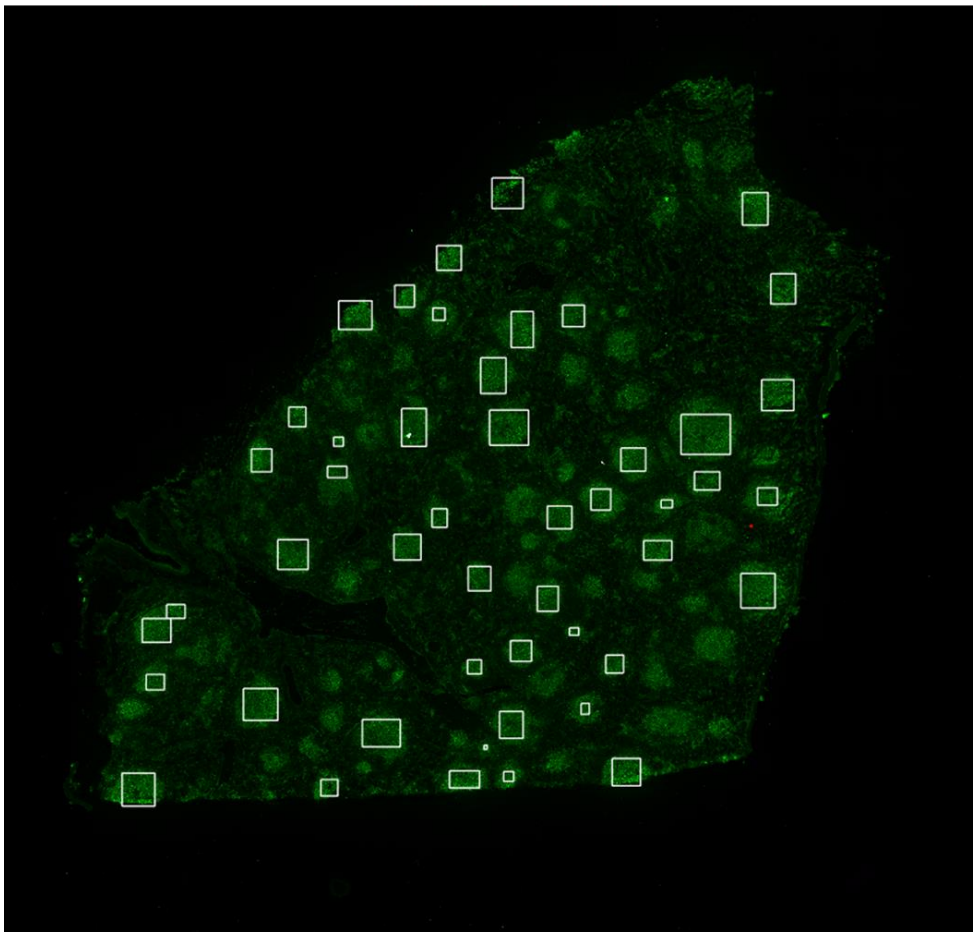

Image of the FDC RNA (magenta) in the RT-SHIV+ NHP 42528 and CD3+T cells (in green). White boxes indicate locations of FDC-associated RNA Abbreviations: FDC, follicular dendritic cell; RT-SHIV, reverse transcriptase simian-human immunodeficiency virus; NHP, nonhuman primate. Located M:\DPET\CPAC General Lab\GRADUATE STUDENTS\Aaron D\Spleen\ISH

APPENDIX 3.35: ADDITIONAL FOLLICULAR DENDRITIC CELL-ASSOCIATED RNA IMAGE #8

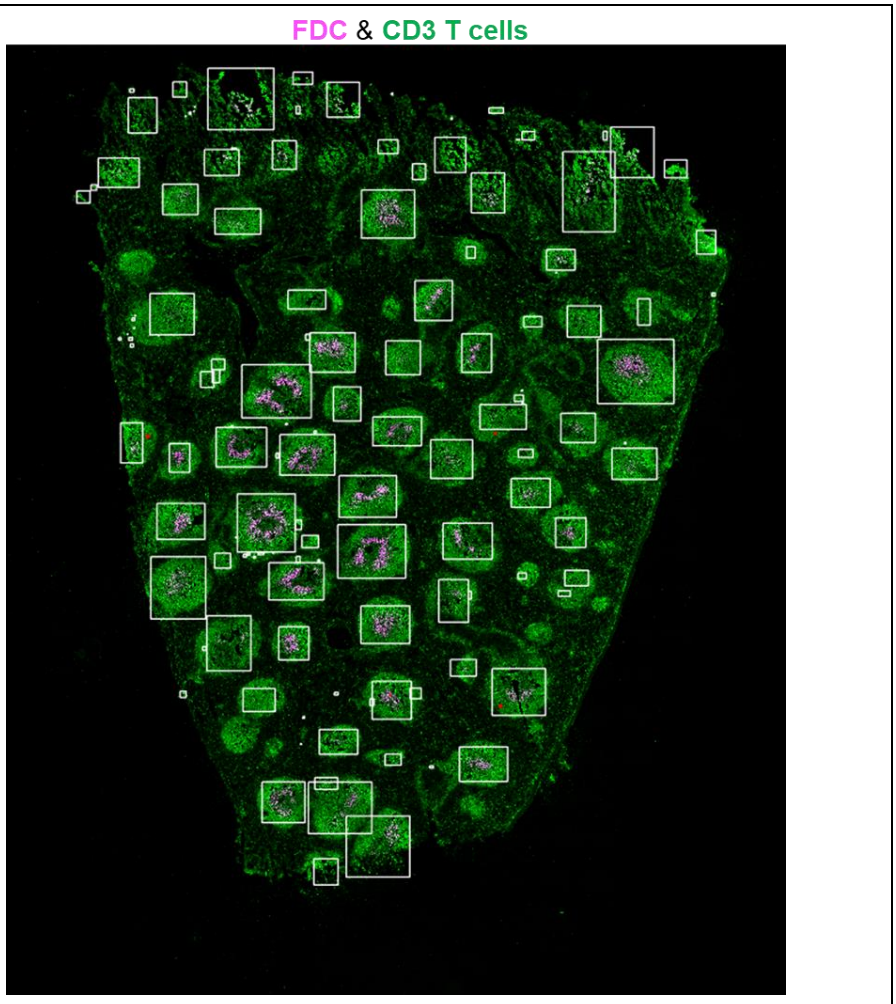

Image of the FDC RNA (magenta) in the RT-SHIV+ NHP 42966 and CD3+T cells (in green). White boxes indicate locations of FDC-associated RNA Abbreviations: FDC, follicular dendritic cell; RT-SHIV, reverse transcriptase simian-human immunodeficiency virus; NHP, nonhuman primate. Located M:\DPET\CPAC General Lab\GRADUATE STUDENTS\Aaron D\Spleen\ISH

APPENDIX 3.36: ADDITIONAL FOLLICULAR DENDRITIC CELL-ASSOCIATED RNA IMAGE #9

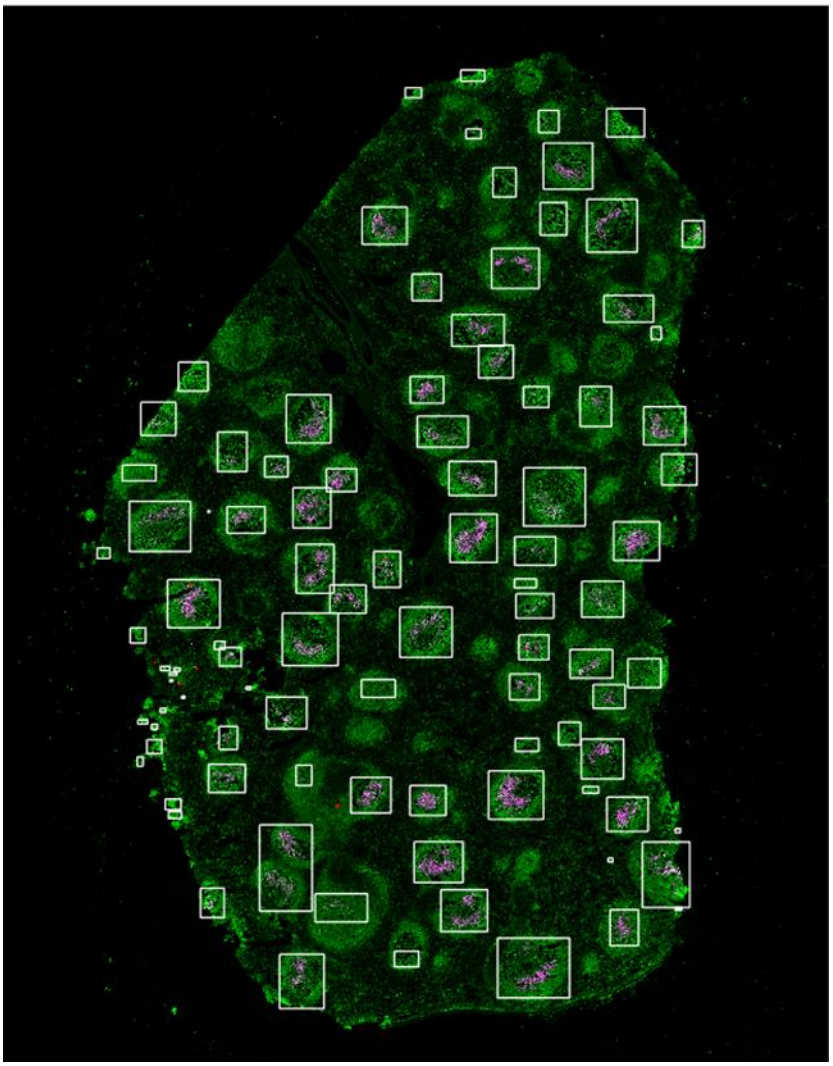

Image of the FDC RNA (magenta) in the RT-SHIV+ NHP 42971 and CD3+T cells (in green). White boxes indicate locations of FDC-associated RNA Abbreviations: FDC, follicular dendritic cell; RT-SHIV, reverse transcriptase simian-human immunodeficiency virus; NHP, nonhuman primate. Located M:\DPET\CPAC General Lab\GRADUATE STUDENTS\Aaron D\Spleen\ISH

APPENDIX 3.37: CORRELATION PLOTS OF HEME-CORRECTED CUMULATIVE ARV TISSUE COVERAGE VERSUS FIBROSIS MARKER COVERAGE

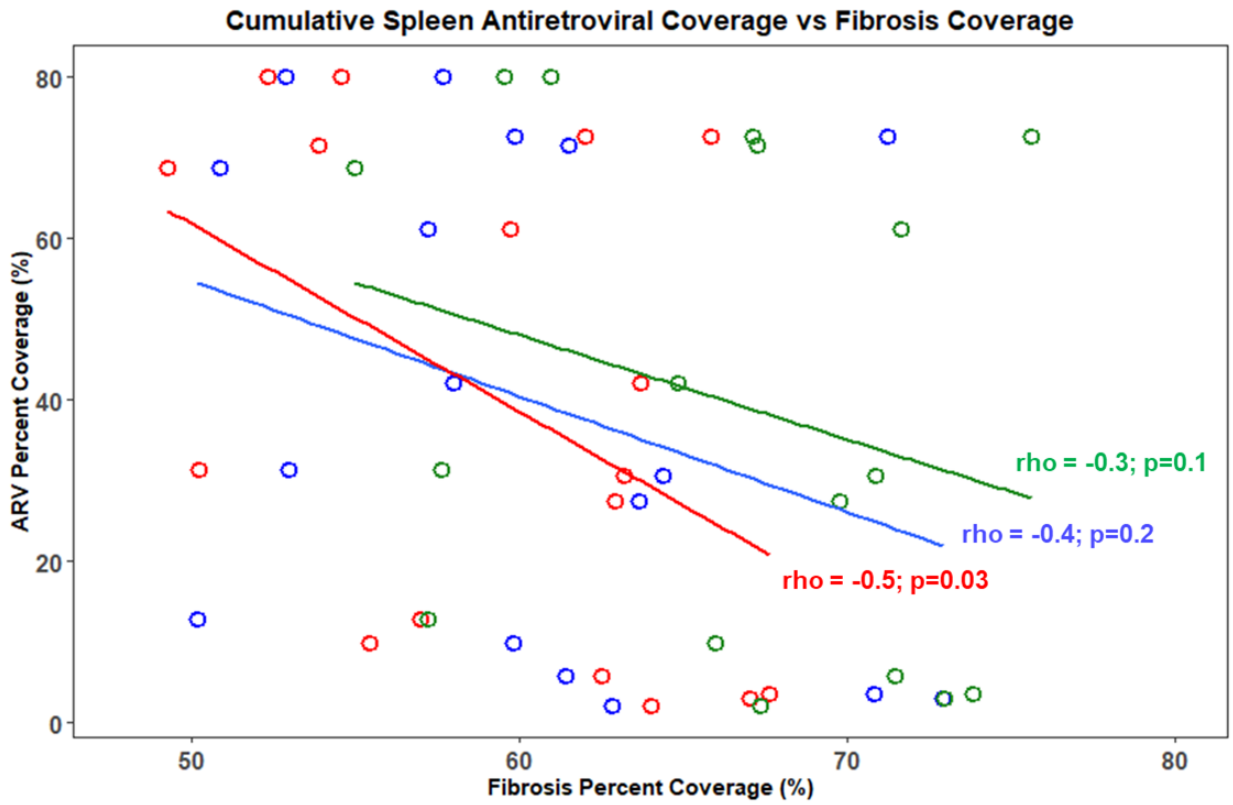

Correlation plots of heme-corrected cumulative ARV tissue coverage versus fibrosis marker coverage. Open circles represent the paired NHP (n=17 total) data points of coverages for collagen 1 (blue), collagen 3 (red), and fibrinogen (green). Correlations (rho) and associated p-values calculated by the nonparametric Spearman's rank correlation. ARV, antiretroviral; NHP, nonhuman primate.

APPENDIX 4.1: PLASMA VALIDATION IN NHPS

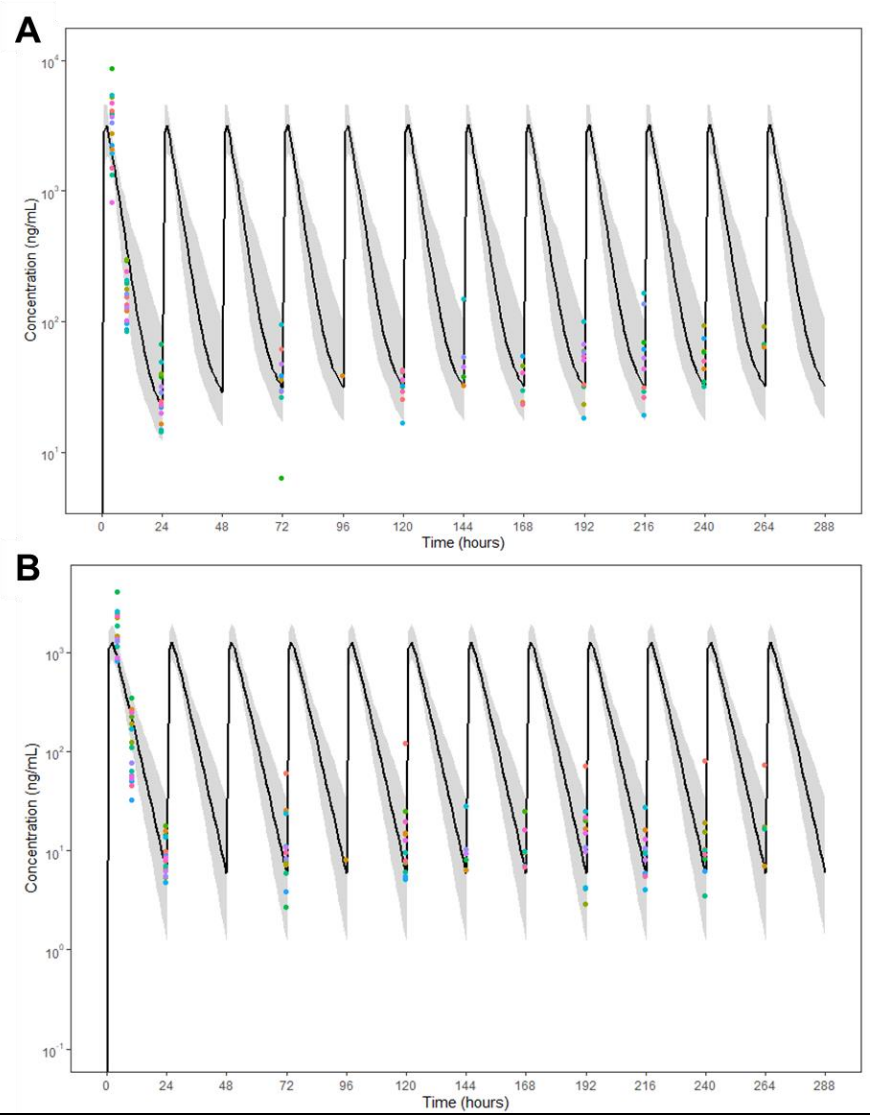

Plasma validation in NHPs for FTC (A) and TFV (B). Colored dots represent individual NHP concentrations. Lines and gray shading represents the median and 5th and 95th percentiles at each time point. Abbreviations: FTC, emtricitabine; TFV, tenofovir; NHP, nonhuman primate.

APPENDIX 4.2: PLASMA VALIDATION IN HUMANS

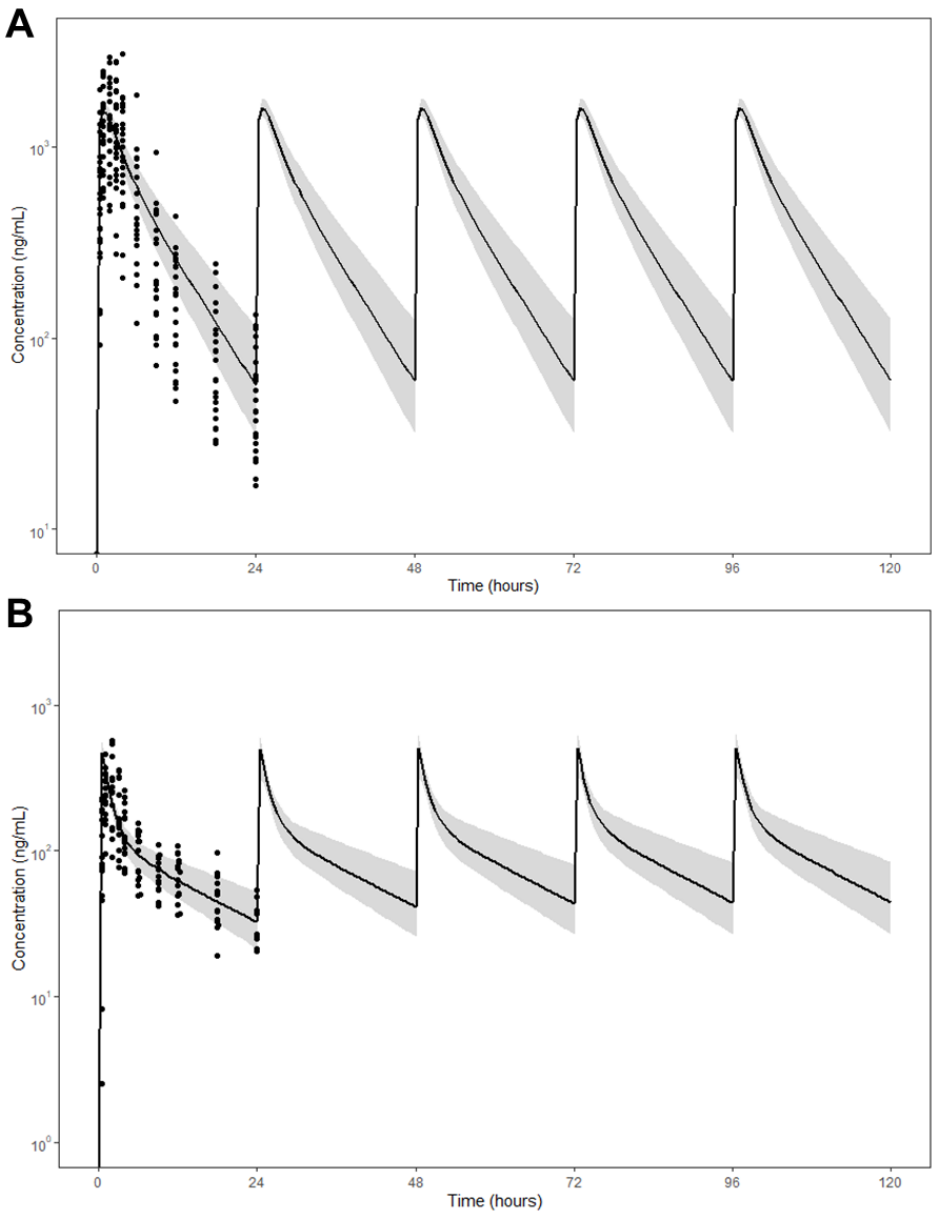

Plasma validation in humans for FTC (A) and TFV (B). Dots represent observed concentration data from Cottrell et al.[157] Lines and gray shading represents the median and 5th and 95th percentiles at each time point. Abbreviations: FTC, emtricitabine; TFV, tenofovir.

APPENDIX 5.1: TISSUE PHARMACOLOGY – THEORY VERSUS REALITY

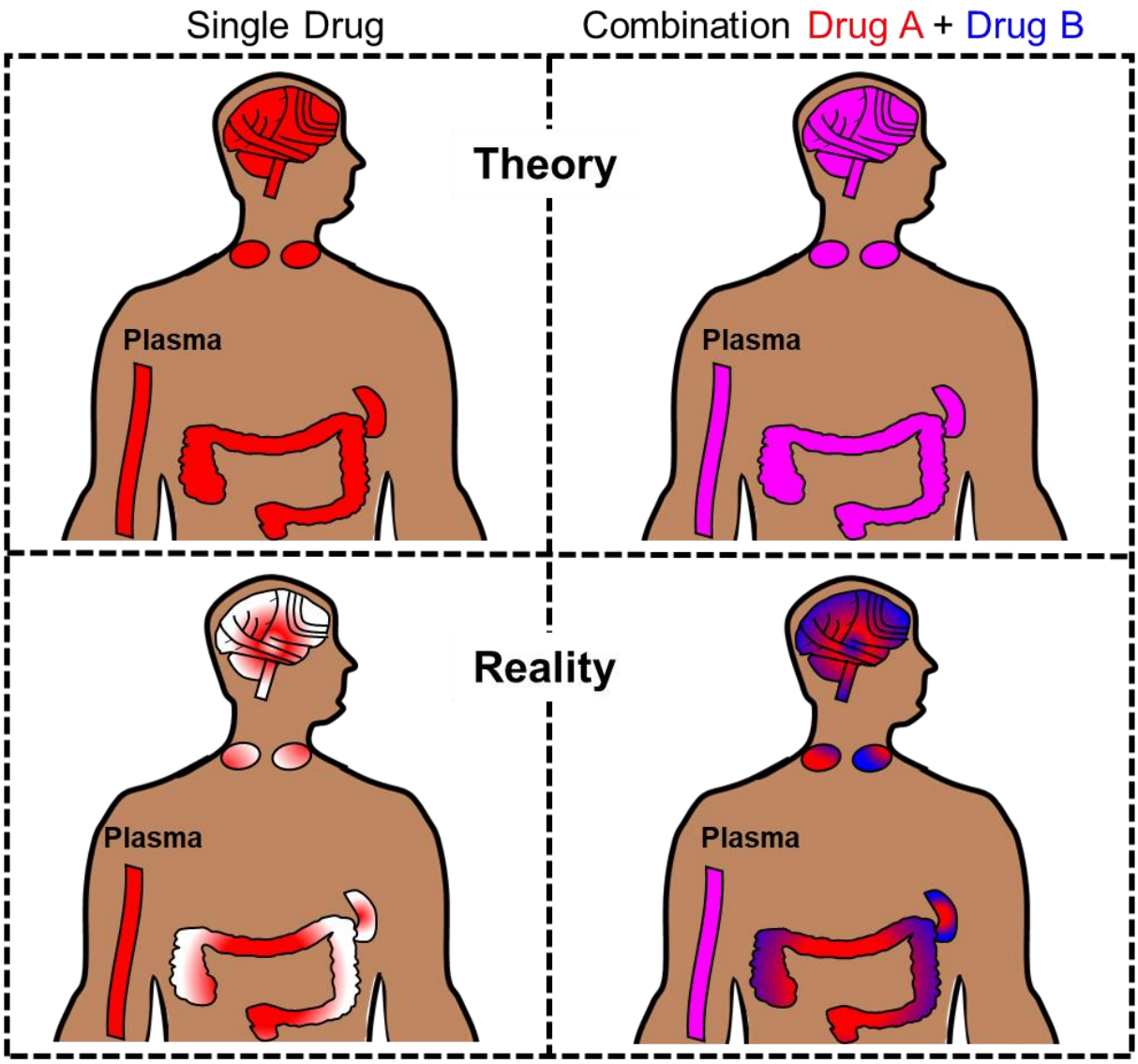

The dichotomy of the theory and reality of drug penetration within tissues, both as a single drug, and a combination of 'Drug A' and 'Drug B'. The overlap of Drug A (red) and Drug B (blue) is visualized as magenta.

APPENDIX 6: GRANTS AND AWARDS

September 2021	**International Workshop on Clinical Pharmacology of HIV, Hepatitis and Other Antiviral Drugs 2021 Best Abstract Award** *Award given to top abstract at the Clinical Pharmacology workshop*
September 2021	**ACCP Student Abstract Award** *Award given to one of eight top abstracts at the ACCP conference*
2021-2022	**AFPE Pre-Doctoral Fellowship in Pharmaceutical Sciences** *National award to doctoral students who demonstrate promising research proposals*
August 2021	**Royster Society of Fellows Inductee** *Prestigious honor given to top graduate students*
August 2021	**Paul Hardin Dissertation Completion Fellowship** *Prestigious honor given to final year doctoral students to support dissertation research*
November 2017	**Three Minute Thesis People's Choice Award Winner** *Award at the UNC Graduate School's 3MT Competition, as determined by audience vote*
August 2017	**Eshelman Recruitment Incentive Award** *For selected incoming students into the PhD program at the UNC Eshelman School of Pharmacy*
August 2017	**Graduate School Doctoral Merit Assistantship** *For selected incoming students into the graduate program at UNC-Chapel Hill*

REFERENCES

1. van Sighem, A. I. *et al.* Life expectancy of recently diagnosed asymptomatic HIV-infected patients approaches that of uninfected individuals. *AIDS* **24**, 1527–1535 (2010).

2. Wong, J. K. *et al.* Recovery of replication-competent HIV despite prolonged suppression of plasma viremia. *Science* **278**, 1291–1295 (1997).

3. Chun, T.-W. *et al.* Rebound of plasma viremia following cessation of antiretroviral therapy despite profoundly low levels of HIV reservoir: implications for eradication. *AIDS* **24**, 2803–2808 (2010).

4. Wong, J. K. & Yukl, S. A. Tissue reservoirs of HIV. *Curr Opin HIV AIDS* **11**, 362–370 (2016).

5. Perelson, A. S. *et al.* Decay characteristics of HIV-1-infected compartments during combination therapy. *Nature* **387**, 188–191 (1997).

6. Siliciano, J. D. *et al.* Long-term follow-up studies confirm the stability of the latent reservoir for HIV-1 in resting CD4+ T cells. *Nat. Med.* **9**, 727–728 (2003).

7. Banga, R. *et al.* PD-1(+) and follicular helper T cells are responsible for persistent HIV-1 transcription in treated aviremic individuals. *Nat. Med.* **22**, 754–761 (2016).

8. García, M. *et al.* Peripheral T follicular helper Cells Make a Difference in HIV Reservoir Size between Elite Controllers and Patients on Successful cART. *Sci. Rep.* **7**, 16799 (2017).

9. Aid, M. *et al.* Follicular CD4 T helper cells as a major HIV reservoir compartment: A molecular perspective. *Front. Immunol.* **9**, 895 (2018).

10. Siliciano, J. D. & Siliciano, R. F. A long-term latent reservoir for HIV-1: discovery and clinical implications. *J. Antimicrob. Chemother.* **54**, 6–9 (2004).

11. Cory, T. J., Schacker, T. W., Stevenson, M. & Fletcher, C. V. Overcoming pharmacologic sanctuaries. *Curr Opin HIV AIDS* **8**, 190–195 (2013).

12. Fletcher, C. V. *et al.* Persistent HIV-1 replication is associated with lower antiretroviral drug concentrations in lymphatic tissues. *Proc. Natl. Acad. Sci. USA* **111**, 2307–2312 (2014).

13. Estes, J. D. *et al.* Defining total-body AIDS-virus burden with implications for curative strategies. *Nat. Med.* **23**, 1271–1276 (2017).

14. Thompson, C. G., Gay, C. L. & Kashuba, A. D. M. HIV Persistence in Gut-Associated Lymphoid Tissues: Pharmacological Challenges and Opportunities. *AIDS Res. Hum. Retroviruses* **33**, 513–523 (2017).

15. Mebius, R. E. & Kraal, G. Structure and function of the spleen. *Nat. Rev. Immunol.* **5**, 606–616 (2005).

16. Cesta, M. F. Normal structure, function, and histology of the spleen. *Toxicol. Pathol.* **34**, 455–465 (2006).

17. Steiniger, B. S. Human spleen microanatomy: why mice do not suffice. *Immunology* **145**, 334–346 (2015).

18. Cataldi, M., Vigliotti, C., Mosca, T., Cammarota, M. & Capone, D. Emerging role of the spleen in the pharmacokinetics of monoclonal antibodies, nanoparticles and exosomes. *Int. J. Mol. Sci.* **18**, (2017).

19. Crean, P. A. *et al.* The fractional distribution of the cardiac output in man using microspheres labelled with technetium 99m. *Br. J. Radiol.* **59**, 209–215 (1986).

20. Davies, B. & Morris, T. Physiological parameters in laboratory animals and humans. *Pharm. Res.* **10**, 1093–1095 (1993).

21. Schmidt, E. E., MacDonald, I. C. & Groom, A. C. Comparative aspects of splenic microcirculatory pathways in mammals: the region bordering the white pulp. *Scanning Microsc* **7**, 613–628 (1993).

22. Cioc, A. M. *et al.* Rituximab-induced changes in hematolymphoid tissues found at autopsy. *Am. J. Clin. Pathol.* **130**, 604–612 (2008).

23. Bennett, M. & Schechter, G. P. Treatment of splenic marginal zone lymphoma: splenectomy versus rituximab. *Semin Hematol* **47**, 143–147 (2010).

24. Kalpadakis, C. *et al.* Rituximab monotherapy is highly effective in splenic marginal zone lymphoma. *Hematol Oncol* **25**, 127–131 (2007).

25. Kalpadakis, C. *et al.* Treatment of splenic marginal zone lymphoma with rituximab monotherapy: progress report and comparison with splenectomy. *Oncologist* **18**, 190–197 (2013).

26. Svicher, V., Ceccherini-Silberstein, F., Antinori, A., Aquaro, S. & Perno, C. F. Understanding HIV compartments and reservoirs. *Curr HIV/AIDS Rep* **11**, 186–194 (2014).

27. Reinhart, T. A. *et al.* Simian immunodeficiency virus burden in tissues and cellular compartments during clinical latency and AIDS. *J. Infect. Dis.* **176**, 1198–1208 (1997).

28. Deleage, C., Chan, C. N., Busman-Sahay, K. & Estes, J. D. Next-generation in situ hybridization approaches to define and quantify HIV and SIV reservoirs in tissue microenvironments. *Retrovirology* **15**, 4 (2018).

29. Deleage, C. *et al.* Defining HIV and SIV reservoirs in lymphoid tissues. *Pathog. Immun.* **1**, 68–106 (2016).

30. Nolan, D. J. *et al.* The Spleen Is an HIV-1 Sanctuary During Combined Antiretroviral Therapy. *AIDS Res. Hum. Retroviruses* **34**, 123–125 (2018).

31. Bozzi, G. *et al.* No evidence of ongoing HIV replication or compartmentalization in tissues during combination antiretroviral therapy: Implications for HIV eradication. *Sci. Adv.* **5**, eaav2045 (2019).

32. Diaz, L. K., Murphy, R. L., Phair, J. P. & Variakojis, D. The AIDS autopsy spleen: a comparison of the pre-anti-retroviral and highly active anti-retroviral therapy eras. *Mod. Pathol.* **15**, 406–412 (2002).

33. Williams, D. W. *et al.* Splenic Damage during SIV Infection: Role of T-Cell Depletion and Macrophage Polarization and Infection. *Am. J. Pathol.* **186**, 2068–2087 (2016).

34. Kohyama, M. *et al.* Role for Spi-C in the development of red pulp macrophages and splenic iron homeostasis. *Nature* **457**, 318–321 (2009).

35. Kurotaki, D., Uede, T. & Tamura, T. Functions and development of red pulp macrophages. *Microbiol. Immunol.* **59**, 55–62 (2015).

36. Davies, L. C., Jenkins, S. J., Allen, J. E. & Taylor, P. R. Tissue-resident macrophages. *Nat. Immunol.* **14**, 986–995 (2013).

37. Dutta, P. *et al.* Macrophages retain hematopoietic stem cells in the spleen via VCAM-1. *J. Exp. Med.* **212**, 497–512 (2015).

38. Kristiansen, M. *et al.* Identification of the haemoglobin scavenger receptor. *Nature* **409**, 198–201 (2001).

39. Haan, J. M. M. den & Kraal, G. Innate immune functions of macrophage subpopulations in the spleen. *J Innate Immun* **4**, 437–445 (2012).

40. Yadava, A., Kumar, S., Dvorak, J. A., Milon, G. & Miller, L. H. Trafficking of Plasmodium chabaudi adami-infected erythrocytes within the mouse spleen. *Proc. Natl. Acad. Sci. USA* **93**, 4595–4599 (1996).

41. Munday, J., Floyd, H. & Crocker, P. R. Sialic acid binding receptors (siglecs) expressed by macrophages. *J. Leukoc. Biol.* **66**, 705–711 (1999).

42. Vanderheijden, N. *et al.* Involvement of sialoadhesin in entry of porcine reproductive and respiratory syndrome virus into porcine alveolar macrophages. *J. Virol.* **77**, 8207–8215 (2003).

43. Elomaa, O. *et al.* Cloning of a novel bacteria-binding receptor structurally related to scavenger receptors and expressed in a subset of macrophages. *Cell* **80**, 603–609 (1995).

44. A-Gonzalez, N. *et al.* The nuclear receptor LXRα controls the functional specialization of splenic macrophages. *Nat. Immunol.* **14**, 831–839 (2013).

45. Moukambi, F. *et al.* Early Loss of Splenic Tfh Cells in SIV-Infected Rhesus Macaques. *PLoS Pathog.* **11**, e1005287 (2015).

46. Boswell, K. L. *et al.* Loss of circulating CD4 T cells with B cell helper function during chronic HIV infection. *PLoS Pathog.* **10**, e1003853 (2014).

47. Cubas, R. A. *et al.* Inadequate T follicular cell help impairs B cell immunity during HIV infection. *Nat. Med.* **19**, 494–499 (2013).

48. Rodrigues, V. *et al.* Abortive T follicular helper development is associated with a defective humoral response in Leishmania infantum-infected macaques. *PLoS Pathog.* **10**, e1004096 (2014).

49. Estes, J. D. *et al.* Simian immunodeficiency virus-induced lymphatic tissue fibrosis is mediated by transforming growth factor beta 1-positive regulatory T cells and begins in early infection. *J. Infect. Dis.* **195**, 551–561 (2007).

50. Estes, J. D. Role of collagen deposition in lymphatic tissues and immune reconstruction during HIV-1 and SIV infections. *Curr HIV/AIDS Rep* **6**, 29–35 (2009).

51. Estes, J. D. *et al.* Premature induction of an immunosuppressive regulatory T cell response during acute simian immunodeficiency virus infection. *J. Infect. Dis.* **193**, 703–712 (2006).

52. Freitas, C. R., Barbosa, A. A., Fernandes, A. L. & Andrade, Z. A. Pathology of the spleen in hepatosplenic schistosomiasis. Morphometric evaluation and extracellular matrix changes. *Mem. Inst. Oswaldo Cruz* **94**, 815–822 (1999).

53. Zhang, Z. Q. *et al.* Kinetics of CD4+ T cell repopulation of lymphoid tissues after treatment of HIV-1 infection. *Proc. Natl. Acad. Sci. USA* **95**, 1154–1159 (1998).

54. Schacker, T. W. *et al.* Collagen deposition in HIV-1 infected lymphatic tissues and T cell homeostasis. *J. Clin. Invest.* **110**, 1133–1139 (2002).

55. Schacker, T. W. *et al.* Lymphatic tissue fibrosis is associated with reduced numbers of naive CD4+ T cells in human immunodeficiency virus type 1 infection. *Clin. Vaccine Immunol.* **13**, 556–560 (2006).

56. Estes, J. *et al.* Collagen deposition limits immune reconstitution in the gut. *J. Infect. Dis.* **198**, 456–464 (2008).

57. Zeng, M. *et al.* Lymphoid tissue damage in HIV-1 infection depletes naïve T cells and limits T cell reconstitution after antiretroviral therapy. *PLoS Pathog.* **8**, e1002437 (2012).

58. Tien, P. C. *et al.* Inflammation and mortality in HIV-infected adults: analysis of the FRAM study cohort. *J. Acquir. Immune Defic. Syndr.* **55**, 316–322 (2010).

59. Toribio, M. *et al.* Effects of pitavastatin and pravastatin on markers of immune activation and arterial inflammation in HIV. *AIDS* **31**, 797–806 (2017).

60. Utay, N. S. *et al.* Telmisartan therapy does not improve lymph node or adipose tissue fibrosis more than continued antiretroviral therapy alone. *J. Infect. Dis.* **217**, 1770–1781 (2018).

61. Freiberg, M. S. *et al.* HIV infection and the risk of acute myocardial infarction. *JAMA Intern. Med.* **173**, 614–622 (2013).

62. Hunt, P. W. *et al.* T cell activation is associated with lower CD4+ T cell gains in human immunodeficiency virus-infected patients with sustained viral suppression during antiretroviral therapy. *J. Infect. Dis.* **187**, 1534–1543 (2003).

63. French, M. A., King, M. S., Tschampa, J. M., da Silva, B. A. & Landay, A. L. Serum immune activation markers are persistently increased in patients with HIV infection after 6 years of antiretroviral therapy despite suppression of viral replication and reconstitution of CD4+ T cells. *J. Infect. Dis.* **200**, 1212–1215 (2009).

64. Neuhaus, J. *et al.* Markers of inflammation, coagulation, and renal function are elevated in adults with HIV infection. *J. Infect. Dis.* **201**, 1788–1795 (2010).

65. Deeks, S. G., Tracy, R. & Douek, D. C. Systemic effects of inflammation on health during chronic HIV infection. *Immunity* **39**, 633–645 (2013).

66. Burdo, T. H. *et al.* Increased monocyte turnover from bone marrow correlates with severity of SIV encephalitis and CD163 levels in plasma. *PLoS Pathog.* **6**, e1000842 (2010).

67. Burdo, T. H. *et al.* Soluble CD163 made by monocyte/macrophages is a novel marker of HIV activity in early and chronic infection prior to and after anti-retroviral therapy. *J. Infect. Dis.* **204**, 154–163 (2011).

68. Bronte, V. & Pittet, M. J. The spleen in local and systemic regulation of immunity. *Immunity* **39**, 806–818 (2013).

69. Swirski, F. K. *et al.* Identification of splenic reservoir monocytes and their deployment to inflammatory sites. *Science* **325**, 612–616 (2009).

70. Falk, S., Müller, H. & Stutte, H. J. The spleen in acquired immunodeficiency syndrome (AIDS). *Pathol Res Pract* **183**, 425–433 (1988).

71. Falk, S. & Stutte, H. J. The spleen in HIV infection — morphological evidence of HIV-associated macrophage dysfunction. *Res Virol* **141**, 161–169 (1990).

72. Wagner, T. A. *et al.* HIV latency. Proliferation of cells with HIV integrated into cancer genes contributes to persistent infection. *Science* **345**, 570–573 (2014).

73. Kulpa, D. A. & Chomont, N. HIV persistence in the setting of antiretroviral therapy: when, where and how does HIV hide? *J. Virus Erad.* **1**, 59–66 (2015).

74. Simonetti, F. R. *et al.* Clonally expanded CD4+ T cells can produce infectious HIV-1 in vivo. *Proc. Natl. Acad. Sci. USA* **113**, 1883–1888 (2016).

75. Kearney, M. F. *et al.* Origin of Rebound Plasma HIV Includes Cells with Identical Proviruses That Are Transcriptionally Active before Stopping of Antiretroviral Therapy. *J. Virol.* **90**, 1369–1376 (2016).

76. Lee, E. *et al.* Impact of Antiretroviral Therapy Duration on HIV-1 Infection of T Cells within Anatomic Sites. *J. Virol.* **94**, (2020).

77. von Stockenstrom, S. *et al.* Longitudinal genetic characterization reveals that cell proliferation maintains a persistent HIV type 1 DNA pool during effective HIV therapy. *J. Infect. Dis.* **212**, 596–607 (2015).

78. Mascio, M. Di *et al.* Antiretroviral tissue kinetics: in vivo imaging using positron emission tomography. *Antimicrob. Agents Chemother.* **53**, 4086–4095 (2009).

79. Lee, W. A. *et al.* Selective intracellular activation of a novel prodrug of the human immunodeficiency virus reverse transcriptase inhibitor tenofovir leads to preferential distribution and accumulation in lymphatic tissue. *Antimicrob. Agents Chemother.* **49**, 1898–1906 (2005).

80. Devanathan, A. S. *et al.* Antiretroviral penetration and drug transporter concentrations in the spleens of three preclinical animal models and humans. *Antimicrob. Agents Chemother.* **64**, e01384–20 (2020).

81. Devanathan, A. S. *et al.* Antiretroviral Penetration across Three Preclinical Animal Models and Humans in Eight Putative HIV Viral Reservoirs. *Antimicrob. Agents Chemother.* **64**, (2019).

82. Shen, L. & Siliciano, R. F. Viral reservoirs, residual viremia, and the potential of highly active antiretroviral therapy to eradicate HIV infection. *J. Allergy Clin. Immunol.* **122**, 22–28 (2008).

83. Lorenzo-Redondo, R. *et al.* Persistent HIV-1 replication maintains the tissue reservoir during therapy. *Nature* **530**, 51–56 (2016).

84. Kis, O., Robillard, K., Chan, G. N. Y. & Bendayan, R. The complexities of antiretroviral drug-drug interactions: role of ABC and SLC transporters. *Trends Pharmacol. Sci.* **31**, 22–35 (2010).

85. Hodges, V. M., Molloy, G. Y. & Wickramasinghe, S. N. Demonstration of mRNA for five species of cytochrome P450 in human bone marrow, bone marrow-derived macrophages and human haemopoietic cell lines. *Br. J. Haematol.* **108**, 151–156 (2000).

86. Wickramasinghe, S. N. Evidence of drug metabolism by macrophages: possible role of macrophages in the pathogenesis of drug-induced tissue damage and in the activation of environmental procarcinogens. *Clin Lab Haematol* **9**, 271–280 (1987).

87. Wickramasinghe, S. N., Barden, G. & Gardner, B. Ability of unstimulated and phorbol-ester-stimulated human blood-monocyte-derived macrophages to metabolize drugs and its implications. *Clin Lab Haematol* **13**, 41–50 (1991).

88. Elliott, J. I., Raguz, S. & Higgins, C. F. Multidrug transporter activity in lymphocytes. *Br. J. Pharmacol.* **143**, 899–907 (2004).

89. Joukhadar, C. *et al.* Impaired target site penetration of beta-lactams may account for therapeutic failure in patients with septic shock. *Crit. Care Med.* **29**, 385–391 (2001).

90. Thompson, C. G., Cohen, M. S. & Kashuba, A. D. M. Antiretroviral pharmacology in mucosal tissues. *J. Acquir. Immune Defic. Syndr.* **63 Suppl 2**, S240–7 (2013).

91. Mouton, J. W. *et al.* Tissue concentrations: do we ever learn? *J. Antimicrob. Chemother.* **61**, 235–237 (2008).

92. Thompson, C. G. *et al.* Mass spectrometry imaging reveals heterogeneous efavirenz distribution within putative HIV reservoirs. *Antimicrob. Agents Chemother.* **59**, 2944–2948 (2015).

93. Thompson, C. G. *et al.* Heterogeneous antiretroviral drug distribution and HIV/SHIV detection in the gut of three species. *Sci. Transl. Med.* **11**, (2019).

94. Bokhart, M. T. *et al.* Quantitative mass spectrometry imaging of emtricitabine in cervical tissue model using infrared matrix-assisted laser desorption electrospray ionization. *Anal. Bioanal. Chem.* **407**, 2073–2084 (2015).

95. Bokhart, M. T. & Muddiman, D. C. Infrared matrix-assisted laser desorption electrospray ionization mass spectrometry imaging analysis of biospecimens. *Analyst* **141**, 5236–5245 (2016).

96. Robichaud, G., Barry, J. A., Garrard, K. P. & Muddiman, D. C. Infrared matrix-assisted laser desorption electrospray ionization (IR-MALDESI) imaging source coupled to a FT-ICR mass spectrometer. *J Am Soc Mass Spectrom* **24**, 92–100 (2013).

97. Deeks, S. G. HIV: Shock and kill. *Nature* **487**, 439–440 (2012).

98. Bose, P., Dai, Y. & Grant, S. Histone deacetylase inhibitor (HDACI) mechanisms of action: emerging insights. *Pharmacol. Ther.* **143**, 323–336 (2014).

99. Perrin, J. *et al.* Identifying drug targets in tissues and whole blood with thermal-shift profiling. *Nat. Biotechnol.* **38**, 303–308 (2020).

100. Norton, N. J., Mok, H. P., Sharif, F., Hirst, J. C. & Lever, A. M. L. HIV silencing and inducibility are heterogeneous and are affected by factors intrinsic to the virus. *MBio* **10**, (2019).

101. Guo, Y. *et al.* Therapeutic potential of Pak1 inhibition for pain associated with cutaneous burn injury. *Mol. Pain* **14**, 1744806918788648 (2018).

102. Jacobson, J. M. *et al.* Safety, pharmacokinetics, and antiretroviral activity of multiple doses of ibalizumab (formerly TNX-355), an anti-CD4 monoclonal antibody, in human immunodeficiency virus type 1-infected adults. *Antimicrob. Agents Chemother.* **53**, 450–457 (2009).

103. Emu, B. *et al.* Phase 3 Study of Ibalizumab for Multidrug-Resistant HIV-1. *N. Engl. J. Med.* **379**, 645–654 (2018).

104. Bettiker, R. L., Koren, D. E. & Jacobson, J. M. Ibalizumab. *Curr Opin HIV AIDS* (2018).doi:10.1097/COH.0000000000000473

105. Iacob, S. A. & Iacob, D. G. Ibalizumab targeting CD4 receptors, an emerging molecule in HIV therapy. *Front. Microbiol.* **8**, 2323 (2017).

106. Sheikh, V., Murray, J. S. & Sherwat, A. Ibalizumab in Multidrug-Resistant HIV - Accepting Uncertainty. *N. Engl. J. Med.* **379**, 605–607 (2018).

107. Buss, N. A. P. S., Henderson, S. J., McFarlane, M., Shenton, J. M. & de Haan, L. Monoclonal antibody therapeutics: history and future. *Curr. Opin. Pharmacol.* **12**, 615–622 (2012).

108. Wang, W., Wang, E. Q. & Balthasar, J. P. Monoclonal antibody pharmacokinetics and pharmacodynamics. *Clin. Pharmacol. Ther.* **84**, 548–558 (2008).

109. Shah, D. K. & Betts, A. M. Towards a platform PBPK model to characterize the plasma and tissue disposition of monoclonal antibodies in preclinical species and human. *J Pharmacokinet Pharmacodyn* **39**, 67–86 (2012).

110. Cao, Y. & Jusko, W. J. Survey of monoclonal antibody disposition in man utilizing a minimal physiologically-based pharmacokinetic model. *J Pharmacokinet Pharmacodyn* **41**, 571–580 (2014).

111. Kaufman, S. & Deng, Y. Splenic control of intravascular volume in the rat. *J. Physiol. (Lond.)* **468**, 557–565 (1993).

112. Tabrizi, M., Bornstein, G. G. & Suria, H. Biodistribution mechanisms of therapeutic monoclonal antibodies in health and disease. *AAPS J.* **12**, 33–43 (2010).

113. Akilesh, S., Christianson, G. J., Roopenian, D. C. & Shaw, A. S. Neonatal FcR expression in bone marrow-derived cells functions to protect serum IgG from catabolism. *J. Immunol.* **179**, 4580–4588 (2007).

114. Yip, V. *et al.* Quantitative cumulative biodistribution of antibodies in mice: effect of modulating binding affinity to the neonatal Fc receptor. *MAbs* **6**, 689–696 (2014).

115. Gruell, H. & Klein, F. Antibody-mediated prevention and treatment of HIV-1 infection. *Retrovirology* **15**, 73 (2018).

116. Kuhlmann, A.-S., Peterson, C. W. & Kiem, H.-P. Chimeric antigen receptor T-cell approaches to HIV cure. *Curr Opin HIV AIDS* **13**, 446–453 (2018).

117. Moore, J. P., McKeating, J. A., Huang, Y. X., Ashkenazi, A. & Ho, D. D. Virions of primary human immunodeficiency virus type 1 isolates resistant to soluble CD4 (sCD4) neutralization differ in sCD4 binding and glycoprotein gp120 retention from sCD4-sensitive isolates. *J. Virol.* **66**, 235–243 (1992).

118. Zhen, A., Carrillo, M. A. & Kitchen, S. G. Chimeric antigen receptor engineered stem cells: a novel HIV therapy. *Immunotherapy* **9**, 401–410 (2017).

119. Yang, G. *et al.* Identification of autoantigens recognized by the 2F5 and 4E10 broadly neutralizing HIV-1 antibodies. *J. Exp. Med.* **210**, 241–256 (2013).

120. McCoy, L. E. & Burton, D. R. Identification and specificity of broadly neutralizing antibodies against HIV. *Immunol. Rev.* **275**, 11–20 (2017).

121. Wallace, P. K. *et al.* Mechanisms of adoptive immunotherapy: improved methods for in vivo tracking of tumor-infiltrating lymphocytes and lymphokine-activated killer cells. *Cancer Res.* **53**, 2358–2367 (1993).

122. Melder, R. J. *et al.* Systemic distribution and tumor localization of adoptively transferred lymphocytes in mice: comparison with physiologically based pharmacokinetic model. *Neoplasia* **4**, 3–8 (2002).

123. Stekel, D. J., Parker, C. E. & Nowak, M. A. A model of lymphocyte recirculation. *Immunol. Today* **18**, 216–221 (1997).

124. Khot, A., Matsueda, S., Thomas, V. A., Koya, R. C. & Shah, D. K. Measurement and Quantitative Characterization of Whole-Body Pharmacokinetics of Exogenously Administered T Cells in Mice. *J. Pharmacol. Exp. Ther.* **368**, 503–513 (2019).

125. Hersey, P. The separation and' ' 51 chromium labeling of human lymphocytes with in vivo studies of survival and migration. *Blood* **38**, 360–371 (1971).

126. Chun, T. W. *et al.* Early establishment of a pool of latently infected, resting CD4(+) T cells during primary HIV-1 infection. *Proc. Natl. Acad. Sci. USA* **95**, 8869–8873 (1998).

127. Chun, T. W., Davey, R. T., Engel, D., Lane, H. C. & Fauci, A. S. Re-emergence of HIV after stopping therapy. *Nature* **401**, 874–875 (1999).

128. Palmer, S., Josefsson, L. & Coffin, J. M. HIV reservoirs and the possibility of a cure for HIV infection. *J. Intern. Med.* **270**, 550–560 (2011).

129. Smith, M. Z., Wightman, F. & Lewin, S. R. HIV reservoirs and strategies for eradication. *Curr HIV/AIDS Rep* **9**, 5–15 (2012).

130. Kuo, H.-H. & Lichterfeld, M. Recent progress in understanding HIV reservoirs. *Curr Opin HIV AIDS* (2017).doi:10.1097/COH.0000000000000441

131. Batista, F. D. & Harwood, N. E. The who, how and where of antigen presentation to B cells. *Nat. Rev. Immunol.* **9**, 15–27 (2009).

132. Lamers, S. L. *et al.* HIV DNA Is Frequently Present within Pathologic Tissues Evaluated at Autopsy from Combined Antiretroviral Therapy-Treated Patients with Undetectable Viral Loads. *J. Virol.* **90**, 8968–8983 (2016).

133. Fletcher, C. V. *et al.* Sex-based differences in saquinavir pharmacology and virologic response in AIDS Clinical Trials Group Study 359. *J. Infect. Dis.* **189**, 1176–1184 (2004).

134. Antonelli, G. *et al.* Resistance of HIV-1 to AZT might also involve the cellular expression of multidrug resistance P-glycoprotein. *AIDS Res. Hum. Retroviruses* **8**, 1839–1844 (1992).

135. Evans, D. T. & Silvestri, G. Nonhuman primate models in AIDS research. *Curr Opin HIV AIDS* **8**, 255–261 (2013).

136. Thompson, C. G. *et al.* Multimodal analysis of drug transporter expression in gastrointestinal tissue. *AIDS* **31**, 1669–1678 (2017).

137. Burgunder, E. *et al.* Antiretroviral Drug Concentrations in Lymph Nodes: A Cross-Species Comparison of the Effect of Drug Transporter Expression, Viral Infection, and Sex in Humanized Mice, Nonhuman Primates, and Humans. *J. Pharmacol. Exp. Ther.* **370**, 360–368 (2019).

138. Denton, P. W. & Garcia, J. V. Novel humanized murine models for HIV research. *Curr HIV/AIDS Rep* **6**, 13–19 (2009).

139. Hatziioannou, T. & Evans, D. T. Animal models for HIV/AIDS research. *Nat. Rev. Microbiol.* **10**, 852–867 (2012).

140. Loo, P. L. P. Van, Zutphen, L. F. M. Van & Baumans, V. Male management: Coping with aggression problems in male laboratory mice. *Lab Anim* **37**, 300–313 (2003).

141. North, T. W. *et al.* Viral sanctuaries during highly active antiretroviral therapy in a nonhuman primate model for AIDS. *J. Virol.* **84**, 2913–2922 (2010).

142. Denton, P. W. *et al.* Systemic administration of antiretrovirals prior to exposure prevents rectal and intravenous HIV-1 transmission in humanized BLT mice. *PLoS One* **5**, e8829 (2010).

143. Neff, C. P., Ndolo, T., Tandon, A., Habu, Y. & Akkina, R. Oral pre-exposure prophylaxis by anti-retrovirals raltegravir and maraviroc protects against HIV-1 vaginal transmission in a humanized mouse model. *PLoS One* **5**, e15257 (2010).

144. Shytaj, I. L. *et al.* A highly intensified ART regimen induces long-term viral suppression and restriction of the viral reservoir in a simian AIDS model. *PLoS Pathog.* **8**, e1002774 (2012).

145. Veselinovic, M. *et al.* HIV pre-exposure prophylaxis: mucosal tissue drug distribution of RT inhibitor Tenofovir and entry inhibitor Maraviroc in a humanized mouse model. *Virology* **464-465**, 253–263 (2014).

146. Massud, I. *et al.* Lack of prophylactic efficacy of oral maraviroc in macaques despite high drug concentrations in rectal tissues. *J. Virol.* **87**, 8952–8961 (2013).

147. Anderson, P. L. *et al.* Pharmacological considerations for tenofovir and emtricitabine to prevent HIV infection. *J. Antimicrob. Chemother.* **66**, 240–250 (2011).

148. Srinivas, N. *et al.* Antiretroviral concentrations and surrogate measures of efficacy in the brain tissue and CSF of preclinical species. *Xenobiotica* **49**, 1192–1201 (2019).

149. Truvada [package insert]. Gilead Sciences, Inc. Foster City, CA. at <https://www.gilead.com/~/media/Files/pdfs/medicines/hiv/truvada/truvada_pi.pdf>

150. Fallon, J. K., Neubert, H., Hyland, R., Goosen, T. C. & Smith, P. C. Targeted quantitative proteomics for the analysis of 14 UGT1As and -2Bs in human liver using NanoUPLC-MS/MS with selected reaction monitoring. *J. Proteome Res.* **12**, 4402–4413 (2013).

151. Zhou, T., Hu, M., Cost, M., Poloyac, S. & Rohan, L. Short communication: expression of transporters and metabolizing enzymes in the female lower genital tract: implications for microbicide research. *AIDS Res. Hum. Retroviruses* **29**, 1496–1503 (2013).

152. Nicol, M. R. *et al.* Expression of six drug transporters in vaginal, cervical, and colorectal tissues: Implications for drug disposition in HIV prevention. *J. Clin. Pharmacol.* **54**, 574–583 (2014).

153. Huang, Y. *et al.* Antiretroviral drug transporters and metabolic enzymes in human testicular tissue: potential contribution to HIV-1 sanctuary site. *J. Antimicrob. Chemother.* **71**, 1954–1965 (2016).

154. Minuesa, G. *et al.* Drug uptake transporters in antiretroviral therapy. *Pharmacol. Ther.* **132**, 268–279 (2011).

155. Fallon, J. K., Smith, P. C., Xia, C. Q. & Kim, M.-S. Quantification of Four Efflux Drug Transporters in Liver and Kidney Across Species Using Targeted Quantitative Proteomics by Isotope Dilution NanoLC-MS/MS. *Pharm. Res.* **33**, 2280–2288 (2016).

156. Khatri, R. *et al.* Targeted quantitative proteomic analysis of drug metabolizing enzymes and transporters by nano LC-MS/MS in the sandwich cultured human hepatocyte model. *J. Pharmacol. Toxicol. Methods* **98**, 106590 (2019).

157. Cottrell, M. L. *et al.* A translational pharmacology approach to predicting outcomes of preexposure prophylaxis against HIV in men and women using tenofovir disoproxil fumarate with or without emtricitabine. *J. Infect. Dis.* **214**, 55–64 (2016).

158. Reyataz [package insert] Princeton (NJ); Bristol-Myers Squibb Company. (2003).at <https://packageinserts.bms.com/pi/pi_reyataz.pdf>

159. Sustiva [package insert] Princeton (NJ); Bristol-Myers Squibb Company. (1998).at <https://packageinserts.bms.com/pi/pi_sustiva.pdf>

160. Isentress [package insert[Whitehouse Station (NJ); Merck & Co., Inc. (2007).at <https://www.merck.com/product/usa/pi_circulars/i/isentress/isentress_pi.pdf>

161. Selzentry [package insert] New York (NY); Pfizer, Inc. (2007).at <https://www.accessdata.fda.gov/drugsatfda_docs/label/2007/022128lbl.pdf>

162. Durand-Gasselin, L., Silva, D. Da, Benech, H., Pruvost, A. & Grassi, J. Evidence and possible consequences of the phosphorylation of nucleoside reverse transcriptase inhibitors in human red blood cells. *Antimicrob. Agents Chemother.* **51**, 2105–2111 (2007).

163. Adams, J. L. *et al.* Tenofovir diphosphate and emtricitabine triphosphate concentrations in blood cells compared with isolated peripheral blood mononuclear cells: a new measure of antiretroviral adherence? *J. Acquir. Immune Defic. Syndr.* **62**, 260–266 (2013).

164. Hu, M., Valicherla, G. R., Zhou, T., Hillier, S. L. & Rohan, L. C. Expression, Activity, and Regulation of Phosphorylating Enzymes in Tissues and Cells Relevant to HIV-1 Sexual Transmission. *AIDS Res. Hum. Retroviruses* **38**, 22–32 (2022).

165. Robbins, B. L., Srinivas, R. V., Kim, C., Bischofberger, N. & Fridland, A. Anti-human immunodeficiency virus activity and cellular metabolism of a potential prodrug of the acyclic nucleoside phosphonate 9-R-(2-phosphonomethoxypropyl)adenine (PMPA), Bis(isopropyloxymethylcarbonyl)PMPA. *Antimicrob. Agents Chemother.* **42**, 612–617 (1998).

166. Boffito, M. *et al.* Protein binding in antiretroviral therapies. *AIDS Res. Hum. Retroviruses* **19**, 825–835 (2003).

167. Gaur, P. K., Mishra, S., Bajpai, M. & Mishra, A. Enhanced oral bioavailability of efavirenz by solid lipid nanoparticles: in vitro drug release and pharmacokinetics studies. *Biomed Res. Int.* **2014**, 363404 (2014).

168. Janneh, O. *et al.* Intracellular accumulation of efavirenz and nevirapine is independent of P-glycoprotein activity in cultured CD4 T cells and primary human lymphocytes. *J. Antimicrob. Chemother.* **64**, 1002–1007 (2009).

169. Srinivas, N., Maffuid, K. & Kashuba, A. D. M. Clinical pharmacokinetics and pharmacodynamics of drugs in the central nervous system. *Clin Pharmacokinet* **57**, 1059–1074 (2018).

170. Dumond, J. B. *et al.* Maraviroc concentrates in the cervicovaginal fluid and vaginal tissue of HIV-negative women. *J. Acquir. Immune Defic. Syndr.* **51**, 546–553 (2009).

171. Hoefnagel, J. G. M., Koopmans, P. P., Burger, D. M., Schuurman, R. & Galama, J. M. D. Role of the inhibitory quotient in HIV therapy. *Antivir Ther (Lond)* **10**, 879–892 (2005).

172. Winston, A. & Khoo, S. Clinical application of the inhibitory quotient: is there a role in HIV protease inhibitor therapy? *Curr Opin HIV AIDS* **3**, 608–611 (2008).

173. Boffito, M. Pharmacokinetic implications of resistance. In *Antiretroviral resistance in clinical practice* (Geretti, A. M.) (Mediscript, London, 2006).

174. Cottrell, M. L., Srinivas, N. & Kashuba, A. D. M. Pharmacokinetics of antiretrovirals in mucosal tissue. *Expert Opin Drug Metab Toxicol* **11**, 893–905 (2015).

175. Feng, J. Y. *et al.* The triple combination of tenofovir, emtricitabine and efavirenz shows synergistic anti-HIV-1 activity in vitro: a mechanism of action study. *Retrovirology* **6**, 44 (2009).

176. Desuzinges-Mandon, E. *et al.* ABCG2 transports and transfers heme to albumin through its large extracellular loop. *J. Biol. Chem.* **285**, 33123–33133 (2010).

177. Pal, D. *et al.* Efflux transporters- and cytochrome P-450-mediated interactions between drugs of abuse and antiretrovirals. *Life Sci.* **88**, 959–971 (2011).

178. Wang, X. *et al.* Breast cancer resistance protein (BCRP/ABCG2) induces cellular resistance to HIV-1 nucleoside reverse transcriptase inhibitors. *Mol. Pharmacol.* **63**, 65–72 (2003).

179. Jedlitschky, G. *et al.* The nucleotide transporter MRP4 (ABCC4) is highly expressed in human platelets and present in dense granules, indicating a role in mediator storage. *Blood* **104**, 3603–3610 (2004).

180. Lu, H., Chen, C. & Klaassen, C. Tissue distribution of concentrative and equilibrative nucleoside transporters in male and female rats and mice. *Drug Metab. Dispos.* **32**, 1455–1461 (2004).

181. Iikura, M. *et al.* ENT1, a ribavirin transporter, plays a pivotal role in antiviral efficacy of ribavirin in a hepatitis C virus replication cell system. *Antimicrob. Agents Chemother.* **56**, 1407–1413 (2012).

182. Zhang, J. *et al.* The role of nucleoside transporters in cancer chemotherapy with nucleoside drugs. *Cancer Metastasis Rev.* **26**, 85–110 (2007).

183. Cerveny, L. *et al.* Equilibrative Nucleoside Transporter 1 (ENT1, SLC29A1) Facilitates Transfer of the Antiretroviral Drug Abacavir across the Placenta. *Drug Metab. Dispos.* **46**, 1817–1826 (2018).

184. Latunde-Dada, G. O., Laftah, A. H., Masaratana, P., McKie, A. T. & Simpson, R. J. Expression of ABCG2 (BCRP) in mouse models with enhanced erythropoiesis. *Front. Pharmacol.* **5**, 135 (2014).

185. Takenaka, K. *et al.* Substrate overlap between Mrp4 and Abcg2/Bcrp affects purine analogue drug cytotoxicity and tissue distribution. *Cancer Res.* **67**, 6965–6972 (2007).

186. Paproski, R. J. *et al.* Biodistribution and uptake of 3'-deoxy-3'-fluorothymidine in ENT1-knockout mice and in an ENT1-knockdown tumor model. *J. Nucl. Med.* **51**, 1447–1455 (2010).

187. Vildhede, A., Wiśniewski, J. R., Norén, A., Karlgren, M. & Artursson, P. Comparative Proteomic Analysis of Human Liver Tissue and Isolated Hepatocytes with a Focus on Proteins Determining Drug Exposure. *J. Proteome Res.* **14**, 3305–3314 (2015).

188. Kumar, V. *et al.* A Comparison of Total and Plasma Membrane Abundance of Transporters in Suspended, Plated, Sandwich-Cultured Human Hepatocytes Versus Human Liver Tissue Using Quantitative Targeted Proteomics and Cell Surface Biotinylation. *Drug Metab. Dispos.* **47**, 350–357 (2019).

189. Siest, G. *et al.* Transcription factor and drug-metabolizing enzyme gene expression in lymphocytes from healthy human subjects. *Drug Metab. Dispos.* **36**, 182–189 (2008).

190. Palmisano, L. & Vella, S. A brief history of antiretroviral therapy of HIV infection: success and challenges. *Ann. Ist. Super. Sanita* **47**, 44–48 (2011).

191. Samji, H. *et al.* Closing the gap: increases in life expectancy among treated HIV-positive individuals in the United States and Canada. *PLoS One* **8**, e81355 (2013).

192. Chun, T. W. *et al.* Quantification of latent tissue reservoirs and total body viral load in HIV-1 infection. *Nature* **387**, 183–188 (1997).

193. Chun, T.-W. *et al.* Persistence of HIV in gut-associated lymphoid tissue despite long-term antiretroviral therapy. *J. Infect. Dis.* **197**, 714–720 (2008).

194. Chun, T.-W. & Fauci, A. S. HIV reservoirs:' ' pathogenesis and obstacles to viral eradication and cure. *AIDS* **26**, 1261–1268 (2012).

195. Busman-Sahay, K., Starke, C. E., Nekorchuk, M. D. & Estes, J. D. Eliminating HIV reservoirs for a cure: the issue is in the tissue. *Curr Opin HIV AIDS* **16**, 200–208 (2021).

196. Chaillon, A. *et al.* HIV persists throughout deep tissues with repopulation from multiple anatomical sources. *J. Clin. Invest.* **130**, 1699–1712 (2020).

197. Scholz, E. M. B. *et al.* Quantitative Imaging Analysis of the Spatial Relationship between Antiretrovirals, Reverse Transcriptase Simian-Human Immunodeficiency Virus RNA, and Collagen in the Mesenteric Lymph Nodes of Nonhuman Primates. *Antimicrob. Agents Chemother.* **65**, (2021).

198. Barry, J. A., Groseclose, M. R. & Castellino, S. Quantification and assessment of detection capability in imaging mass spectrometry using a revised mimetic tissue model. *Bioanalysis* **11**, 1099–1116 (2019).

199. Dorr, P. *et al.* Maraviroc (UK-427,857), a potent, orally bioavailable, and selective small-molecule inhibitor of chemokine receptor CCR5 with broad-spectrum anti-human immunodeficiency virus type 1 activity. *Antimicrob. Agents Chemother.* **49**, 4721–4732 (2005).

200. Temesgen, Z. & Siraj, D. S. Raltegravir: first in class HIV integrase inhibitor. *Ther Clin Risk Manag* **4**, 493–500 (2008).

201. Emtriva [package insert]. Gilead Sciences, Inc. Foster City, CA. at <https://www.gilead.com/~/media/Files/pdfs/medicines/hiv/emtriva/emtriva_pi.pdf>

202. European Medicines Agency *REYATAZ (atazanavir) new drug application, scientific discussion*. (2004).

203. Viread [package insert]. Gilead Sciences, Inc. Foster City, CA. at <https://www.gilead.com/~/media/Files/pdfs/medicines/liver-disease/viread/viread_pi.pdf>

204. Bokhart, M. T., Nazari, M., Garrard, K. P. & Muddiman, D. C. MSiReader v1.0: Evolving Open-Source Mass Spectrometry Imaging Software for Targeted and Untargeted Analyses. *J Am Soc Mass Spectrom* **29**, 8–16 (2018).

205. Vibholm, L. K. *et al.* Characterization of Intact Proviruses in Blood and Lymph Node from HIV-Infected Individuals Undergoing Analytical Treatment Interruption. *J. Virol.* **93**, (2019).

206. Rothenberger, M. K. *et al.* Large number of rebounding/founder HIV variants emerge from multifocal infection in lymphatic tissues after treatment interruption. *Proc. Natl. Acad. Sci. USA* **112**, E1126–34 (2015).

207. Haase, A. T. *et al.* Quantitative image analysis of HIV-1 infection in lymphoid tissue. *Science* **274**, 985–989 (1996).

208. Haase, A. T. Population biology of HIV-1 infection: viral and CD4+ T cell demographics and dynamics in lymphatic tissues. *Annu. Rev. Immunol.* **17**, 625–656 (1999).

209. Langeveld, M., Gamadia, L. E. & Berge, I. J. M. ten T-lymphocyte subset distribution in human spleen. *Eur. J. Clin. Invest.* **36**, 250–256 (2006).

210. Jochmans, D. *et al.* Selective killing of human immunodeficiency virus infected cells by non-nucleoside reverse transcriptase inhibitor-induced activation of HIV protease. *Retrovirology* **7**, 89 (2010).

211. Trinité, B., Zhang, H. & Levy, D. N. NNRTI-induced HIV-1 protease-mediated cytotoxicity induces rapid death of CD4 T cells during productive infection and latency reversal. *Retrovirology* **16**, 17 (2019).

212. Chaurand, P., Schriver, K. E. & Caprioli, R. M. Instrument design and characterization for high resolution MALDI-MS imaging of tissue sections. *J Mass Spectrom* **42**, 476–489 (2007).

213. Cadena, A. M. *et al.* Persistence of viral RNA in lymph nodes in ART-suppressed SIV/SHIV-infected Rhesus Macaques. *Nat. Commun.* **12**, 1474 (2021).

214. Jones, H. & Rowland-Yeo, K. Basic concepts in physiologically based pharmacokinetic modeling in drug discovery and development. *CPT Pharmacometrics Syst. Pharmacol.* **2**, e63 (2013).

215. Scholz, E. M. B., Cao, Y. & Kashuba, A. D. M. A cross-species comparison of antiretroviral penetration into lymph nodes using novel physiologically based pharmacokinetic models. *J. Antimicrob. Chemother.* (2021).doi:10.1093/jac/dkab298

216. Garrett, K. L. *et al.* A pharmacokinetic/pharmacodynamic model to predict effective HIV prophylaxis dosing strategies for people who inject drugs. *J. Pharmacol. Exp. Ther.* **367**, 245–251 (2018).

217. Calcagno, A., Perri, G. Di & Bonora, S. Pharmacokinetics and pharmacodynamics of antiretrovirals in the central nervous system. *Clin Pharmacokinet* **53**, 891–906 (2014).

218. Trezza, C. R. & Kashuba, A. D. M. Pharmacokinetics of antiretrovirals in genital secretions and anatomic sites of HIV transmission: implications for HIV prevention. *Clin Pharmacokinet* **53**, 611–624 (2014).

219. Patterson, K. B. *et al.* Penetration of tenofovir and emtricitabine in mucosal tissues: implications for prevention of HIV-1 transmission. *Sci. Transl. Med.* **3**, 112re4 (2011).

220. Fletcher, C. V. *et al.* The Lymphoid Tissue Pharmacokinetics of Tenofovir Disoproxil Fumarate and Tenofovir Alafenamide in HIV-Infected Persons. *Clin. Pharmacol. Ther.* (2020).doi:10.1002/cpt.1883

221. Hawkins, T. *et al.* Intracellular pharmacokinetics of tenofovir diphosphate, carbovir triphosphate, and lamivudine triphosphate in patients receiving triple-nucleoside regimens. *J. Acquir. Immune Defic. Syndr.* **39**, 406–411 (2005).

222. Pruvost, A. *et al.* Pilot pharmacokinetic study of human immunodeficiency virus-infected patients receiving tenofovir disoproxil fumarate (TDF): investigation of systemic and intracellular interactions between TDF and abacavir, lamivudine, or lopinavir-ritonavir. *Antimicrob. Agents Chemother.* **53**, 1937–1943 (2009).

223. Wang, L. H. *et al.* Pharmacokinetic and pharmacodynamic characteristics of emtricitabine support its once daily dosing for the treatment of HIV infection. *AIDS Res. Hum. Retroviruses* **20**, 1173–1182 (2004).

224. Jindal, H. K., Ai, Z., Gascard, P., Horton, C. & Cohen, C. M. Specific loss of protein kinase activities in senescent erythrocytes. *Blood* **88**, 1479–1487 (1996).

225. Bratosin, D. *et al.* Cellular and molecular mechanisms of senescent erythrocyte phagocytosis by macrophages. A review. *Biochimie* **80**, 173–195 (1998).

226. Dyavar, S. R. *et al.* Intramuscular and subcutaneous administration of antiretroviral drugs, compared with oral, enhances delivery to lymphoid tissues in BALB/c mice. *J. Antimicrob. Chemother.* **76**, 2651–2658 (2021).

227. McLennan, D. N., Porter, C. J. H. & Charman, S. A. Subcutaneous drug delivery and the role of the lymphatics. *Drug Discov. Today. Technol.* **2**, 89–96 (2005).

228. Richter, W. F., Bhansali, S. G. & Morris, M. E. Mechanistic determinants of biotherapeutics absorption following SC administration. *AAPS J.* **14**, 559–570 (2012).

229. Richter, W. F. & Jacobsen, B. Subcutaneous absorption of biotherapeutics: knowns and unknowns. *Drug Metab. Dispos.* **42**, 1881–1889 (2014).

230. Spreen, W. *et al.* GSK1265744 pharmacokinetics in plasma and tissue after single-dose long-acting injectable administration in healthy subjects. *J. Acquir. Immune Defic. Syndr.* **67**, 481–486 (2014).

231. Cattaneo, D. & Gervasoni, C. Pharmacokinetics and Pharmacodynamics of Cabotegravir, a Long-Acting HIV Integrase Strand Transfer Inhibitor. *Eur J Drug Metab Pharmacokinet* **44**, 319–327 (2019).

232. Uhlen, M. *et al.* Towards a knowledge-based Human Protein Atlas. *Nat. Biotechnol.* **28**, 1248–1250 (2010).

233. National Center for Biotechnology Information Romidepsin CID=5352062. at <https://pubchem.ncbi.nlm.nih.gov/compound/Romidepsin>

234. National Center for Biotechnology Information Panobinostat CID=6918837. at <https://pubchem.ncbi.nlm.nih.gov/compound/Panobinostat>

235. Smit, M. M. *et al.* Spatially annotated single cell sequencing for unraveling intratumor heterogeneity. *Front. Bioeng. Biotechnol.* **10**, 829509 (2022).

236. Corley, M. J. & Farhadian, S. F. Emerging Single-cell Approaches to Understand HIV in the Central Nervous System. *Curr HIV/AIDS Rep* **19**, 113–120 (2022).